INFORMATION TO USERS

This manuscript has been reproduced from the microfilm master. UMI films the text directly from the original or copy submitted. Thus, some thesis and dissertation copies are in typewriter face, while others may be from any type of computer printer.

The quality of this reproduction is dependent upon the quality of the copy submitted. Broken or indistinct print, colored or poor quality illustrations and photographs, print bleedthrough, substandard margins, and improper alignment can adversely affect reproduction.

In the unlikely event that the author did not send UMI a complete manuscript and there are missing pages, these will be noted. Also, if unauthorized copyright material had to be removed, a note will indicate the deletion.

Oversize materials (e.g., maps, drawings, charts) are reproduced by sectioning the original, beginning at the upper left-hand corner and continuing from left to right in equal sections with small overlaps.

Photographs included in the original manuscript have been reproduced xerographically in this copy. Higher quality 6" x 9" black and white photographic prints are available for any photographs or illustrations appearing in this copy for an additional charge. Contact UMI directly to order.

Bell & Howell Information and Learning
300 North Zeeb Road, Ann Arbor, MI 48106-1346 USA

UMI®
800-521-0600

Experimental Investigations of Corona-Discharge Oxidation of Silicon

Sayed-Masoud Sayedi

A Thesis

in

The Department

of

Electrical and Computer Engineering

Presented in Partial Fulfillment of The Requirements

for the Degree of Doctor of Philosophy at

Concordia University

Montréal, Québec, Canada

December 1997

ABSTRACT

Experimental Investigations of Corona-Discharge Oxidation of Silicon

Sayed-Masoud Sayedi, Ph.D.
Concordia University, 1997

As integrated-circuit device dimensions decrease, the importance of having new reliable processes for growing MOS gate oxides becomes more and more evident. Short process times and low process temperatures are desirable features in view of tight thermal budget constraints and the need for precise location of dopants. However, conventional thermal oxidation to grow high quality films usually requires relatively long oxidation times and relatively high temperature.

Previous research on negative point (anodic) corona-processed SiO_2 films has shown that the thermal budget incurred using the corona process is much lower than in standard thermal oxidation due to the greatly enhanced oxidation rate. Promising results of low-T corona-processed ~1000Å films have shown that the films had physical characteristics comparable to those obtained in thermal oxidation. This research extends the previous work: (a) thin oxides (~200Å) are processed in order to be potentially more relevant to modern MOS processes, and (b) a more thorough electrical characterization is initiated. Electrical tests show that oxide and interface charges are comparable to thermal oxides. Breakdown characteristics are promising. The boundary between the corona-processed and control regions is found to be severely compromised. Subsequent corona treatments which overlap such boundary regions are found to restore the quality of the oxide. Fourier

Transform Infrared (FTIR) Spectroscopy results show that the negative corona films have a different structure from that of thermal oxide films. Electrical tests on positive point (cathodic) corona-processed SiO_2 films show that the electrical quality of the films is much worse than that of standard thermally grown films, grown at a similar temperature. In the interests of growing more-uniform negative-corona SiO_2 films on broader areas of silicon wafers, experiments using multi-point or multi-needle structures were conducted. The enhancement profiles of films grown in both positive and negative cases are simulated using linear-parabolic rate constants, modified to account for the corona current.

ACKNOWLEDGEMENTS

I would like to express my deepest gratitude to my thesis supervisor Dr. L.M. Landsberger for his invaluable guidance, advice, encouragement and support throughout this work. Dr. Landsberger introduced me to the world of Microelectronics technology, and through supervision of this experimental research, taught me many precious lessons that will certainly enhance my future academic work.

I also gratefully thank Dr. M. Kahrizi for his highly effective guidance, insights, and support throughout this work. I thank him for his time and attention throughout this work and, most recently, for his time in reading this manuscript.

I thank Dr. D. Landheer for his collaboration and guidance in doing FTIR tests, and work on the modelling of the corona process. His suggestions were very critical and had considerable impact on the work.

I would like to thank the personnel in the work shop and glass shop for their help in making the necessary parts for the corona apparatus. I would like to thank the people at the Department of Engineering Physics at École Polytechnique in Montreal, and The Institute for Microstructural Sciences at NRC, Ottawa, for their help at various stages of this experimental work. Also, I would like to thank all my friends in Concordia's Microelectronics Laboratory for the many fruitful discussions which we have had during the course of this work.

I gratefully acknowledge the scholarship support of Isfahan University of Technology in Iran.

This work was also supported by the Natural Sciences and Engineering Research Council of Canada (NSERC), the NRC/NSERC Research Partnership Program, and the Fonds pour la Formation de Chercheurs et l'Aide à la Recherche (FCAR).

And finally, my special thanks go to my parents who have always been a great support to me in my life. I owe special thanks to my wife Zahra, for her patience and encouragement. Her great effort in taking care of our daughters, Sara and Mina, has been invaluable in giving me the peace of mind to complete this work.

TABLE OF CONTENTS

LIST OF FIGURES

LIST OF TABLES

CHAPTER 1

Introduction and Outline

1.1 Silicon Dioxide Films and Silicon Integrated Circuits

Silicon dioxide (SiO_2) is the most important insulating film in the fabrication of semiconductor devices. SiO_2 films of various thicknesses not only satisfy critical needs during fabrication processes, but also have fundamental roles in the electrical performance of the fabricated devices and circuits.

During fabrication processes, the growth of temporary oxide layers to create intermediate structures is an essential and common practice. In this way, fabrication processes rely heavily on the convenience and repeatability of oxide properties such as growth rate, properties as a barrier to the diffusion of ions and impurities, and etching rate in different etch processes.

There are also permanent oxide layers in the final devices. The electrical performance of the devices depends on the quality of the oxide layers. The SiO_2 structure is used as an insulating layer to separate different parts of the integrated circuit. Any imperfection in this insulator leads to degradation of the electrical behavior of the circuit. Perhaps most importantly, SiO_2 films are used as dielectric layers in Metal-Oxide-Semiconductor (MOS) structures. Via this structure (mostly as the gate oxide in Metal-Oxide-Semiconductor Field-Effect-Transistors: MOSFETs), SiO_2 layers play critical roles in the performance and quality of circuits.

1.1.1 Silicon Dioxide Films and MOSFETs

For all different types of MOSFET (depletion or enhancement, N- or P- channel) the

trans-conductance gain (i_o/v_i) is mostly related to the electrical characteristics of the channel between the Drain and Source terminals. The condition of the channel is in turn determined by the applied gate voltage, the doping of the substrate and the quality and characteristics of the gate oxide and Si/SiO_2 interface [1-5]. As well, the other very important parameter of a MOSFET, V_{th}(threshold voltage), is again mostly related to the doping of the substrate and to the quality and characteristics of the gate oxide. Also, besides some well-known external effects that can change the characteristics of a MOSFET - for example the dependence of V_{th} on temperature - there are still many other not well-known effects that cause MOSFET behavior to depart from the ideal case. These effects, again, are mainly related to the quality of the gate oxide and to the material structure of its interfaces with the substrate and gate electrode [1-5]. The defects and electrical charges in the oxide and at its interfaces are the origins of those non-idealities.

If the as-fabricated characteristics of a MOSFET remained constant over time and use, the MOSFET could be used in circuits based on these as-fabricated characteristics. In that case, knowing the dependence of the as-fabricated parameters of the MOSFET on different fabrication procedures would be enough. However, the oxide charge traps and interface traps change in a varying manner during exposure to different conditions, conditions which can occur during ordinary use of a MOSFET. As a result , the MOSFET parameters become altered due to time and use, making the device unreliable. It is therefore very important to have a good understanding of real gate oxide films created by different fabrication processes, and of their degradation under different operating conditions. Finally, based on these understandings, it is important to find suitable oxidation (and fabrication) processes to create a good quality gate oxide and reliable MOSFETs which change their parameters only minimally during their use.

Research into the field of improving gate oxide quality has been very active for several decades and continues to be substantial even now [for example, references 6-10].

1.2 Research on Alternative Oxidation Processes

The reason for widespread study of gate oxide, its electrical characteristics, and its quality dependence on fabrication processes, is to discover oxidation processes by which reliable and high quality MOSFETs can be fabricated. There are many different processes which are being actively investigated. Some examples are N_2O treatments [7,10], plasma oxidation [8], and fluorine oxidation [11].

Moreover, as the dimensions of ULSI (Ultra-Large-Scale-Integration) devices continue to be scaled down, problems resulting from processes having high thermal budgets (processes using high temperatures and/or long time durations) have become the targets for more and more research. Stacking faults, warpage of large wafers, creation of Si clusters at interfaces, dopant pile up and segregation, and difficulty in confining dopants within small volumes are some well-known problems.

Thermal budget is also a critical factor in the preparation of heterostructure insulated gate field-effect transistors (HIGFETs) on silicon. In particular, the exposure to high temperatures must be restricted in the formation of pMOSFETs with compressively strained SiGe alloy channels on silicon substrates, and in nMOSFETs with tensile Si channels on relaxed SiGe alloy substrates. This is to prevent strain relaxation of the sensitive heterostructure layers [12,13]. As a result, the need for strain-controlled, lower-temperature and shorter-time fabrication processes has become more and more evident.

This need for lower-temperature and shorter-time fabrication processes has motivated many detailed investigations of low thermal budget oxidation processes as alternatives to conventional thermal oxidation processes. An understanding is necessary of

their oxide growth mechanisms and of the characteristics of the resultant oxide films.

Oxidation processes in the presence of electric fields constitute one plausible approach to create acceptable oxide films at both low temperatures and short times. The processes not only have attractively high oxidation rates at low temperatures, but also have anisotropic oxidation characteristics that could potentially be useful in solving the problem of "birds-beak" formations [14,15] , at the sides of active regions in MOS devices.

DC-bias plasma oxidation [16-19] , voltage enhanced UV assisted oxidation [20] , DC glow discharge oxidation [21] , and corona oxidation [22-31] are examples of processes which operate with an electric field across the oxide film during its growth.

The anodic oxidation of silicon in oxygen plasma was reported first by Ligenza in 1965 [32]. Since then, due to the promising aspects of the process, many similar processes have been the subject of experimental research. Corona discharge oxidation has been one of those lines of research. The work on the negative point-to-plane corona process at relatively low temperatures revealed that the process not only grows films at a substantially higher rate than does conventional thermal oxidation, but also creates films with lower refractive indices, compared to those of high temperature thermally grown films. Also, preliminary electrical characterization [26] of the film showed that the electrical quality of the films is promising.

This work aims to continue, broaden, and deepen the study of the corona-processed SiO_2 films.

1.3 Outline of This Work

This research extends the previous work on corona oxide films in several directions. The study focuses on films with lower thicknesses, potentially more relevant to modern MOS processes, and the electrical characteristics of the films are examined in more detail.

Also, the research covers other relevant topics in corona oxidation, including experimental investigation on the extension of the negative-corona oxidation method to create uniform oxide films, growth and characterization of positive-corona films, and examination of the structure of the positive and negative corona films using Fourier Transform Infrared (FTIR) spectroscopic analysis. Also, based on models proposed by other authors for the growth rate of thermal oxide films, the possible mechanisms of growth-rate enhancement of the corona films are discussed.

Chapter 2 introduces some background material concerning the fundamentals of silicon oxidation, plasma-based oxidation processes and corona-discharge oxidation. Two different models of thermal oxidation including the Deal-Grove model and the ionic-based oxidant model are covered. Then a brief description of plasma-based oxidation is introduced, followed by a description of the corona oxidation process and the basic results of previous work on negative point-to-plane corona-processed films.

Chapter 3 extends the previous characterization of negative-point corona films with a more thorough electrical characterization of thinner negative-point corona processed oxides. Both corona-grown and corona-treated films are examined. Also, a detailed study of the edge area of the corona region by using a two-step corona procedure is presented. The distinct electrical characteristics of the negative corona films at their boundaries with control oxide areas, are shown in these results.

Chapter 4 presents efforts to produce uniform negative-point corona oxide films over larger areas. The strategy and procedures involved in using a grid of needles anisotropically etched in a piece of Si wafer (instead of the platinum needle) is described. Experimental results using the structure are presented, followed by discussion on the features that are seen in the experiments and results.

Chapter 5 presents positive-point experiments and results. Along with some thickness

profiles of the films, refractive indices and C-V results of the films are presented. The different behavior of positive corona films is examined closely and compared to that of negative corona films.

Chapter 6 presents the results of Fourier-Transform-Infrared Spectroscopic Analysis on both positive- and negative- corona films. It is necessary to invoke a different bulk oxide network structure for negative corona oxide films to explain the results.

Chapter 7 investigates the oxidation rate enhancement features in both positive and negative corona oxidation and treatment. By suggesting modification to the parameters of the linear-parabolic model, numerical simulations of enhancement profiles are presented. Simulation results are compared to the experimental results. Different interpretations of the growth mechanisms are presented.

Chapter 8 finally summarizes the main results and conclusions of this work, followed by suggestions on directions for future work on the corona process.

CHAPTER 2

Background

2.1 The Thermal Oxidation Process

As background for this experimental investigation of silicon oxidation, two models proposed for conventional thermal oxidation are briefly reviewed. The first model is based on the assumption that in thermal oxidation, neutral oxygen molecules are the oxidant species. The second model, in contrast, is based on the assumption that negative oxygen ions are the oxidant species. Through this brief review, the basic concepts of the oxidation process are presented. Also, the parameters introduced in the models are used later in Chapter 7, in the discussion of corona oxidation mechanisms.

2.1.1 The Deal-Grove Linear-Parabolic Model

The Deal-Grove [33] linear-parabolic model of thermal oxidation is based on the assumption that neutral oxidant molecules (O_2 in dry oxidation, and H_2O in wet oxidation) are the main oxidizing species in the oxidation process. The gradient in the oxidant concentration causes diffusive flow through the already-grown film, toward the Si/SiO_2 interface. There, the reaction of the oxidant with the silicon atoms of the substrate produces SiO_2. This newly formed oxide at the interface lifts the already existing oxide above it. Fig.2.1(a) shows the oxidant flow at different regions; the flow from the ambient gas into the oxide film (F_1), the flow through the oxide film (F_2), and finally the flow from the film toward the silicon substrate (F_3) where the oxidant is consumed by the reaction with Si atoms and creation of new oxide. Fig.2.1(b) shows the concentration of the oxidant at

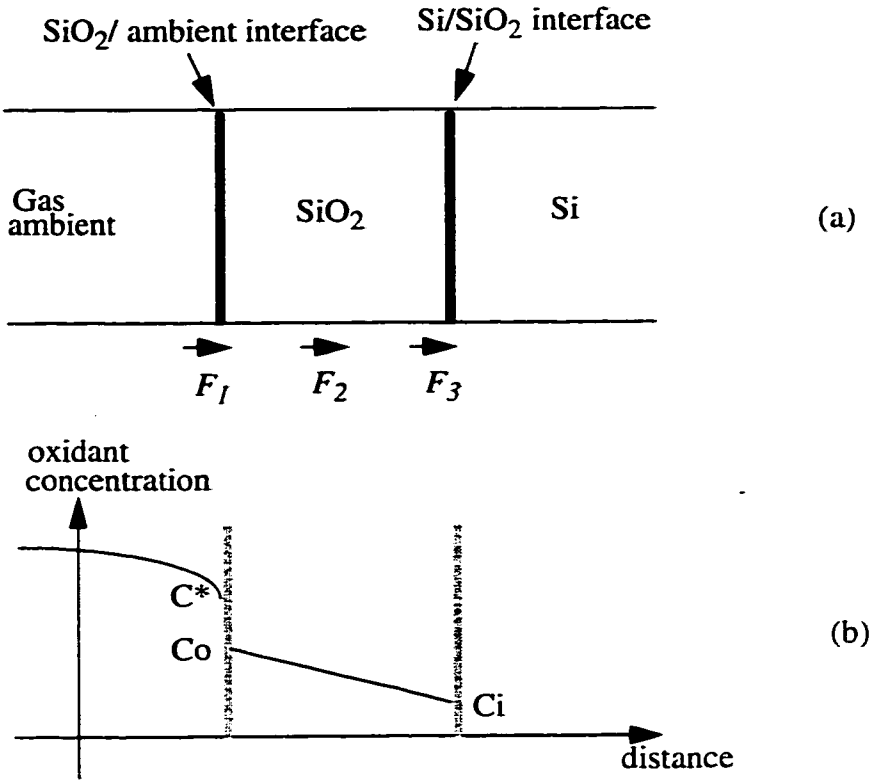

Fig. 2.1: a) The flow of oxidant during an oxidation process; b) The profile of oxidant concentration at different locations during the process.

different regions. The model assumes a steady-state condition that requires:

$$F_1 = F_2 = F_3 = F \tag{2.1}$$

where F is the flux of the oxidant that determines the film growth rate as follows:

$$\frac{dX_{ox}}{dt} = \frac{F}{M_{ox}} \tag{2.2}$$

where X_{ox} is oxide thickness, t is the oxidation time, and M_{ox} is the number density of oxidant molecules structurally incorporated into a unit volume of the growing oxide network.

The three fluxes F_1, F_2, and F_3 can be expressed separately based on their physical definitions:

$$F_1 = h(C^* - C_o) \tag{2.3}$$

$$F_2 = D\frac{C_o - C_i}{X_{ox}} \tag{2.4}$$

$$F_3 = k_i C_i \tag{2.5}$$

where :

h=gas phase mass transfer coefficient (cm/sec)

C^*= equilibrium concentration of the oxidant in the oxide ($1/cm^3$)

C_o= concentration of the oxidant in the surface of the oxide ($1/cm^3$)

D= effective diffusion coefficient of oxidant in the oxide(cm^2/sec)

C_i= oxidant concentration near the Si/SiO_2 interface ($1/cm^3$)

K_i=chemical reaction rate constant at Si/SiO_2 interface

(In Eq.(2.4) it is assumed that oxidant concentration in the oxide is a linear function of the distance from the oxide surface.)

After solving the above equations, the following equation relates the growth rate to the system parameters:

$$\frac{dX_{ox}}{dt} = \frac{F}{M_{ox}} = \frac{C^*/M_{ox}}{\frac{1}{K_i} + \frac{1}{h} + \frac{X_{ox}}{D}} \tag{2.6}$$

By assuming an initial value of X_{in} for X_{ox}, solving Eq.(2.6) yields:

$$(X_{ox})^2 - (X_{in})^2 + A(X_{ox}) - A(X_{in}) = Bt \tag{2.7}$$

or;

$$X_{ox} = \frac{A}{2}\left(\sqrt{1 + \frac{t+\tau}{A^2/4B}} - 1\right) \tag{2.8}$$

where:

$$B = \frac{2DC^*}{M_{ox}} \tag{2.9}$$

$$B/A = \frac{C^*/M_{ox}}{\frac{1}{k_i} + \frac{1}{h}} \tag{2.10}$$

$$\tau = \frac{X_{in}^2 + AX_{in}}{B} \tag{2.11}$$

Eq.(2.8) shows that for the condition of ($t+\tau << A^2/4B$) the equation can be approximated as:

$$X_{ox} \cong \frac{B}{A}(t+\tau) \tag{2.12}$$

and for the condition ($t+\tau >> A^2/4B$), it can be approximated as:

$$X_{ox}^2 \cong B(t+\tau) \tag{2.13}$$

Equations (2.12) and (2.13) show that oxidation on bare silicon starts with a linear growth rate governed by the rate constant B/A, and then later the condition is dominated by a parabolic growth rate governed by the rate constant B. The dependence of the two rate constants on the physical parameters of the system is shown in Equations (2.9)and (2.10). As the equations show, the oxidant concentration in the oxide at the surface, and the reaction coefficient, control the growth rate in the linear regime, while the diffusivity of the oxidant in the film and, again, the oxidant concentration in the oxide at the surface, control the growth rate in the parabolic regime.

2.1.2 The Ionic Growth Model

Since the linear-parabolic model was proposed in 1965 by Grove and Deal [33] , it has been the most widely accepted model for thermal oxidation. However, because of its shortcomings in fitting and explain some features of the experimental results, research on oxidation modeling still is highly active. One proposed model, with a completely different view of the oxidation mechanism, is the ionic growth model proposed by Wolters *et al.* [34]. The model explains many features that are experimentally seen in thermal oxidation. In this model, charged oxygen ions are the oxidant species during oxidation. The following is a brief description of the model.

The following development follows relatively closely the derivation in the work of Wolters *et al.* [34]. Based on Wagner's theory of metal oxidation [34,35] the general expression for the flow of charged particles inside an oxide layer is given by:

$$J_i = \frac{-D_i C_i}{kT}\left(\frac{d\mu_i}{dX} - z_i q E\right) = \frac{-\sigma_i}{z_i^2 q^2}\frac{d\mu_i}{dX} + \frac{\sigma_i}{z_i q}E \qquad (2.14)$$

where C_i is the oxidant particle concentration, D_i is the diffusion coefficient of oxidant particles, $\mu_i = kTln(C_i)$ is the thermodynamical potential, E is the electric field, X is the location in the oxide layer, σ_i is the conductivity, and z_i (=2 for O^{2-} ions) is the charge of the species in units of the electron charge q(= $-1.6 * 10^{-19}$ Coulomb).

Based on the ionic growth model, there are two different charged carriers moving in opposite directions during the thermal oxidation process (Fig.2.2). Applying the above equation to the oxygen ions (by replacing subscript i with *ion*: $z_i \equiv z_{ion}=2$, $J_i \equiv J_{ion}$; $C_i \equiv C_{ion}$, $\sigma_i \equiv \sigma_{ion}$, ...) shows that there are two separate terms that determine the flow of ionic oxidants through the oxide film: the thermodynamical term (the first term that includes μ_i), and the electrical term (the second term that includes E).

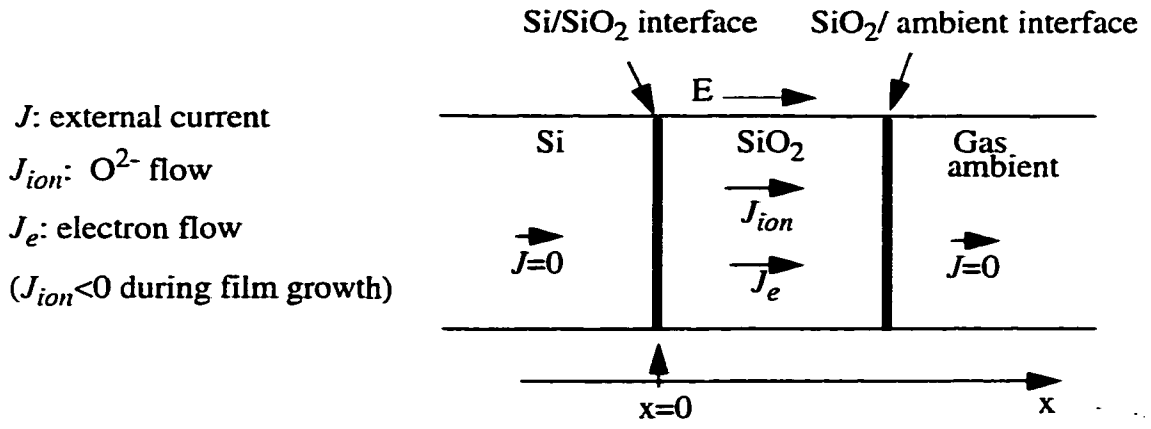

Fig. 2.2: Flow of charged particles in growing oxide film during its growth.

Based on the coordinate system shown in the Fig.2.2, the necessary condition for oxidation is $J_{ion}<0$. Eq.(2.14) shows that in the case where there is an existing negative electric field, ($E/q>0$), increasing the magnitude of E could cause a complete stopping of oxidation. For the case of positive electric field ($E/q<0$), the two terms in Eq.(2.14) have the same sign (negative), which would tend to enhance the growth.

Using the equilibrium condition of $O_2 + 4\,e^- = 2O^{2-}$ results:

$$\frac{d\mu_{o2}}{dX} = 2\frac{d\mu_{ion}}{dX} - 4\frac{d\mu_e}{dX} \tag{2.15}$$

In conventional thermal oxidation, the net electrical current is zero, therefore:

$$J = 2qJ_{ion} + qJ_e = 0 \tag{2.16}$$

substituting J_{ion} and J_e from Eq.(2.14) in Eq.(2.16), and then substituting $d\mu_e/dx$ from Eq.(2.15) gives the expression for the ionic oxidant flux.

$$J_{ion} = \frac{-(\sigma_e^{-1} + \sigma_{ion}^{-1})^{-1}}{8q^2}\frac{d\mu_{o2}}{dX} \tag{2.17}$$

Based on Wolters' model the magnitude of σ_{ion} is not constant over all the oxide, and it

decreases near Si/SiO_2 interface due to a high local electric field caused by Q_f in that region. Considering two different ionic conductivities, one for the region near the Si interface, (σ_1), and one for the remaining region, (σ_2), yields:

$$\sigma_{ion}^{-1} = \sigma_1^{-1} + \sigma_2^{-1} \tag{2.18}$$

In the case of having σ_1 much smaller than σ_2 the overall ionic conductivity will be determined by σ_1. Wolters *et al.* [34], derives an approximate equation for σ_{ion} that shows the effect of Q_f on ion conductivity:

$$\sigma_{ion} = \sigma_o \left(1 + \left(\frac{(X_{ox})/e}{X_Q}\right)^{-\alpha}\right)^{-1} \tag{2.19}$$

where X_Q is the distance between the Q_f layer and the Si/SiO_2 interface, and $\alpha = \ln(\sigma_2 / \sigma_1)$. Using equations (2.17) and (2.19), knowing that $J_{ion} = - M_{ox} dX_{ox}/dt$ (M_{ox} as defined before for Eq.(2.2)), and substituting $d\mu_{o2}/dx$ with $\Delta\mu_{o2}/X_{ox}$, gives the following power-parabolic growth rate:

$$(X_{ox})^2 - (X_{in})^2 + \hat{A}(X_{ox})^{2-\alpha} - \hat{A}(X_{in})^{2-\alpha} = \hat{B}t \tag{2.20}$$

where X_{in} is the initial thickness of the film and:

$$\hat{A} = \frac{2}{\left(\frac{1}{\sigma_e} + \frac{1}{\sigma_o}\right) \cdot \sigma_o \cdot (eX_Q)^{-\alpha} \cdot (2-\alpha)} \tag{2.21}$$

$$\hat{B} = \frac{\Delta\mu_{O2}}{4 \cdot q^2 \cdot \left(\frac{1}{\sigma_o} + \frac{1}{\sigma_e}\right) \cdot M_{ox}} \tag{2.22}$$

Comparison of Eq.(2.7) extracted in the linear parabolic model, and Eq.(2.20) extracted in the ionic growth model shows that for the case of α=1 both models yield the

same equation. However the defined parameters and oxidation mechanisms are completely different in the two models.

2.2 Plasma-Based Oxidation Processes

Although the oxidation of silicon via thermal oxidation processes is a well-established fabrication technique, shrinking the device dimensions creates the need to use oxidation processes with lower thermal budgets. Plasma oxidation is such a process that is explored as an option by many researchers.

The formation of an oxide on a semiconductor surface immersed in an oxygen plasma is called plasma oxidation. In plasma-enhanced chemical vapor deposition (PECVD), reactive oxidant species are generated in the plasma ambient. During the oxidation, the sample surface is at a floating potential and no current flows through the oxide. In this configuration, the oxidation rate at low temperatures is higher than that of conventional thermal oxidation. The oxidation rate can be increased by electrically biasing the sample; the growth can be stimulated if the sample substrate is biased so that the sample surface potential is above the floating potential. This oxidation process is usually called positive-biased plasma, or anodic plasma oxidation. When the surface potential is below the floating potential, which is called cathodic plasma oxidation, the rate of oxidation is lower, and at certain conditions of voltages and oxide thicknesses, the oxidation is stopped [18]. It has been shown that anodic plasma oxides have much better electrical characteristics compared to those of cathodic plasma oxides [18].

Fig.2.3 shows an example of a plasma anodization system reproduced from Ref. [36]. As the figure shows, the wafer is connected to the positive terminal of the power supply. By changing the polarity of the power supply the oxidation process could be changed to cathodic plasma oxidation. In the case where there is no electrical connection to the sam-

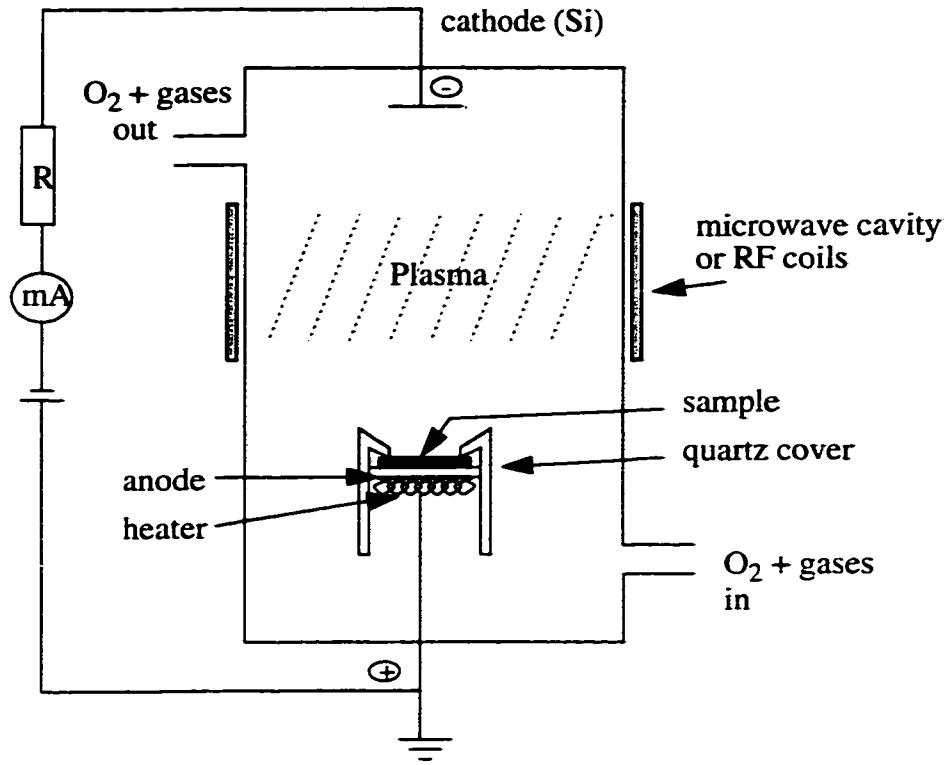

Fig. 2.3: An example of a plasma anodization system, reproduced from Ref. [36].

ple (floating condition), it would be unbiased plasma oxidation .

2.2.1 Corona Discharge Oxidation

As a novel method to create SiO_2 films, low-temperature (600°C-900°C) corona-discharge oxidation has been the subject of several previous publications [22-30]. Reference [23] compared point-to-plane corona discharge processes in negative-point (anodic) and positive-point (cathodic) configurations, and found dramatic differences in the resulting oxide thickness profiles. References [24-30] studied negative-point corona oxidation extensively. The study revealed some promising characteristics of the process and of the grown oxide films: the method dramatically affects not only the oxidation rate but also the film properties [26]. Negative-point-to-plane corona-oxidation greatly enhances the oxidation rate, at low temperatures such as 600-800°C [26]. It was also shown

that such low-temperature corona-processed ~1000Å films had physical characteristics comparable to those obtained in thermal oxidation at substantially higher temperature. The corona process, at T=600-900°C, produces SiO_2 films having a refractive index (density) comparable to that of high-temperature-grown thermal oxide (>1000°C for wet oxidation, and >1150°C for dry oxidation) [26]. This occurs whether the film was grown completely by corona, or whether the film was thermally grown and then subjected to a short corona treatment. This altered network structure was confirmed by substantially enhanced diffusivity through such corona-relaxed oxide layers [28]. Also, it was found that for low-temperature corona-processed ~1000Å films, densities of fixed oxide charges and of interface states at midgap, were lower (better) than expected, and were comparable to those of thermal oxides grown at those temperatures.

2.2.2 Point-to-Plane Corona Apparatus

Fig.2.4 shows a simplified schematic of the corona-discharge apparatus. A more

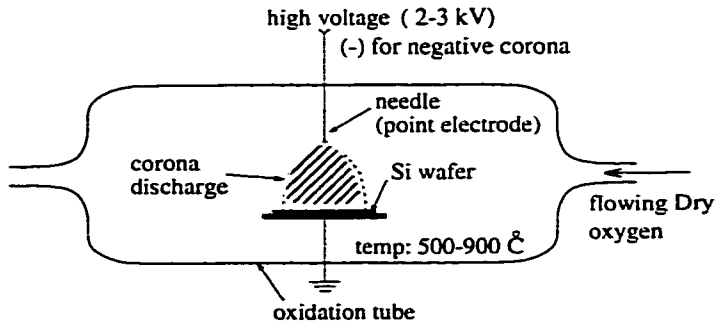

Fig. 2.4: Simplified schematic of the Corona-Discharge apparatus.

detailed illustration of the apparatus is shown in Appendix A [22,26,37]. The apparatus is constructed exclusively of quartz, sapphire, thin platinum wire and silicon wafer, and resides in a standard oxidation furnace at atmospheric pressure. Corona processing is done in flowing dry O_2 at T=600°C - 900°C. During oxidation an electric current is induced in a silicon wafer via a point-to-plane corona discharge. A platinum needle (the point) that is connects to the power supply by a platinum wire, is suspended above the front side of a silicon wafer (the plane). The back side of the silicon wafer is electrically grounded. By using a custom-designed electronic circuit to power and control the voltage or current of the needle, the apparatus can be used to do either positive or negative corona processes, under either constant-current, or constant-voltage conditions. As schematically shown in Fig.2.4, a negative voltage applied to the needle produces a "bell" shaped beam of ions between a point electrode and a silicon wafer.

2.2.3 Negative-Point Corona Baseline Experiments and Results

Fig.2.5 (from reference [26]) shows the effect of negative corona treatment on already existing bulk oxide; Fig.2.5 (a) shows the profiles of thickness and refractive index and Fig.2.5 (b) shows a top view schematic of the sample. The approximately "bell" shaped thickness profile on top of the control thickness is a result of the point electrode structure used in the Corona-Discharge apparatus (Fig.2.4). As the refractive index profile shows, the corona-treated region has lower refractive index which means the oxide has lower density and likely less bond strain.

In general, the refractive index of thermally-processed SiO_2 films increases with decreasing growth temperature, as seen in Fig.2.6. For both wet and dry oxides, there is a well defined break point in temperature, above which the refractive index reaches a minimum value and does not change any more. These break points are at about 1150°C for

(a)

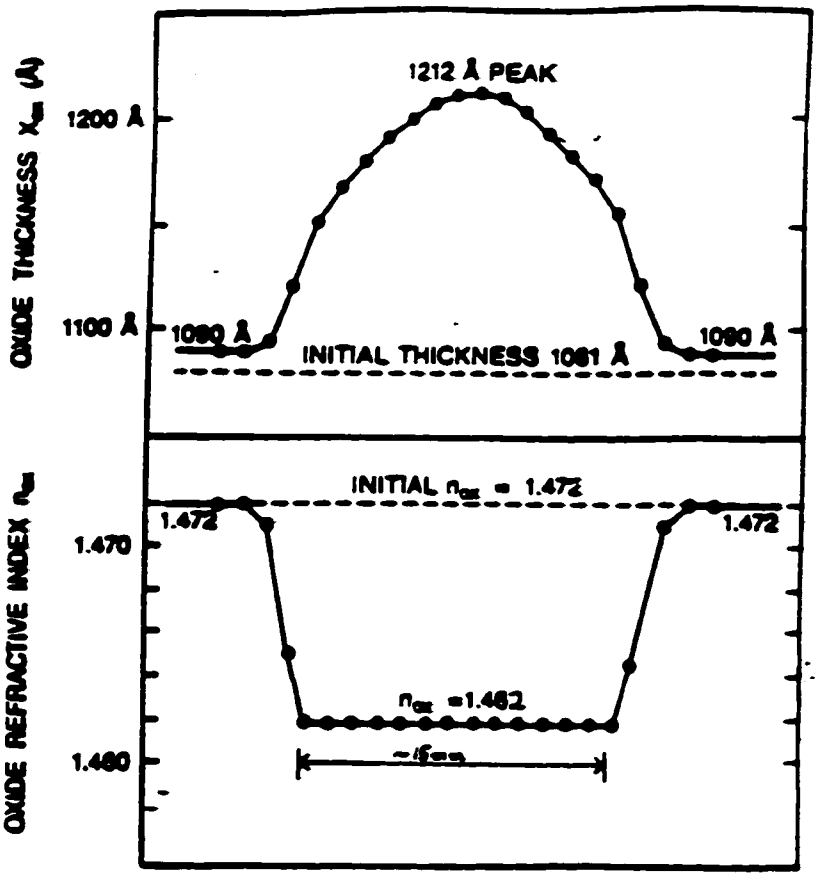

(b)

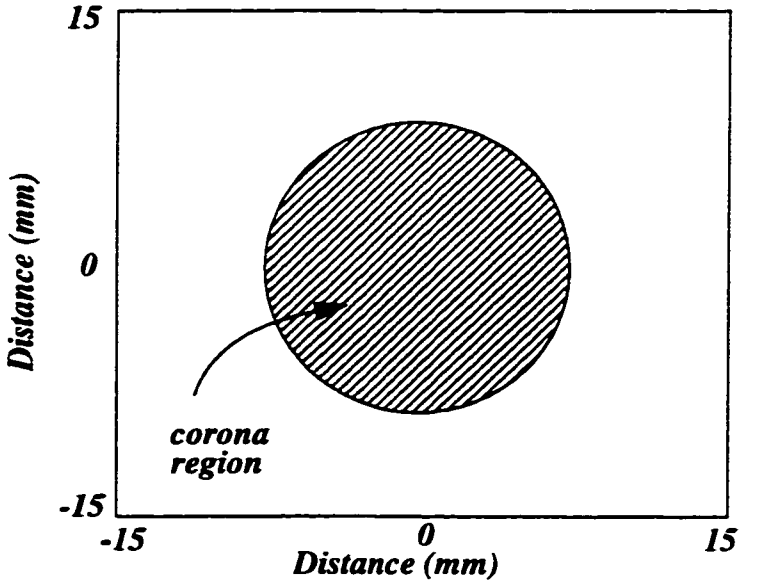

Fig. 2.5: (a)- X_{ox} and N_{ox} profiles for a <111> 800°C grown SiO_2 film relaxed by negative corona in dry O_2 ; Needle current=-4μA , T_{cor} (temperature during corona treatment) =800°C and t_{cor} (time of corona treatment)= 20 minutes. (b)- Top view diagram of the sample. (The horizontal axis shows distance from the point on the wafer immediately below the needle.)[26]

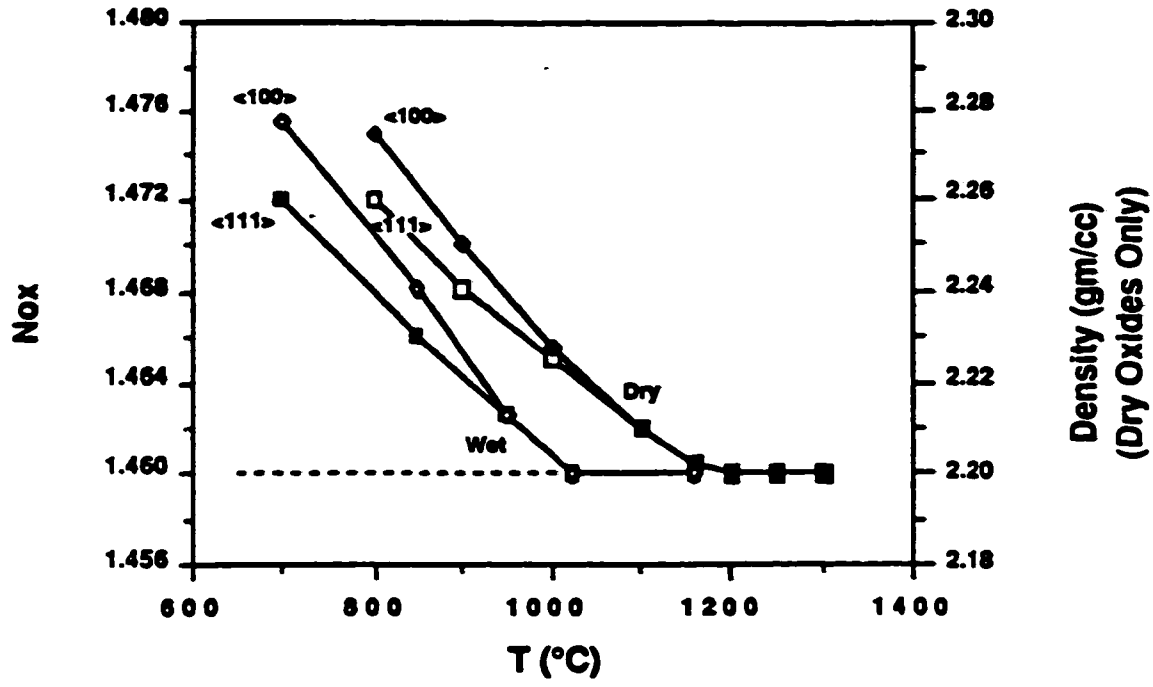

Fig. 2.6: Refractive index vs. growth temperature for wet and dry oxide and density for dry oxides on Si. (<100> and <111> on figure refer to the orientation of the Si surface.)[26]

dry oxidation, and at about 1000°C for wet oxidation (Fig.2.6). As Fig.2.5 shows, however, corona processed films attain at 800°C the refractive index (1.462) of high temperature thermal oxide films.

Fig.2.7 [26] shows two examples of profiles of thicknesses and refractive indices of oxides grown in the Corona-Discharge apparatus. As the figure shows, the refractive indices in the corona region are lower than the values expected for those oxidation temperatures. Also, comparison of the thicknesses of oxides in corona regions and control regions demonstrates again that negative corona oxidation increases the rate of oxidation.

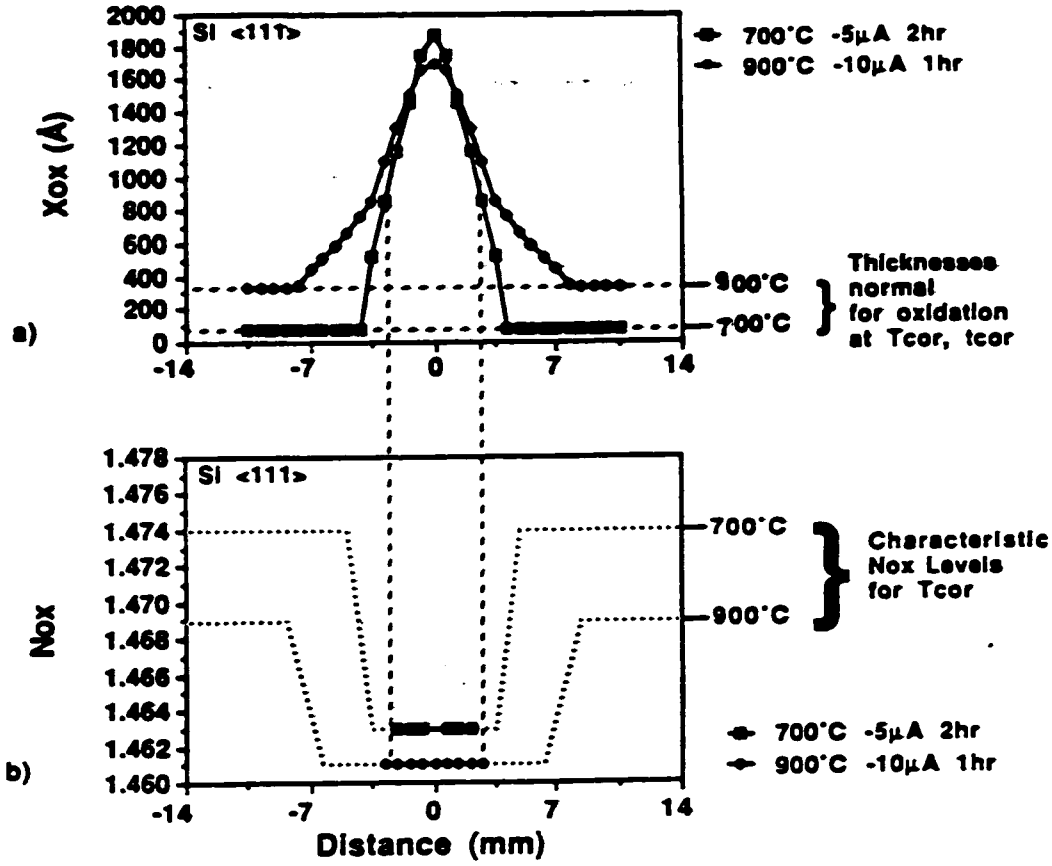

Fig. 2.7: X_{ox}(a) and N_{ox}(b) profiles for two oxygen-corona-grown films. 1- T_{cor} (temperature of corona oxidation)=900°C , t_{cor} (time of corona oxidation)=1hr and the current of needle=-10μA (negative corona) 2- T_{cor}=700°C , t_{cor}=2hrs, current=-5μA (negative corona).[26]

The previous electrical test results on negative-corona treated oxides show that the relaxed corona oxide has quality comparable with oxide grown by standard thermal oxidation. Fig.2.8[26] shows typical Q_f and D_{it} for corona treated oxides. The figure shows, for three different temperatures of corona treatment, the Q_f and D_{it} of treated regions are close to the values of oxide grown at 800°C by standard thermal-oxidation. Also, for

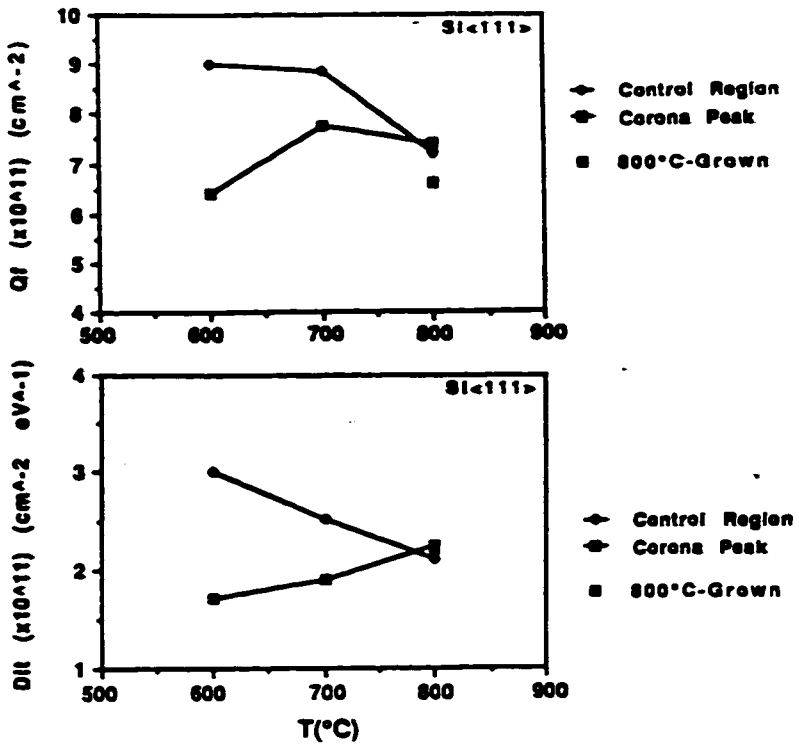

Fig. 2.8: D_{it} and Q_f as a function of corona treatment temperature.[26]

600°C and 700°C corona treatments, the values of Q_f and D_{it} of the corona regions are lower than those of control regions, which indicates potentially higher-quality oxide in the corona regions.

A negative point-to-plane corona discharge method has also been used in growing thin (~7.5 nm) SiO_2 films at room temperature [31]. However the electrical quality of these room-temperature films was found to be much lower than that of thermal oxide films grown at higher temperatures such as 800°C [31].

2.2.4 Positive-Point Corona Baseline Experiments and Results

The polarity of the voltage applied on the needle in the corona apparatus can be reversed, to create a positive point-to-plane corona. The thickness profiles of positive corona films have been reported previously by Modlin [22]. It has been shown that in positive corona, compared to negative corona, the process affects a much wider region of the

wafer. Also in contrast to the negative corona, in most positive-point cases the center region immediately below the needle has lower thickness compared to its surrounding region. Only in very thin films does the center region have the highest thickness. However, even in these cases the affected corona region is still much wider than that of the negative corona. Fig.2.9 (from reference [22]) shows some examples of thickness profiles of the positive corona oxidation process. As the figures show, the profiles are completely different from those of negative corona process shown in Figs. 2.5 and 2.7. It was suggested that the two corona processes produce different kinds of ions in the oxygen ambient. In positive corona, the positive voltage of the point electrode produces positive ions, while in negative corona, the negative voltage of the point electrode produces negative ions [37].

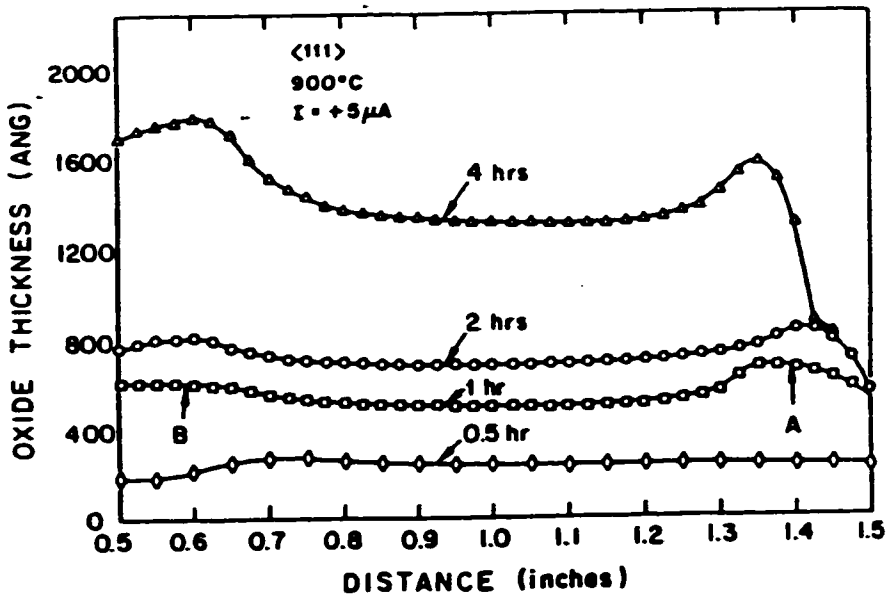

Fig. 2.9: Examples of thickness profiles of films grown in the positive corona oxidation process.[22]

CHAPTER 3

Characterization of Thin Oxides Created by Negative Point-to-Plane Corona

3.1 Introduction

Promising results of low-temperature corona-processed ~1000Å films showed that the films had physical characteristics comparable to those obtained in thermal oxidation. It has been shown that for ~1000Å films, Q_f and D_{it} of corona-processed regions were potentially better than those of the thermal oxide regions. This was generally attributed to the corona process beneficially affecting the oxide and interface structure in a structural relaxation phenomenon which was related to measured refractive index changes[26]. The work presented in this chapter extends the previous work in two directions: (a) thin oxides (~200Å) are processed in order to be potentially more relevant to modern MOS processes, and (b) a more thorough electrical characterization is initiated. In the thinner films considered in this work, it is not practical to accurately measure the refractive index by ellipsometry [26]. But the same relaxation phenomenon is expected to be in effect, again with beneficial effects on oxide and interface quality. Thus, the electrical properties are studied in more detail below.

3.2 Creation of Films and Test Structures

N-type <100> wafers with resistivity of ~10 ohm-cm underwent the reverse RCA cleaning procedure (Appendix B). Four different types of thin (~150-250Å) oxides were used for this investigation:

(a) Corona-grown oxides were prepared by using a point-to-plane apparatus in a stan-

dard thermal oxidation tube [23,26,27,29,33]. The oxidation temperatures were 600°C, 700°C, and 800°C and the time of corona growth was 25 to 35 minutes. A top view of the different regions of these grown oxide films is shown in Fig.3.1(a). Fig.3.1(b), curve (*a*), shows the typical thickness profile as a function of distance across the wafer. The time, temperature, and corona current for this profile were 25 minutes, 800°C, and -2μA respectively. The corona-affected region is approximately 7-8 mm in diameter and the center region of the oxide has a peak thickness about 210Å. The thickness of the thin ~50Å oxide in the surrounding region (region *(ii)*) is consistent with conventional thermal oxidation at 800°C for 25 minutes in dry O_2.

(b) Corona-treated oxide films were prepared in a two-step process. First, an initial oxide film with thickness of slightly less than 200Å was grown on bare silicon using conventional dry thermal oxidation at 800°C for 5 hours and 15 minutes. Next, the wafer was subjected to a corona treatment for 2 minutes -2μA corona current, also at 800°C. In this way the corona-treated region is only slightly (0-20Å) thicker than the surrounding, corona-unaffected region. Fig.3.1(b), curve(*b*), shows the thickness profile, compared to that of case (a) above.The top view of the different regions for this case is the same as that of case (a) shown in Fig.3.1(a).

Previous research [26] on the negative corona process showed that the number of oxygen atoms incorporated into the SiO_2 structure due to the corona process is relatively close to the number of electronic charges which pass through the film due to the integrated corona current. This was verified in Appendix A for two cases of these thin oxides.

(c) Oxide having two overlapped corona treatment regions: These are thin oxide films grown by conventional thermal oxidation and then subjected to two short sequential negative-point corona treatment steps, affecting overlapping but not coincident regions. After the end of a first corona treatment (as described in case (b) above), the wafer was moved

(a)

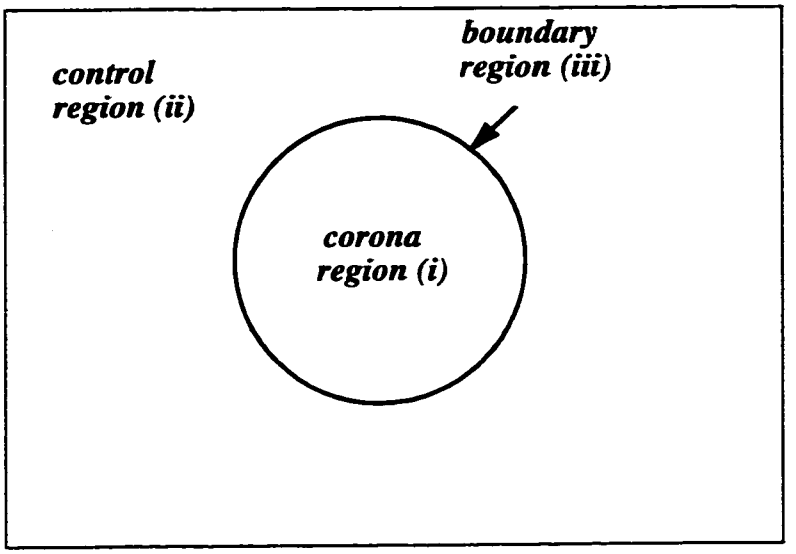

(b)

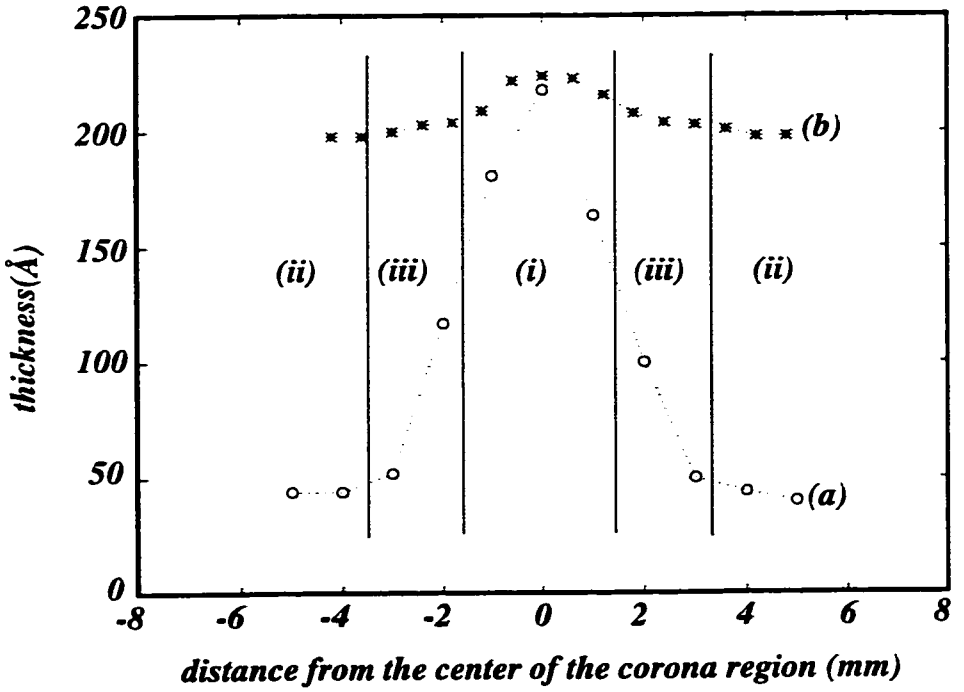

Fig. 3.1: (a)- Top view profile of different regions of corona or corona-treated oxide films (b)-Typical thickness profiles of (*a*) corona-grown and (*b*) corona-treated oxide.

(a)

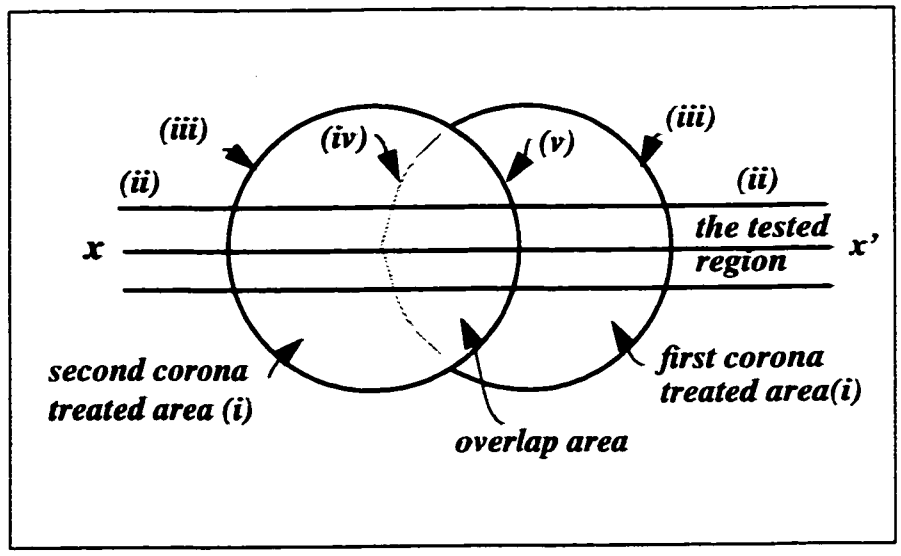

(b)

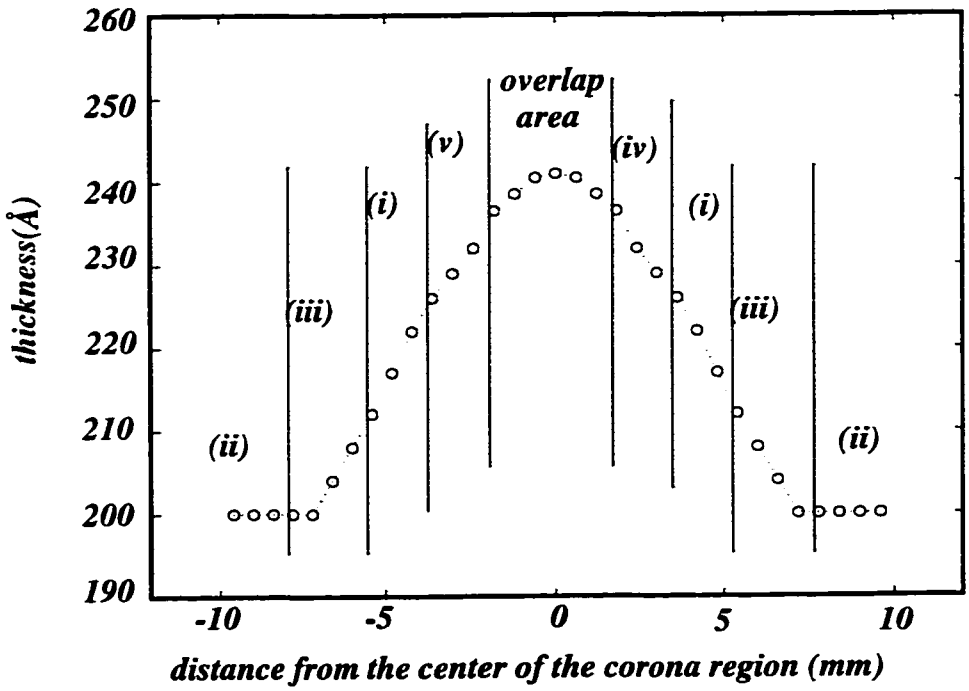

Fig. 3.2: (a)-Top view profile of different regions of two-step corona-treated oxide film. (b)-Typical thickness profiles of two-step corona-treated oxide.

laterally slightly, so that the needle of the corona apparatus became located nearer to the edge of the already corona-treated region. A top view of this scheme is depicted in Fig.3.2(a). In this new position, another 2-minute corona treatment was done at 800°C under the same conditions as the first treatment. Fig.3.2(b) shows the typical thickness profile as a function of distance across the wafer.

(d) Two sources of control oxide were used: (i) oxide films grown by conventional dry thermal oxidation, and (ii) the untreated areas surrounding the corona-treated region. For these areas, film with thickness of about 200Å was grown on bare silicon using conventional dry thermal oxidation at 800°C for 5 hours and 15 minutes.

After the films were fabricated in one of the above four cases(a-d), metallization and patterning (using a shadow mask, or a photoresist and lithography procedure) was done to create MOS capacitors. The samples underwent an anneal at 400°C for 10 minutes in an ambient of 80% N_2 and 20% H_2 .

To suppress potential effects of other (unrelated) process factors in drawing conclusions on the quality of corona-grown and corona-treated oxide films, the test results of control oxides created in this laboratory were used for comparison. Aside from the oxide growth method, all other process steps such as cleaning, metallization and annealing were common to all types of oxide studied. The details of the different fabrication procedures are presented in Appendix B.

Cases (a) and (b) above yield 3 regions of interest, as seen in Fig.3.1 : (i) the central corona-treated region (approx. 6-10mm diameter, bell-shaped profile); (ii) the outer, untreated control region (which grows by standard thermal oxidation); and (iii) the circular region at the boundary between (i) and (ii).

Case (c), as shown in Fig.3.2 , yields more different types of regions. The figure shows two more types of boundary regions compared to the boundary region (iii) shown

in Fig.3.1 for cases (a) and (b). For the overlapped case, in addition to the overlap area and representative regions (i),(ii) and (iii), there are: (iv) a boundary region subsequently corona-treated, and (v) a corona-treated region which is on a boundary of a subsequent corona treatment.

While breakdown tests on both corona-grown (case a) and corona-treated (cases b,c) oxides are of interest, corona-treated oxides were used for most of the electrical stress tests. The two reasons for this choice are: (1) Previous studies of negative point corona processes [26] showed that short-time corona treatment of an oxide film grown at low temperature alters the film structure such that its properties are similar to those of films grown by corona process on bare silicon; (2) In order to draw even tentative conclusions from breakdown tests, many tests are needed at locations having the same thicknesses. The present corona apparatus creates oxide films with a rather bell-shaped thickness profile, with maximum in the center of a circular affected region having diameter ~5-10mm [23,26,27,29]. The central peak of the profile, is the area of most interest and potentially of the highest quality. However, for case (a) the oxide thickness in this center region varies too much to obtain enough breakdown tests at a particular thickness in that region. For comparison, Fig.3.1(b) also shows that the thickness profile of corona-treated oxide is much more uniform. Thus, in order to obtain more useful breakdown statistics, corona-treated oxides were used.

The reason for using the two-step corona-treatment procedure to produce wafers of case (c), will be discussed later in Section 3.8.

3.3 Electrical Measurement Techniques

HP4284A (Precision LCR meter) and HP4140B (pA meter / DC Voltage Source) instruments were used to do high frequency (HF) and low frequency (LF) C-V measure-

ments to find Q_f and D_{it}. An HP4145 parameter-analyzer was used for constant-voltage I-t tests to evaluate the reliability of the corona oxides. A constant-voltage Fowler-Nordheim stress of +8MV/cm was applied to the gates of both control and corona samples. The backside substrate metal was connected to ground. During the electrical stress, the gate current was monitored in order to calculate the build up of the bulk charges[40]. At certain intervals during the stress, C-V measurements were used to measure ΔD_{it} and ΔQ_f [1,40,41].

Also, a HP4145 parameter-analyzer was used to apply constant-current time-dependent dielectric breakdown (TDDB) tests. The backside substrate metal was connected to ground and a positive constant current of $17*10^{-5}$ A/cm^2 was applied to the gate. The voltage of the gate during the test was positive and it kept the N-type substrate of the MOS structure in the accumulation region. By monitoring the gate voltage during the test, the time-to-breakdown (t_{bd}), was observed. t_{bd} was defined as the time to the first abrupt drop in voltage across the capacitor, not necessarily the complete destruction of the film. In some cases, after the sudden drop of voltage at t_{bd}, considerable voltages still existed on the gate electrode. The value of Charge-to-breakdown (Q_{bd}) was obtained by calculation using the values of gate current and t_{bd}.

In ramp-voltage (Time-Zero Dielectric Breakdown (TZDB)) tests, the gate voltage was positive with a ramp rate of 1V/s, and the substrate metal electrode was grounded. This test was used to examine the robustness of the as-grown oxide films[42] .

(More background and detail on electrical measurements is given in Appendix B).

3.4 Measured Q_f and D_{it}

Fig.3.3 shows the typical profiles of Q_f and D_{it} of a oxygen-corona-grown film . The figure shows that in the central region of the oxide Q_f and D_{it} are minimum, and that they

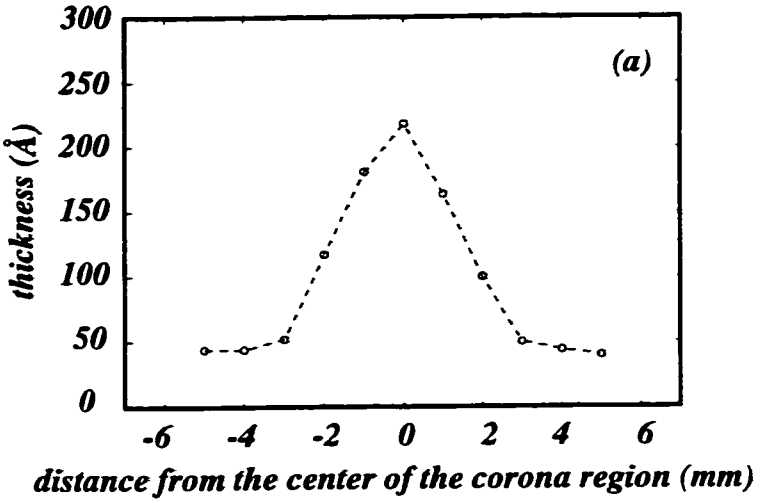

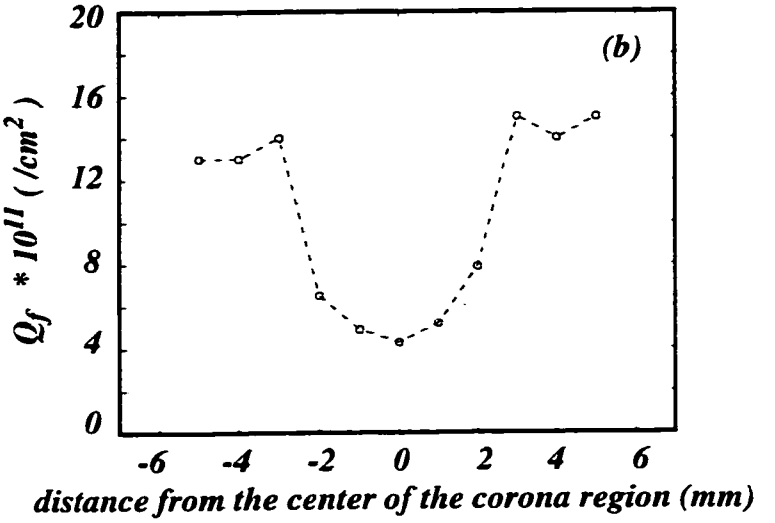

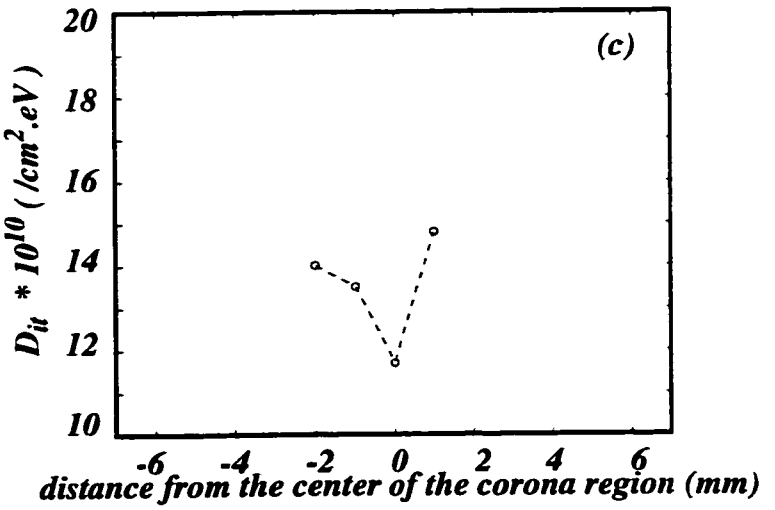

Fig. 3.3: The profiles of (a): X_{ox}, (b): Q_f and (c): D_{it} for a oxygen-corona-grown film, processed at T=800°C for 25minutes at -2μA.

increase farther from the center. As was mentioned before, one possible reason for this phenomenon is the fact that the center region of the oxide is completely relaxed (refractive index =1.46) or at least more relaxed than the surrounding areas.

Because the center regions of the corona-grown oxides are likely to be the most interesting regions, for comparison, the Q_f and D_{it} of the control oxides with the range of thicknesses comparable to those of the center regions of the corona oxides (~200Å films mentioned in case (d) of previous section) were measured as well. Table 3.1 summarizes the results of the measurements. Some published values of Q_f and D_{it} in the literature [1,3,4,43] for standard oxidation at similar temperatures and ambients are shown in parentheses.

As the table shows, the values of Q_f of corona oxides follow the same temperature dependence that exists for oxides grown by standard oxidation (that is, lower temperature

TABLE 3.1: Q_f and D_{it} from C-V measurements.

	Corona @ 600°C in dry O_2	Corona @ 700°C in dry O_2	Corona @ 800°C in dry O_2	Standard thermal oxidation @ 800°C in dry O_2 (≅160Å)	Standard thermal oxidation @ 900°C in dry O_2 (≅200Å)	Oxidation @900°C in dry 50% O_2 and 50% N_2 (≅170–210Å)
Q_f (*e11) /cm^2	10-12 (5-8)	7-8 (4-5)	3.5-5 (2-4)	5-6.5 (2-4)	2.5-4 (1-2)	1-2.5 (1)
D_{it} (*e11/ cm^2.eV	0.6-1.5	0.4-0.61	0.3-1.5 (0.3)	0.8 (0.3)	1.3 (1.2)	0.4

Note: some published values of Q_f and D_{it} from the literature [1,3,4,43] for standard oxidation at similar temperatures and ambients are shown in parentheses.

results in higher Q_f [1]). Also, at each oxide temperature the values for both corona and standard oxidation are in the same range. However, the time of oxidation for the two methods are completely different. For example, growing a 160Å oxide film in dry O_2 at 800 °C by standard oxidation takes about 5 hours, but by negative-corona oxidation and using a current of 2μA , it takes about 15 minutes. The fact that the thermal budget incurred by using the corona method is much lower than the usual dry oxidation and the fact that we can obtain the same ranges of Q_f and D_{it} which depend on the temperature of the oxidation, point to the potential usefulness of the corona procedure for applications in which the thermal budget is critical.

Fig.3.4 shows profiles of oxide thickness, Q_f and D_{it}, for typical corona-treated oxides (case (b) of previous section) . The Q_f and D_{it} curves have been averaged from results for four identically-processed corona-treated films. Fig.3.4 (a) shows that the corona treatment has grown about 20Å thicker film in the center of the sample. The outer, corona-unaffected region serves as a control.

Fig.3.4(b) shows that Q_f in the central corona-treated region is measurably lower than in the outer control region. The boundary of the corona-treated region has substantially higher Q_f than either the central or control regions. These peaks occur on every corona-treated sample examined, and occur where the thickness of the oxide is within about 5Å of the control thickness. The highest Q_f appears to be outside the region where the thickness is increased over the control. This is relatively consistent with previous findings on thick [26,29] oxides.

Fig.3.4(c) shows that D_{it} in the central corona-treated region is slightly higher than in the outer control region. This is again consistent with the previous results [26,29] on thicker oxides corona-treated at 800° C (as opposed to those at 600-700° C, where D_{it} was somewhat *lower* than the control [26,29]).

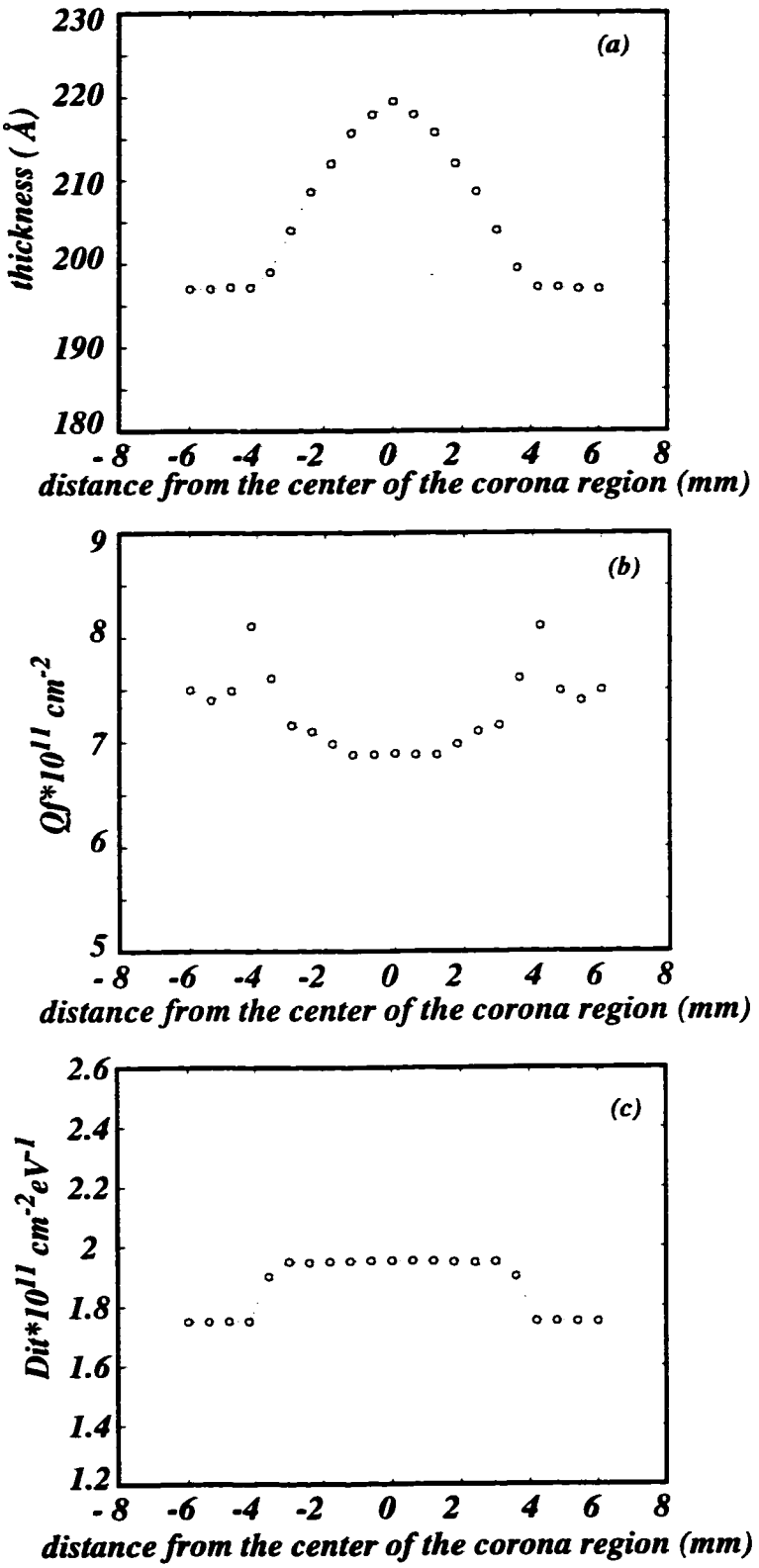

Fig. 3.4: The profile of a): thickness, b): Q_f, and c): D_{it} for a corona-treated film, originally grown by conventional dry thermal oxidation at 800°C for about 5 hours and then processed in corona apparatus at 800°C for 2 minutes. (needle current = -2μA).

3.5 Preliminary Oxide Reliability tests

To evaluate the reliability of the corona-oxide, a constant-voltage Fowler-Nordheim electrical stress of +8MV/cm was applied to the gates of each of control and corona samples. During this test, the gate current was monitored to calculate the build up of oxide charges [40] and, at certain intervals during the stress, C-V measurement was used to measure ΔD_{it} and ΔQ_f [1,40,41]

The first point observed during Fowler-Nordheim stress was the relatively low level of injection current for the corona oxides compared to the control oxides. Fig.3.5 shows typical injected charge levels after some specific times, for four different samples. Data for two different thicknesses, about 210Å and 160 Å, are shown in the figure. At both thicknesses, the corona oxide is more resistant to charge injection. This suggests that a

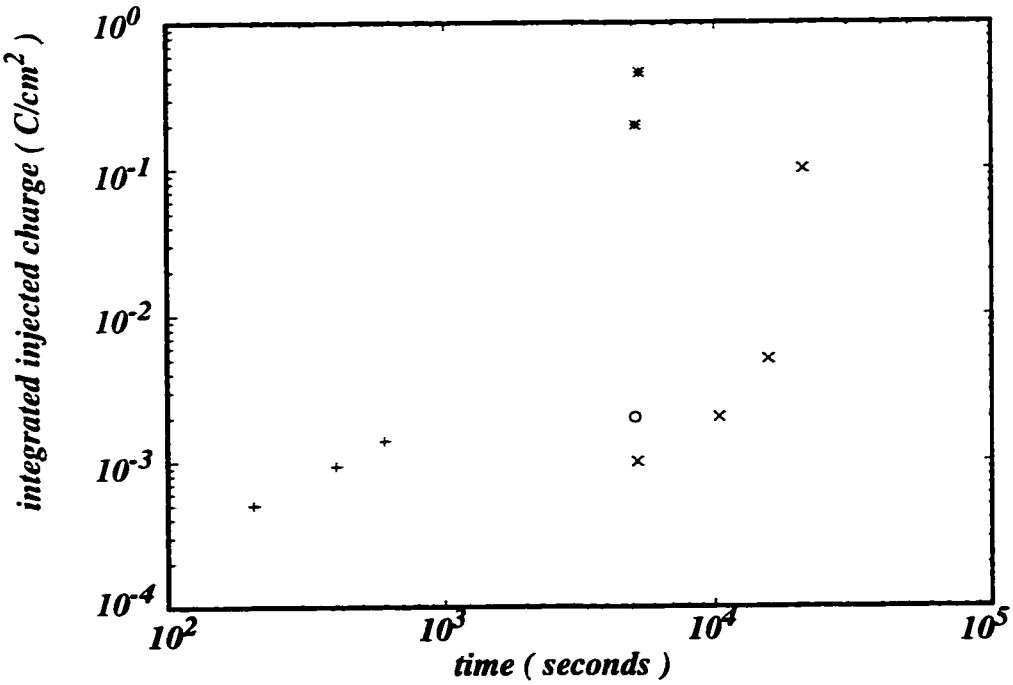

Fig. 3.5: Comparison of injected charges for four different samples;

o corona oxidation; 800°C; 155Å
+ dry oxidation; 800°C; 164Å
*** %50 O_2 dry oxidation; 900°C; 210Å**
x corona oxidation; 800°C; 218Å

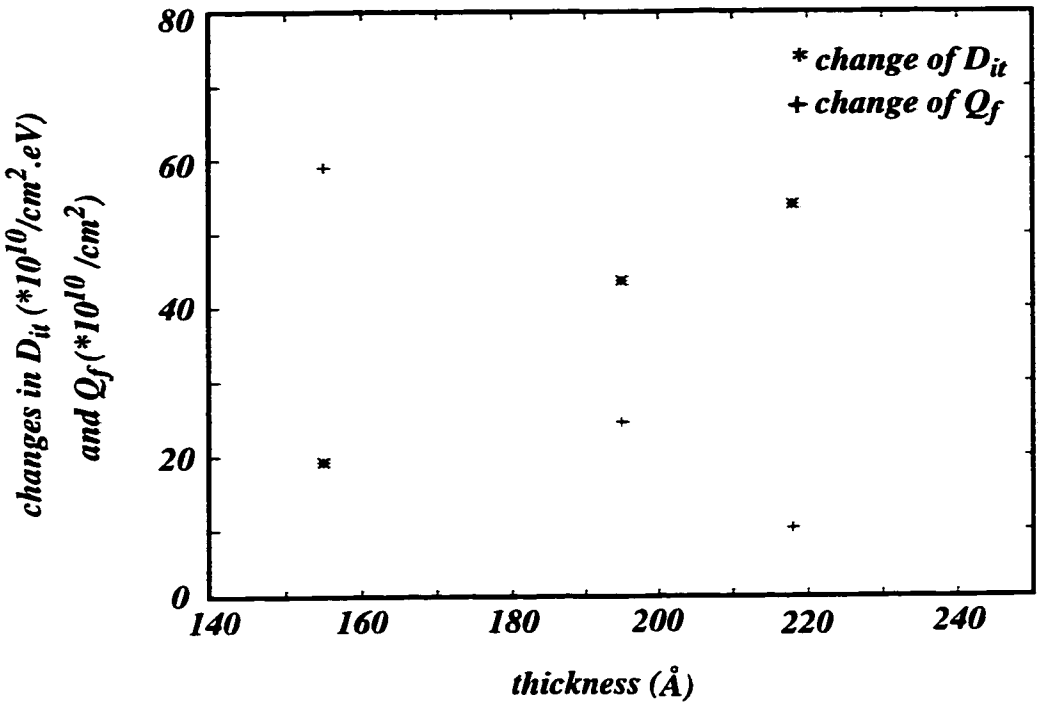

Fig. 3.6: ΔQ_f and ΔD_{it} for different regions of a corona oxide after 5200 seconds stress of +8MV/cm.

higher time-to-breakdown is likely for the corona oxidized samples

The change of Q_f and D_{it} were the next two parameters that were examined. Q_f and D_{it} were measured before and after a constant stress time. From this, ΔQ_f and ΔD_{it} were calculated. Fig.3.6 shows ΔQ_f and ΔD_{it} at various locations on a single corona-treated sample. The data points at ~220Å are at the center of the corona-treated region, while the data points at ~150Å are near the edge of the corona-treated region. Clearly the ΔQ_f at the corona peak was lower than at the edges. This is despite the fact that the creation of oxide charges is expected to be higher in thicker oxides, stressed at the same 8MV/cm (this is expected because the application of a higher absolute voltage tends to generate more tunneling electrons having higher energy [40].) ΔD_{it}, on the other hand, behaves more consistently with the expectation of more defects created in a thicker oxide (assumed to have the same "quality").

Considering the mechanism by which oxide trapped charges and interface charges are created [40], the ΔQ_f results in Fig.3.6 show that the bulk oxide in the center region of the sample may have better quality. In fact during the movement of hot electrons in the conduction band (see Appendix B) of the oxide and movement of holes in the valence band (during the electrical stress) the bulk oxide of the relaxed region shows good resistance against creation of new oxide charge.

For a stress of +8MV/cm, the maximum ΔQ_f was in the range of $8*10^{11}$ /cm^2 (for up to 17000 seconds). Fig.3.7 shows typical evolution of Q_f and D_{it}. As the figure shows, ΔQ_f and ΔD_{it} do not always increase during the stress. The decreasing of ΔQ_f shows either generation of negative charges or annealing of already-generated positive charges. Positive values of ΔQ_f show that the net trapped charge in the oxide is always positive.

To understand the mechanism of trap creation during applied stress, the charge build-up in the bulk oxide is measured using I-t measurements. A typical result is shown in Fig.3.8. The figure shows that, at the beginning of the stress, positive charges are created in the bulk oxide, followed by creation of negative charges. However, ΔQ_f obtained by C-V measurement indicates overall positive charges in the oxide. The difference is likely due to the creation of positive charges within a tunneling distance of the Si/SiO_2 interface, and also due to the creation of donor states at the interface (states having energy above the Fermi level at the flat-band condition) and/or healing of acceptor states (states having energy below the Fermi level at the flat-band condition.)

Fig.3.9 shows that, at lower oxidation temperature, the creation of negative trapped charges occurs at a lower amount of injected charges. Also, at the beginning stages of the stress, positive trapped charge density has the lowest value in the 800°C corona-grown

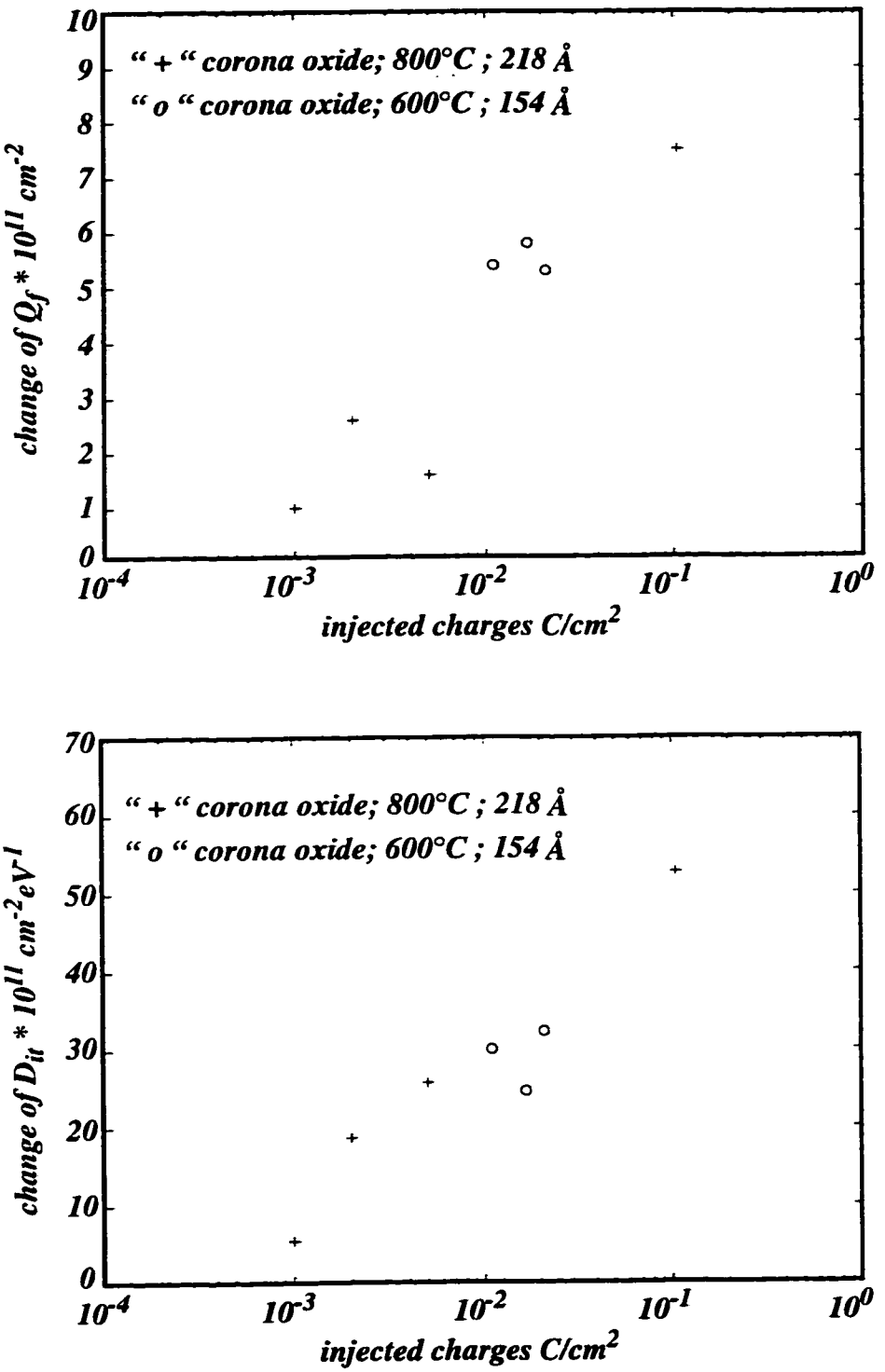

Fig. 3.7: A typical change of Q_f and D_{it} caused by constant voltage stress of +8MV/cm on corona oxide films.

(a)

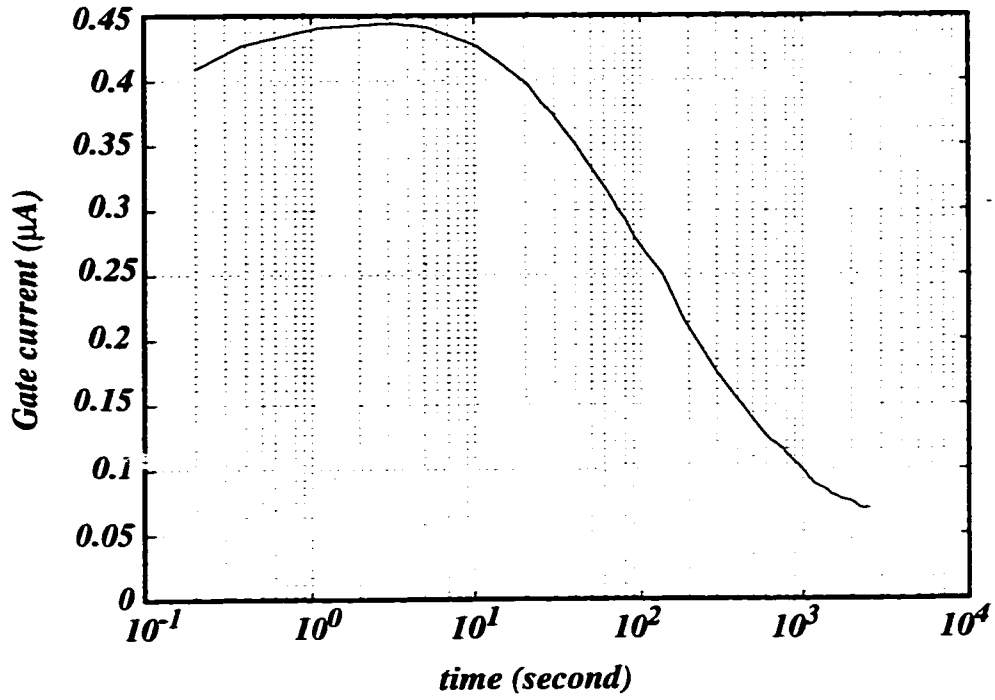

(b)

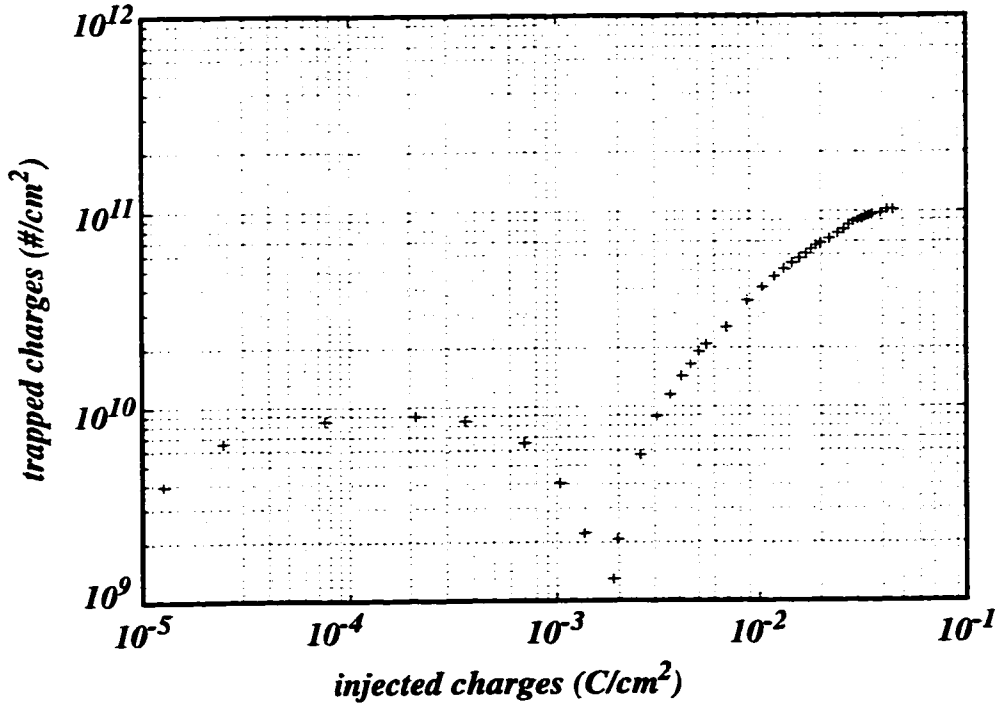

Fig. 3.8: (a): Oxide current during constant applied gate voltage. (b): Magnitude of the number of trapped charges as a function of injected-electron fluence. The film is a corona film grown at 800°C . The thickness of the film is 165Å, and the applied electrical stress is 8.7 MV/cm.

oxide and highest value in the 700°C corona-grown oxide. The lower values of positive trapped charge density in the 600°C compared to 700°C oxide could be caused by the high rate of creation of negative trapped charges in the 600°C oxide. The overall comparison of the results would tend to indicate that the oxide grown at 800°C has the highest quality.

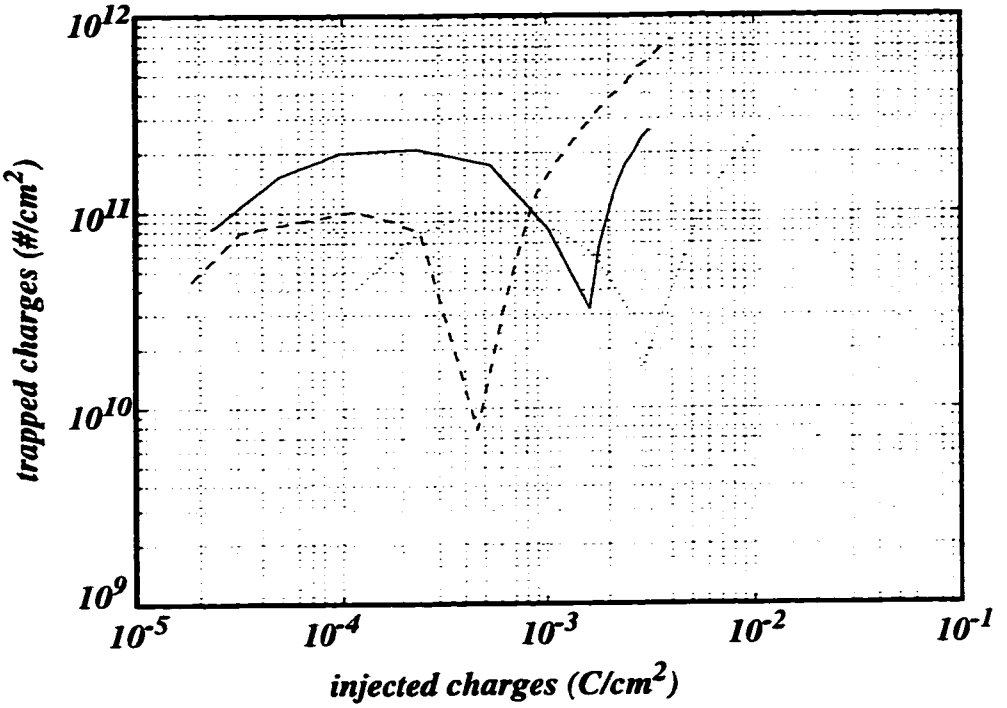

Fig. 3.9: Magnitude of the number of trapped charges as a function of injected-electron for three different corona-growth temperatures:

..... corona @ 800 °C x_{ox} =176 Å, E-field=9MV/cm
_____ corona @ 700 °C x_{ox} =183 Å, E- field=8MV/cm
_ _ _ corona @ 600 °C x_{ox}=179 Å, E-field=8MV/cm

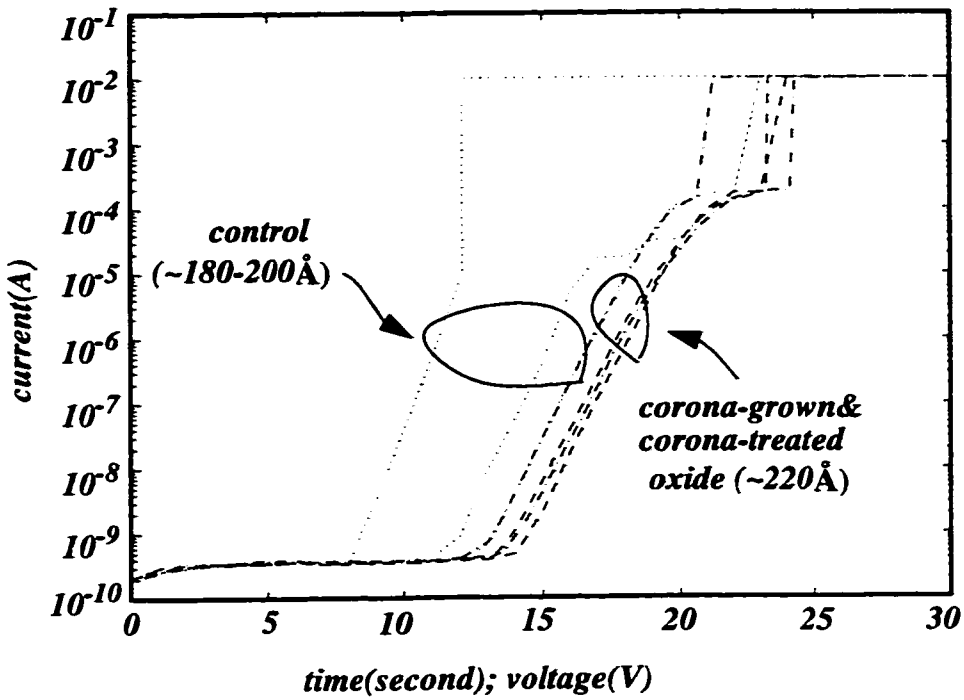

Fig. 3.10: ***Typical ramp I-V curves for different kinds of oxide films. The area of the MOS capacitors is $9*10^{-4}cm^{-2}$.***

3.6 Ramp Voltage Measurements

Fig.3.10 shows typical ramp I-V results. Since electron trapping does not significantly modify oxide electric field during this short test, the measurements are an indicator of the satisfactory robustness of the as-processed oxide structure. For all of the different cases of corona-processed oxide films in this work, the results are similar and appear to vary only with film thickness. Higher thicknesses yield higher V_{bd} (breakdown voltage), in the ~200-220Å thickness range. The particular behavior of the boundary region of corona-treated oxide film which was seen in the Q_f results, and which will also be seen in the TDDB results in section 3.7 and Fig.3.14 below, was not seen in this ramp voltage test.

3.7 I-t test and Breakdown Measurements

Fig.3.11 shows examples of voltage and electric field changes during constant current

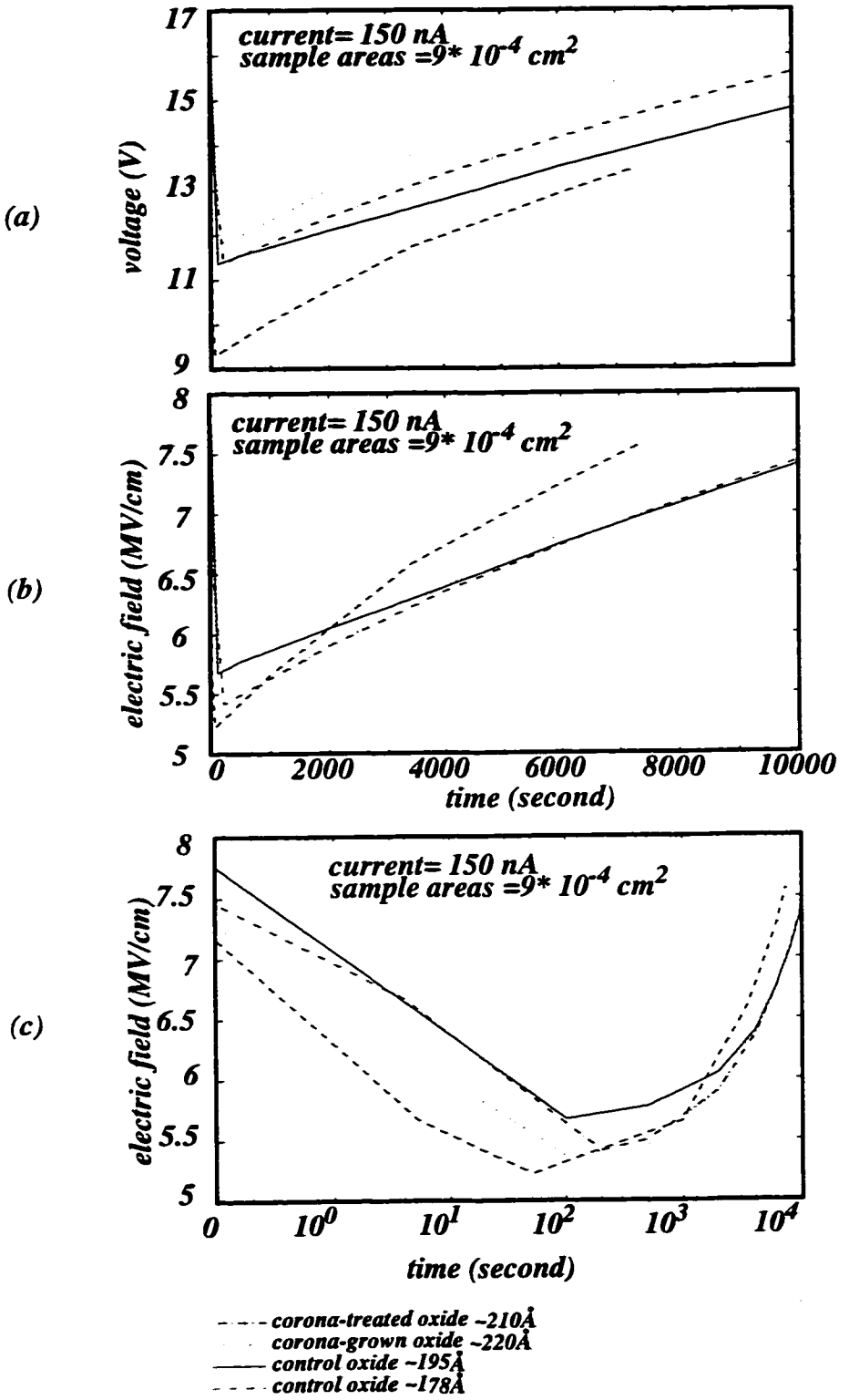

Fig. 3.11: Typical gate voltage(a) and electric field (b) changes during constant current test on different types of samples. Figure(c) shows (b) on a logarithmic scale.

test on the control oxide, corona-grown oxide and corona-treated oxide films. As the curves show, there are two main regimes: first positive charge trapping, then negative charge trapping. This behavior, which also has been seen in constant voltage stress results in Figs. 3.8 and 3.9 is typical of most oxide films during electrical stress tests, reported and analyzed in previous research [40,41,44,45].

Fig.3.12 shows another example of the gate voltage change during a constant-current test. Each discontinuity in the curve (except the last one related to a breakdown event) is related to the ~3-second interruptions in the applied current during the automatic changes in gate voltage sampling rate. From the different levels, and from the voltages which exist before and after each test interruption, it may be concluded that the wear-out process does not just consist simply of catastrophic and final failure. Rather, there are transition events, in which unstable charged defect structures are created; these structures are different

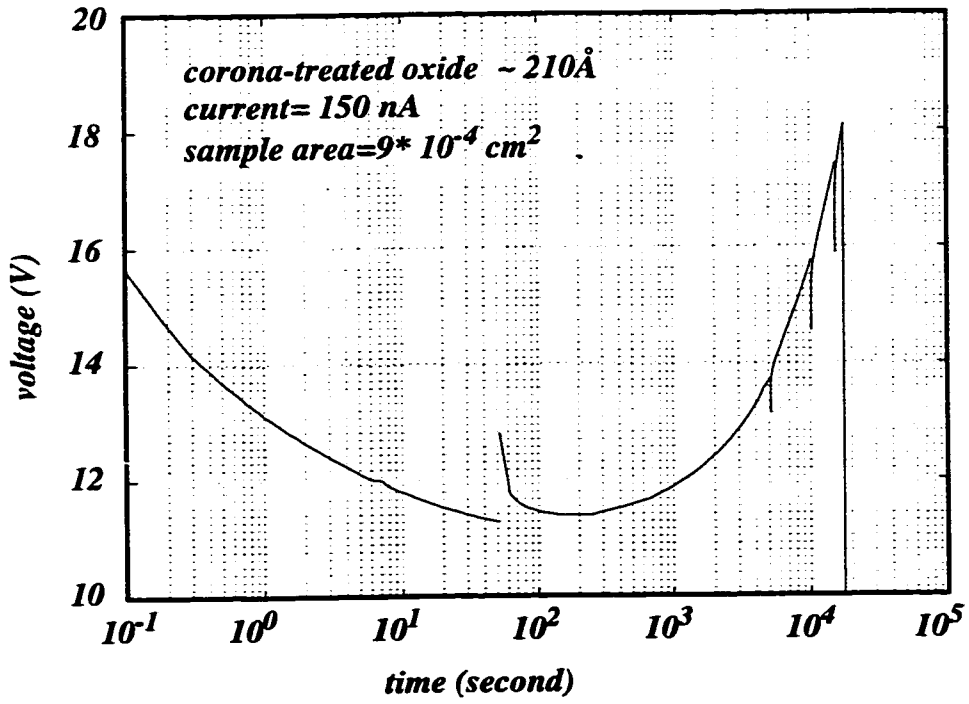

Fig. 3.12: A gate voltage changes up to the time of breakdown. The discontinuities in the curve are caused by interruption of applied current during the test.

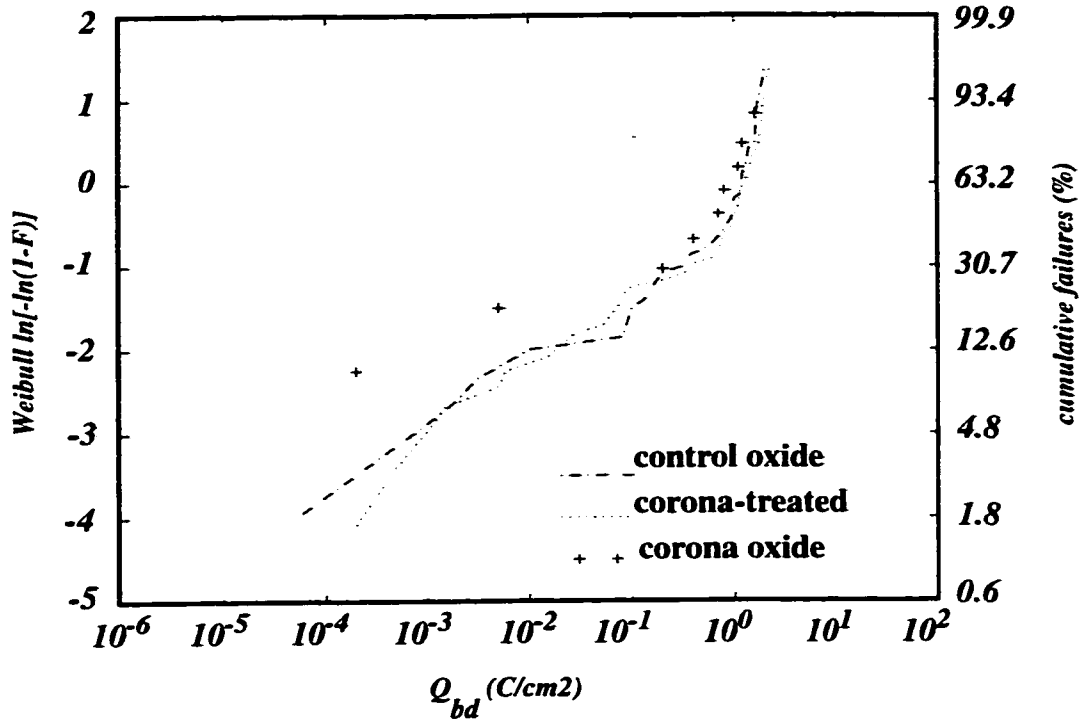

Fig. 3.13: Cumulative failures vs. injected charge-to-breakdown (Q_{bd}) for different types of oxide films.

from final structures. By removing the electrical stress, there is the possibility of re-neutralizing these unstable defect sites.

Fig.3.13 shows the statistics of charge-to-breakdown (Q_{bd}) for the control (about 200Å thickness) , corona-treated (about 200-220Å thickness), and corona (about 220Å thickness) oxide films. The continuous curves are for tests on populations of up to 60 MOS capacitors in each of the first two cases mentioned in Section 3.2. The individual data points represent the results of tests on 10 capacitors created in corona-grown oxide. Clearly the Q_{bd} statistics are quite similar for these three cases of oxide films. Even though the maximum Q_{bd} values of 1 to 2 C/cm^2 are substantially less than the Q_{bd} values usually reported for conventional thermally grown oxide film, the dependence of Q_{bd} on parameters like oxide thickness, applied electric field, applied current, the condition of the test (such as exposing the gate-oxide interface region to a light), the gate area (which

determines whether it is intrinsic or extrinsic breakdown) and the gate material, should be considered [42,45-54]. For example it is suggested that the values of Q_{bd} for MOS structures with Al gates are two orders of magnitude less than in similar MOS structures with polysilicon gates [54]. Some similar ranges of Q_{bd} for MOS structures with Al gates have been reported before [51-54].

To further understand the spatial variation of the corona effects, Q_{bd} tests were done at many points on the wafer surface, including control, corona, and boundary regions. A typical pattern of Q_{bd} is shown in Fig.3.14-(a). A clear tendency toward low Q_{bd} is observed at the boundary between the corona-treated and control regions. By averaging the values of Q_{bd} as a function of distance *from the center of the corona region*, Fig.3.14-(b) is generated. Clearly, the boundary region has worse breakdown characteristics than the corona region.

3.8 Overlapped Corona Treatments

To further examine the distinctive behavior of the boundary region of the corona-treated oxide, tests were done on films with overlapping corona-treatments, as described in Section 3.2, case (c), and Fig.3.2. As was mentioned there, after the first two minutes of corona treatment, the wafer was moved slightly so that the needle of the corona apparatus became located close to the boundary region and then at this new position a second two-minute corona treatment was done.

Typical profiles of Q_f and D_{it} of the MOS structures located along the xx' axis of Fig.3.2 , are shown in Fig.3.15. These results are averaged as a function of distance from the corona center over several identically-processed films. Similarly to Fig.3.4, the boundary regions (iii) have spikes in Q_f, but not in D_{it}.

Breakdown tests were also done on such overlapped corona-treated films. A constant current of $17*10^{-5}$ A/cm^2 for a maximum time of 50 seconds was applied to many MOS

(a)

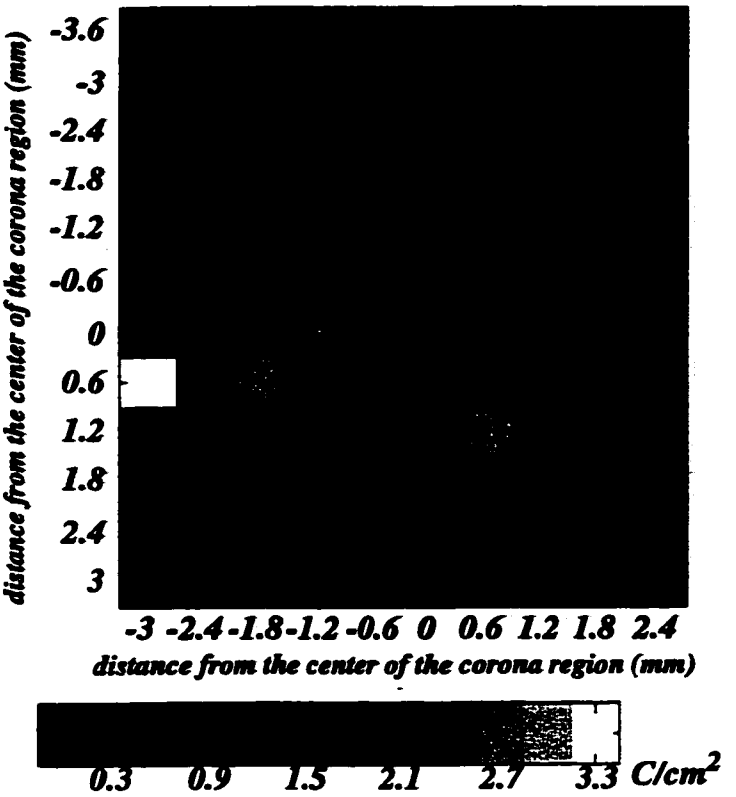

(b)

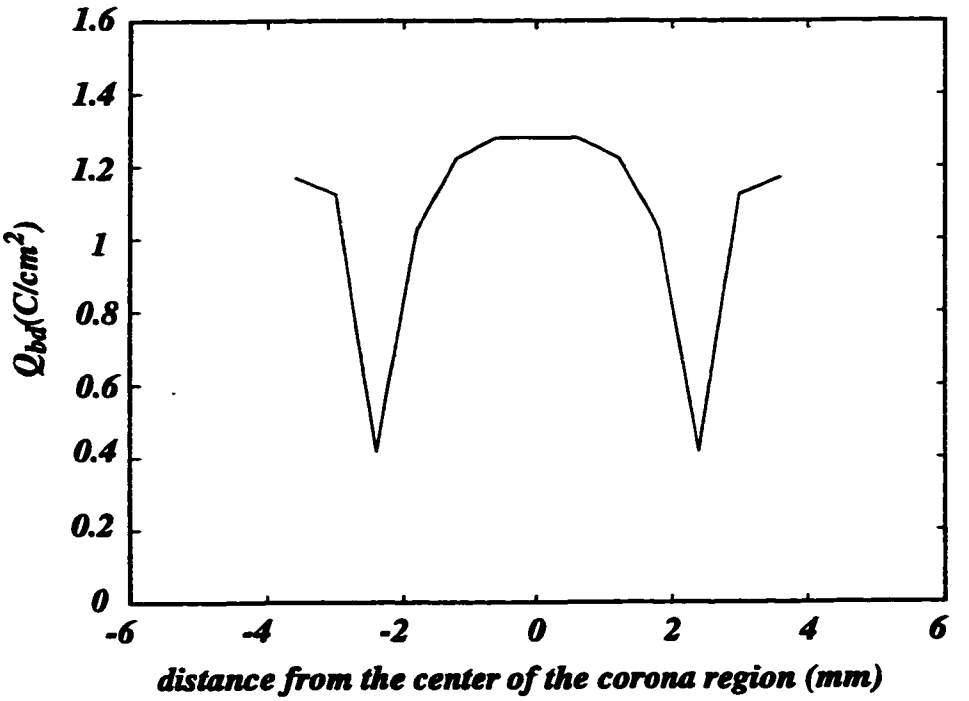

Fig. 3.14: (a): Image profile of Q_{bd} for different regions of a corona-treated sample. ($0<Q_{bd}<3C/cm^2$). (b): Average Q_{bd} calculated for different distances from the center of corona-treated regions obtained from the information in figure (a).

capacitors. Each position in Fig.3.15(d) represents tests on 12 different capacitors on several identically-treated wafers. The figure shows the fraction of capacitors (out of 12 capacitors) that survived the full 50 seconds without breakdown. The figure shows that the locations where the lowest number of capacitors survived 50 seconds corresponded to the boundary regions (iii).

Clearly the outer boundary region (iii) of the two overlapping corona regions has poorer electrical properties (Q_f), and is less resistant to dielectric breakdown than any other region. More importantly, the inner boundary regions (iv) and (v) are not substantially degraded compared to the main corona and control regions. If we assume that the inner boundary (iv) had weak properties at the end of the first corona treatment, it has *recovered* for satisfactory Q_f, and breakdown strength after being treated by the second (overlapping) corona step. The other inner boundary (v), which would also normally have had high Q_f, and low breakdown strength, also showed satisfactory performance in this overlapped configuration.

The behavior of the oxide at boundary regions (iv) and (v) reveals some essential facts. Even though these two regions (see Fig.3.2) may seem similar, they have undergone a different oxidation process sequence. Region (iv) would have had a low Q_{bd} after the first corona treatment, but now, having a full corona treatment (via the second corona process), its behavior is not like the boundary region (iii). This suggests that a kind of annealing process has happened in this region during the second corona process.

On the other hand, region (i) of the first corona treatment is the location that at the end of first treatment had been in the center area of the corona region, and its Q_{bd} values had been relatively high and its Q_f values had been relatively low. By doing the second corona process, part of this region has become boundary region (v) ; the boundary region of the corona-treated area on the already corona-treated oxide film. As can be seen in

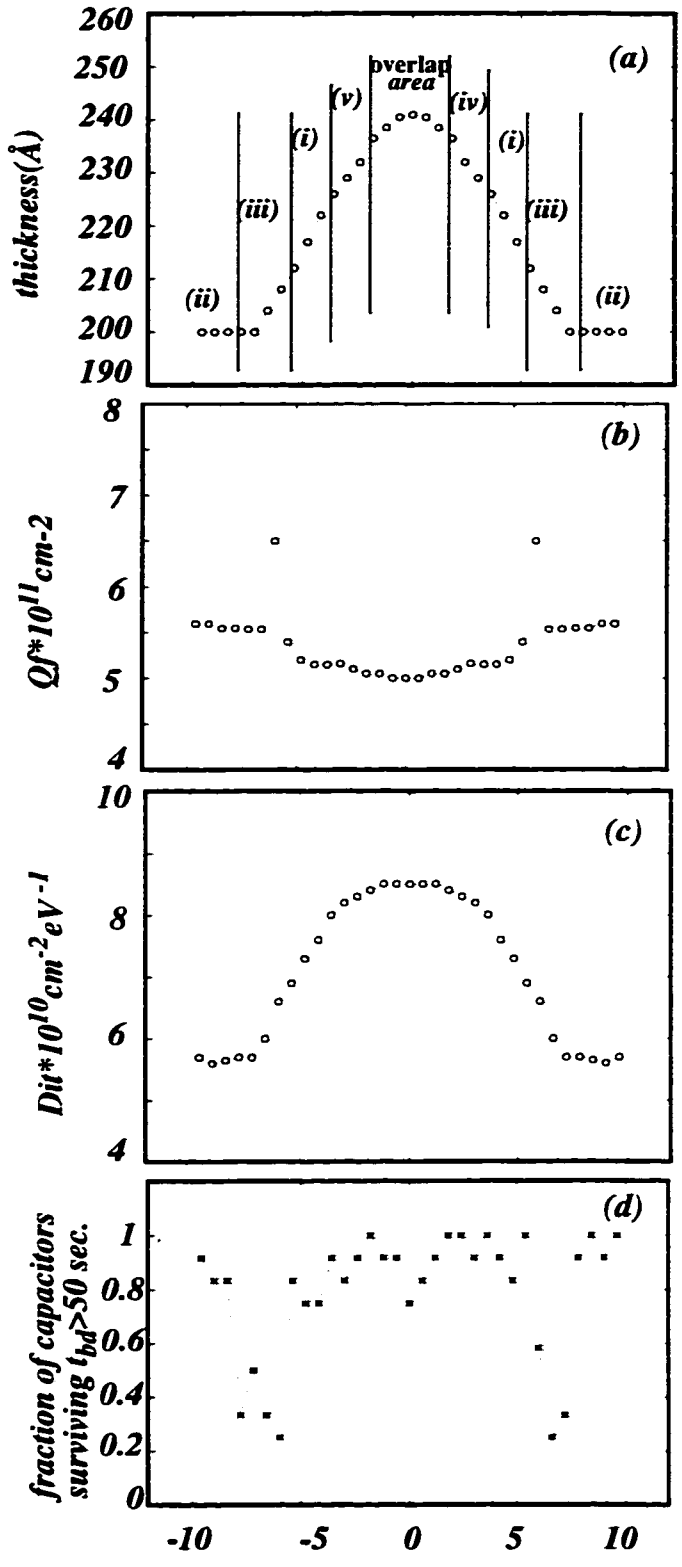

Fig. 3.15: Profiles of (a) Thickness, (b) $Q_{f,}$ (c) D_{it} and (d) breakdown behaviour, for a film having overlapped corona treatments, as described in case(c) in section 3.2.

Fig.3.15, the behavior of this region differs from that of regions (iii). This means that the corona-treated oxide film behaves differently from thermal dry oxide in terms of the quality of the boundary regions.

3.9 Discussion of Corona-Region Boundary Features

A particularly difficult feature of corona-processed films is that the boundary regions of the corona-treated areas have abnormally-poor electrical properties, as measured by Q_f and Q_{bd}. Since the creation of a uniform film over an entire wafer surface would likely require the overlapping of several corona-treated regions, this feature needs to be better understood before the process could be brought closer to practical use.

The results of the above-described electrical tests are summarized qualitatively in Table.3.2, regarding the features at the boundaries of the corona-processed regions. The results of Q_f and Q_{bd} measurements exhibit degradation at the outer boundaries of the corona region (where the corona region meets untreated thermal oxide), but not at inner boundaries within the corona region. This pattern of phenomena may be due to a structural

TABLE 3.2: Summary of features at the boundaries of corona-processed regions.

	Single Corona Treatment	Overlapped Corona	
	Boundary Region (iii)	Outer Boundary (iii)	Inner Boundary (iv, v)
Q_f	higher	higher	no feature
Midgap D_{it}	no feature	no feature	no feature
Q_{bd}	lower	lower	no feature

mismatch between the corona processed regions and the thermal oxide.

Most of the test results are consistent with the negative-point (anodic) corona process causing a *different* structure from standard thermal oxides. In the corona-treatment cases, the corona process is capable of changing the structure of an already grown oxide. This would account for both the severely compromised boundary regions (iii), and the satisfactory quality of the overlapped boundary regions (iv) and (v). It is likely that the degraded electrical characteristics occur simply due to a transition (perhaps a mismatch at an interface) between the two different SiO_2 network structures.

3.10 Chapter 3 Contributions

- The trends found by previous researchers in negative-point corona processing of thicker oxides were confirmed for thinner oxides:
  - Q_f was found to be in the level of ~mid-$10^{11}/cm^2$. This is close to that previously found for thick corona films, and to that of thermally grown films.
  - D_{it} was found to be in the level of ~mid-$10^{10}/cm^2eV$. This is also comparable to those of thick corona films, and standard thermally grown films.
  - the presence of edge phenomena seen previously in the Q_f results of thicker corona films, was also seen in thin corona films.
- Preliminary oxide reliability tests show that the negative-corona oxide is more resistant to creation of oxide defects. Also, ΔQ_f data indicates that bulk oxide in the center region of the corona film may have better quality compared to that in its surrounding regions. The trends of charge creation during electrical stress are comparable to those of standard thermally grown films.
- Ramp voltage tests showed that the V_{bd} are slightly higher for corona treated oxides compared to thermally-grown films.
- Edge phenomena were found in Q_{bd} results. There were low values of Q_{bd} at the boundary regions of the corona oxides.
- Overlapped corona treatments showed that if a boundary region of a corona film is located in the area of a second subsequent corona process, its properties recovered for satisfactory Q_f and breakdown strength. Also if a boundary region of a corona film is located in the area of a previously grown corona film, its Q_f and breakdown strength are not degraded.
- Most of the results are consistent with a structural difference between thermally grown and negative-corona grown films.

CHAPTER 4

Exploratory Experiments Toward Uniform Negative-Corona-Grown Films

4.1 Introduction

The promising electrical results of negative corona oxide films indicate that the films may have some potential to be used in microelectronic circuit structures. However, the corona films grown using a single needle electrode have nonuniform thickness profiles. Also such a single-needle structure affects only a relatively small area of the wafer.

To extend the method to create uniform films there are some possibilities. One is to repeat the process at adjacent locations on the sample by changing the relative positions of the sample and the needle. Another possibility would be to design a grid-of-needles structure for the negative electrode instead of a single needle, so as to obtain a more uniform and wider thickness profile . Using a combination of the two methods is also a possibility.

Although the first method, repetition of the corona procedure on different locations, may solve the problem of film uniformity, the overall time needed to complete the procedure would likely be prohibitively high, depending on the number of repetitions required. Furthermore, the necessity for precise movement of the wafer or the needle would require a relatively more complex apparatus and movement system. Perhaps a stepping motor could be used so that the needle, or the wafer holder, could be located precisely at many different pre-designated locations. Obviously, a proper cathode structure, (if available instead of the single needle) would be a more practical option.

This chapter presents experimental work to this end : to attempt to implement a multi-

point electrode structure to extend the corona method, to produce uniform oxide films on broader areas of the subjected wafers. The process of fabricating a grid-of-points structure on silicon wafers, and some experimental results of thickness profiles of grown corona films, are presented. As it is shown in the results, there are many difficulties and restrictions in using the technique to grow uniform film on a larger area of a wafer. However, the features observed in these experiments would be important considerations for any further work on the method.

4.2 Using a Grid-of-Points Structure in the Corona Apparatus

Using a different cathode structure instead of the single needle in the corona apparatus will change the thickness profiles of the grown films. Ideally, by using a grid of points structure and having the adjacent needles of such a structure close enough to each other, the resulting corona discharge would be uniform, and thus the SiO_2 film thickness enhancement would be uniform. This could be conceptualized as the overlapping of many closely-spaced bell-shaped profiles, each caused by one of the points in the multi-point structure.

As it was mentioned in the brief description of the corona apparatus of Fig.2.4 in Chapter 2, the needle used in that apparatus is a platinum needle. In the technique described in this chapter, silicon was used for the points. This was due to the practicality of using an anisotropic etch process to micromachine a regular array in a silicon wafer. The process provides the possibility of fabricating a grid of a large number of very similar (nominally identical) points, distributed uniformly on the small area of a silicon wafer. Nevertheless, to test the effect of using silicon instead of platinum, some other needle structures were also tested for comparison.

4.2.1 Fabrication Process of the Silicon Grid of Points

The procedure used to fabricate the grid of points is as follows:

1-After applying a four-step cleaning procedure (Appendix B) on a square-shape N-type <100> wafer with the length of ~2.5 cm, it went through a wet oxidation procedure for 1.5 hours at 1100°C. This caused growing of a thick oxide film with thickness of about 0.9 μm (Fig.4.1-a).

2- Using the procedure explained in Appendix B, a layer of positive photoresist was put on each side of the wafer (Fig.4.1-b).

3- Using the mask shown in Fig.4.2-a, windows were made on the top photoresist layer using UV photolithography (Appendix B). At the end of this stage there where many isolated square-shaped photoresist regions on the center region of the wafer on its front side (Fig.4.1-c).

4- In the next step the wafer was put in Buffered Oxide Etchant (BOE) - 1:4 HF:NH_4F - for 2 minutes. The oxide film in the open regions was etched off (Fig.4.1-d).

5-The photoresist layers were removed by acetone (Fig.4.1-e).

6-By using a 15% TMAH solution at 90°C silicon was etched in the open areas. After 2 hours of etching, the structure shown in Fig.4.1-f was obtained. The wafer was then rinsed in D.I. water.

7-By using diluted HF and a Q-tip, the center area of the oxide film on the back side of the wafer was etched off (for better electrical connection during corona oxidation) (Fig.4.1-g).

8-The TMAH etching procedure continued for another 2 hours. During this time the etching of the silicon continued on the front side of the wafer and the open area on the back side was etched as well. The total 4 hours of etching was based on a ~35 μm/hour under-etch rate. This caused the final under-etch length at each edge of the squares to be

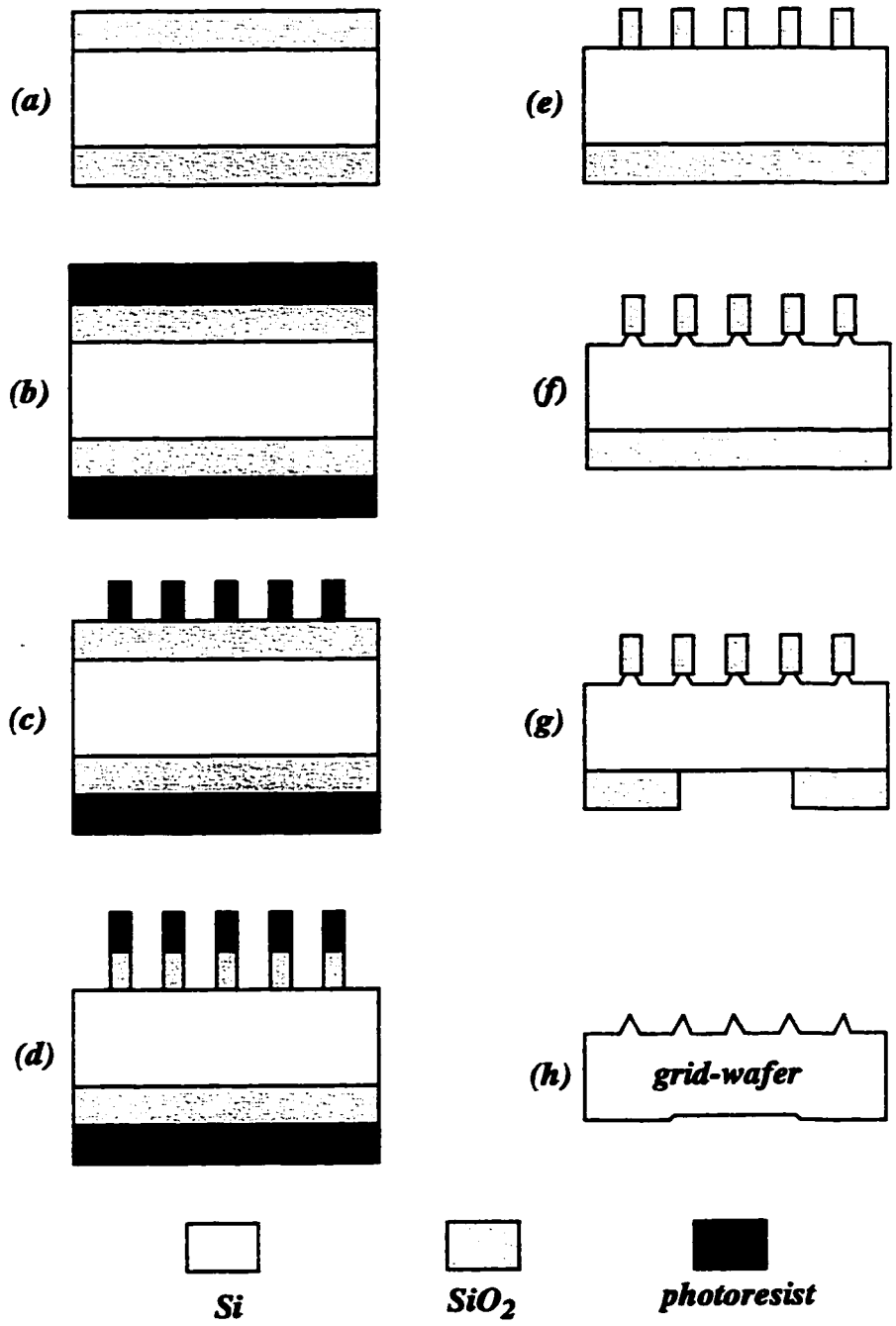

Fig. 4.1: The results at the end of different steps during fabricating a grid of points on a piece of silicon wafer. The details of the procedure are explained in the text.

(a)

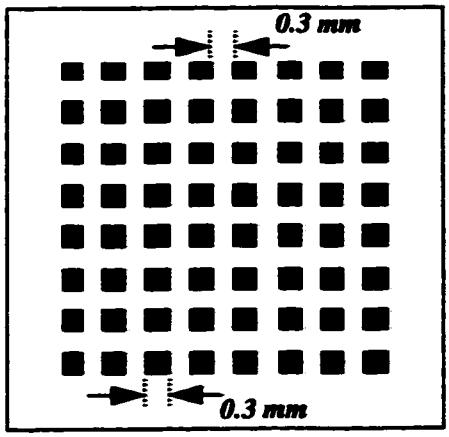

(b)

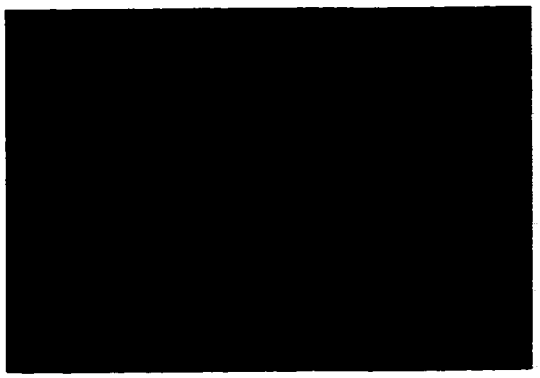

(c)

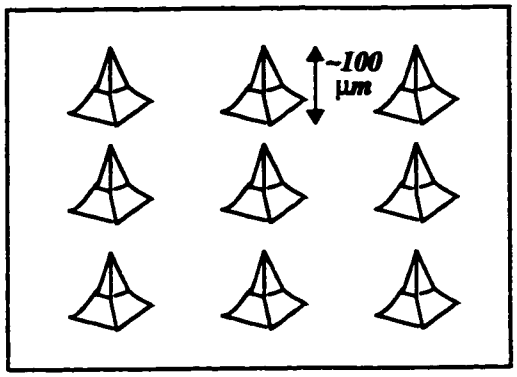

Fig. 4.2: (a): The mask used to fabricate a grid of points. (b): A top view of the micromachined points in the fabricated grid. (c): Plan view schematic of a few micromachined points.

close to half of the side of the squares. The resulting structure was a wafer with about 1000 needle like (hillock) structures on its front side (Fig.4.1-h). Fig.4.2-b, c show the real structure of the resulting points.

Before putting the wafer inside the oxidation tube, it was cleaned by a Reverse-RCA cleaning procedure (Appendix B) and then dried by nitrogen flow.

In the following sections the wafer of Fig.4.1-h is referred to as the "grid-wafer".

4.2.2 Grid Set-up Configurations and Corresponding Oxide Film Results

Fig.4.3 -a shows the first configuration used to hold the grid-wafer in the oxidation tube. An assembly made of quartz and platinum wires was used, both as a mechanical support, and to implement the electrical connections as shown. From this configuration, the resulting film growth enhancement was mostly directly beneath the edges of the grid-wafer, and also beneath the platinum wires which suspend the grid-wafer. Fig.4.3-b schematically shows much higher oxide growth at the locations below these platinum wires. It was concluded that the slightly shorter distance of the wires to the subject sample (see Fig.4.3-a), and also the tendency of electrons to repel from the farthest points of the grid-wafer, caused the result.

To resolve some of these problems the configuration shown in Fig.4.3-c was attempted. In this configuration, the locations of the grid-wafer and the subject wafer were exchanged. The grid-wafer was placed on a piece of platinum foil, and a much bigger wafer was used as a subject wafer. The subject wafer was placed face-down toward the grid of needles on four sapphire rods. To obtain a negative corona, a positive voltage was applied to the subject wafer through the high voltage wire, and the back side of the grid-wafer was connected to the ground wire.

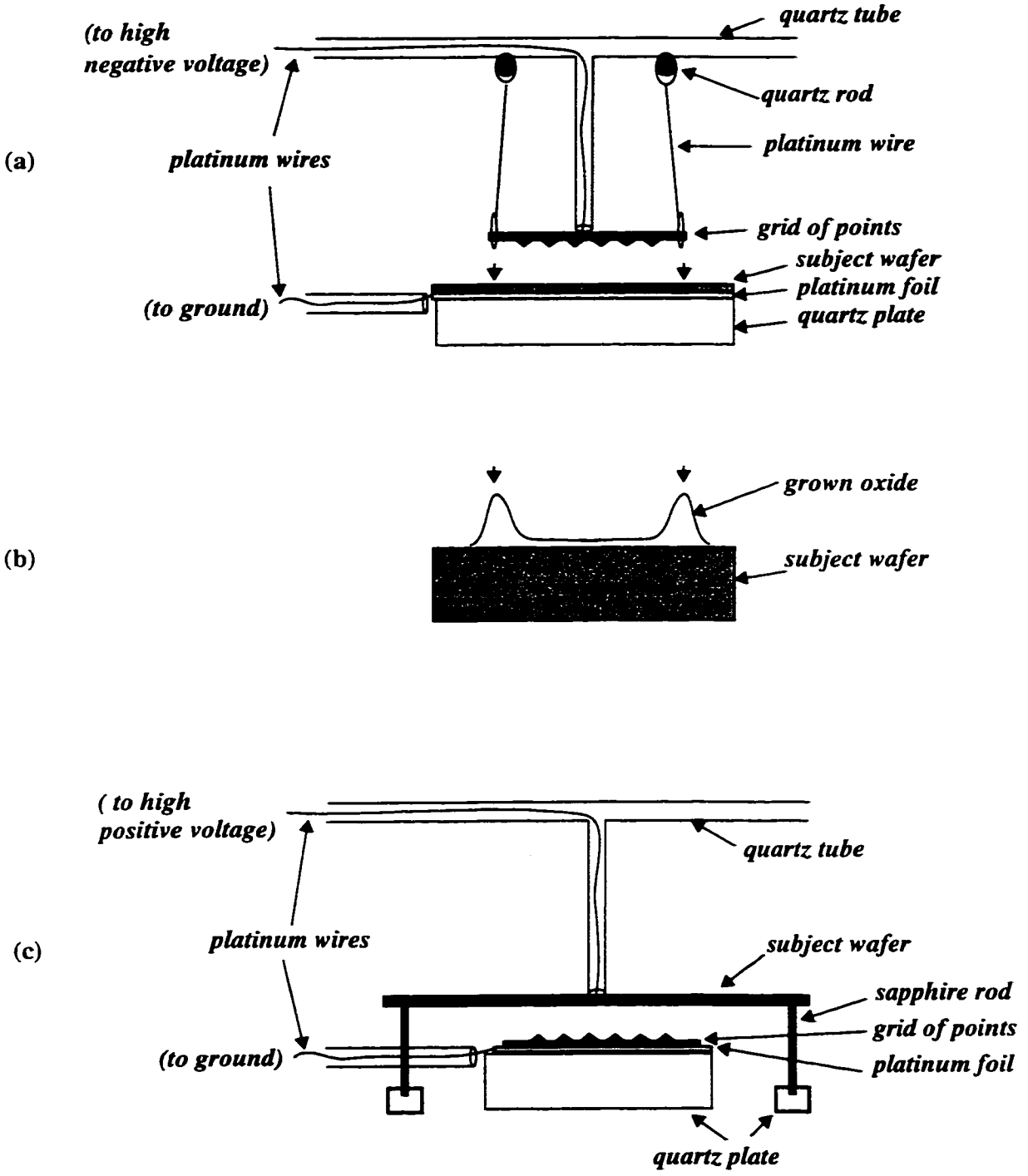

Fig. 4.3: a & c) Two different configurations used to set-up the grid of points into the corona oxidation tube. Two small arrows above the subject wafer in (a) show the places right below the holder platinum wires. b) Illustration of the extra oxide growth rates at the locations below the holder platinum wires in (a).

The leakage current from the four sapphire rods was measured by removing the grid wafer and platinum foil and applying a high voltage between the sample and the ground wire. At the applied voltage of 1.568 kV, the current was 0.1 μA, which was much lower than the 10 μA obtained for the same geometric condition, and same applied voltage, when the grid-wafer was in its place. It indicated that the current that passed through the sapphire rods was relatively low and negligible.

Tests using the configuration in Fig.4.3-c showed that there was still a high rate of oxidation at locations close above the edges of the grid wafer. Also, when applying relatively high corona current, there was an unstable discharge current between one or two corners of the grid wafer and the subject wafer. For this reason, the experiments were done mostly at relatively low corona currents with long oxidation times (1<current<10 μA, 1<time<30 hours).

Figs. 4.4 show two typical oxide thickness profiles for the configuration of Fig.4.3-c. The corona oxidation conditions are shown in the figures. As the thickness profiles show, even though there is an enhancement in the region over the grid of points, there is also high enhancement in some regions over the edges of the grid wafer. The different enhancements on the two different sides could be due to slightly different spacing from the grid wafer edges to the subject wafer. Other experiments similar to the one depicted in Fig.4.3-c confirmed that in fact the flow of the corona current is not only through the needle region of the cathode.

Previous research on the negative-point corona process [26] showed that the number of oxygen atoms incorporated into the SiO_2 structure due to the corona process, is close to the number of electronic charges that pass through the film during the process. It was suggested that each electron of the current, has the role of introducing one oxygen atom into the growing SiO_2 structure. To examine whether the same phenomenon applies when

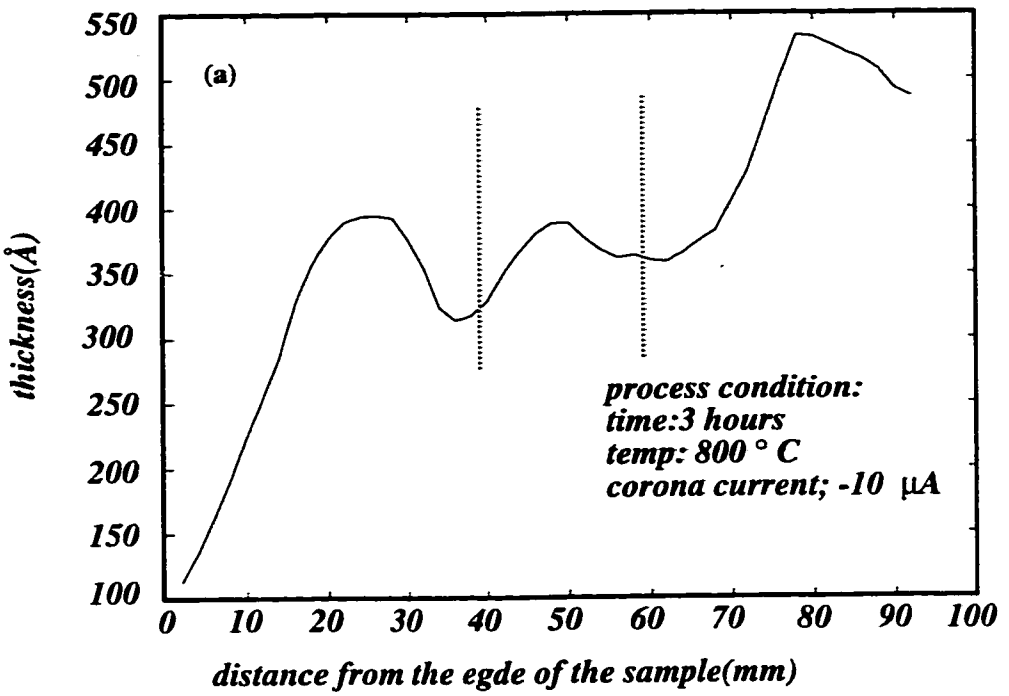

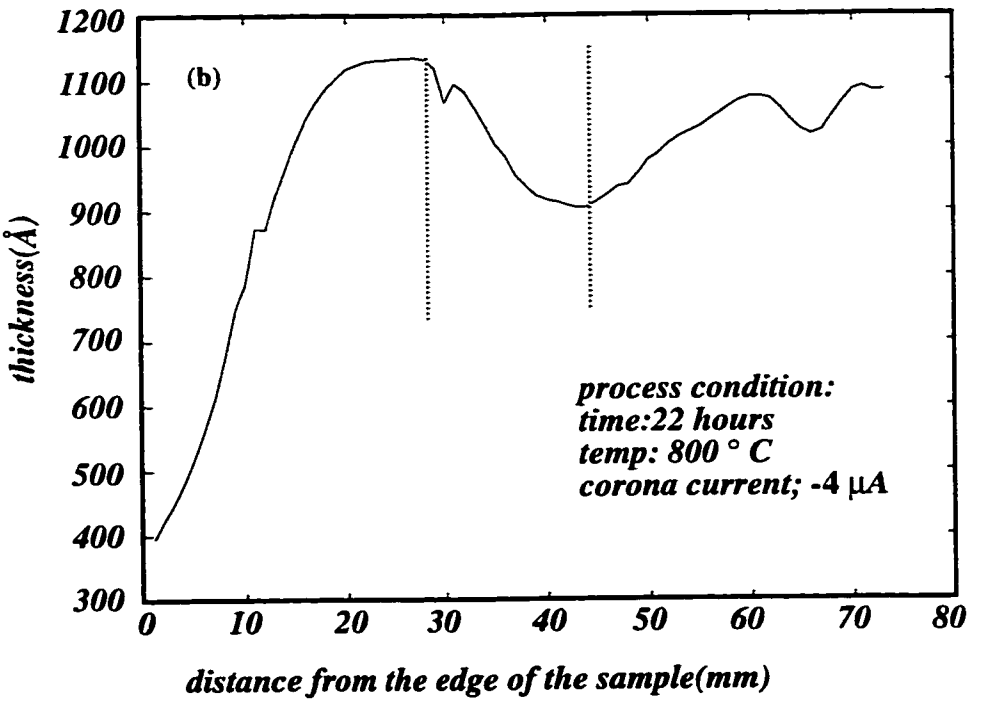

Fig. 4.4: Two typical thickness profile results of using the grid wafer. The region between two dashed lines shows the region beneath the grid of points.

using the grid wafer instead of the platinum needle, the approximate numbers of oxygen atoms incorporated into the SiO_2 structure were calculated. The calculations related to the two Figs.4.4 (a) and 4.4 (b) are included in Appendix A. The following are the results of calculations:

For sample of Fig.4.4(a) :

Estimated number of incorporated oxygen atoms due to the corona effect $\cong 6.62 * 10^{18}$

Estimated numbers of electrons passed through the wafer during the corona process $\cong 6.73 * 10^{17}$

For sample of Fig.4.4(b) :

Estimated number of incorporated oxygen atoms due to the corona effect $\cong 1.08 * 10^{19}$

Estimated numbers of electrons passed through the wafer during the corona process $\cong 1.98 * 10^{18}$

The numbers of oxygen atoms are greater than the numbers of electrons. Even though the calculated numbers of oxygen atoms are rough estimates of their real values (see Appendix A), they are far enough from the numbers of electrons to conclude that the real numbers of oxygen atoms are indeed greater than the numbers of electrons. This may indicate that, beside the possible direct effect of each electron in the growth of the oxide film (like creation of O^- by each electron that eventually could direct the O atom into the SiO_2 structure), there could be some other effects that also alter (enhance) the oxidation rate.

4.2.3 Growing Film Through Windows Opened in a Thick Oxide Layer

One practical way to reduce the effect of the edges in the above experiments is by using a patterned shield between the grid wafer and the sample. This shield would need to have open windows at certain locations directly opposite the points, in order to guide the corona current through the predesigned areas, not through the edges of the wafer. In this work, instead of using a separate shield, a previously-grown layer of thick oxide on the

substrate was used as the shield. The oxide film at the center area opposite the points was etched off before putting the sample into the corona oxidation tube. The corona process was done for 30 hours at 800°C with the corona current of 0.7 μA.

Fig.4.5 shows the result at the region opposite the points. The corona grown film is much more uniform than those in Fig.4.4. The refractive indices of the film are close to those of the high temperature oxide films, similar to those found by processing with a single needle (Chapter 3).

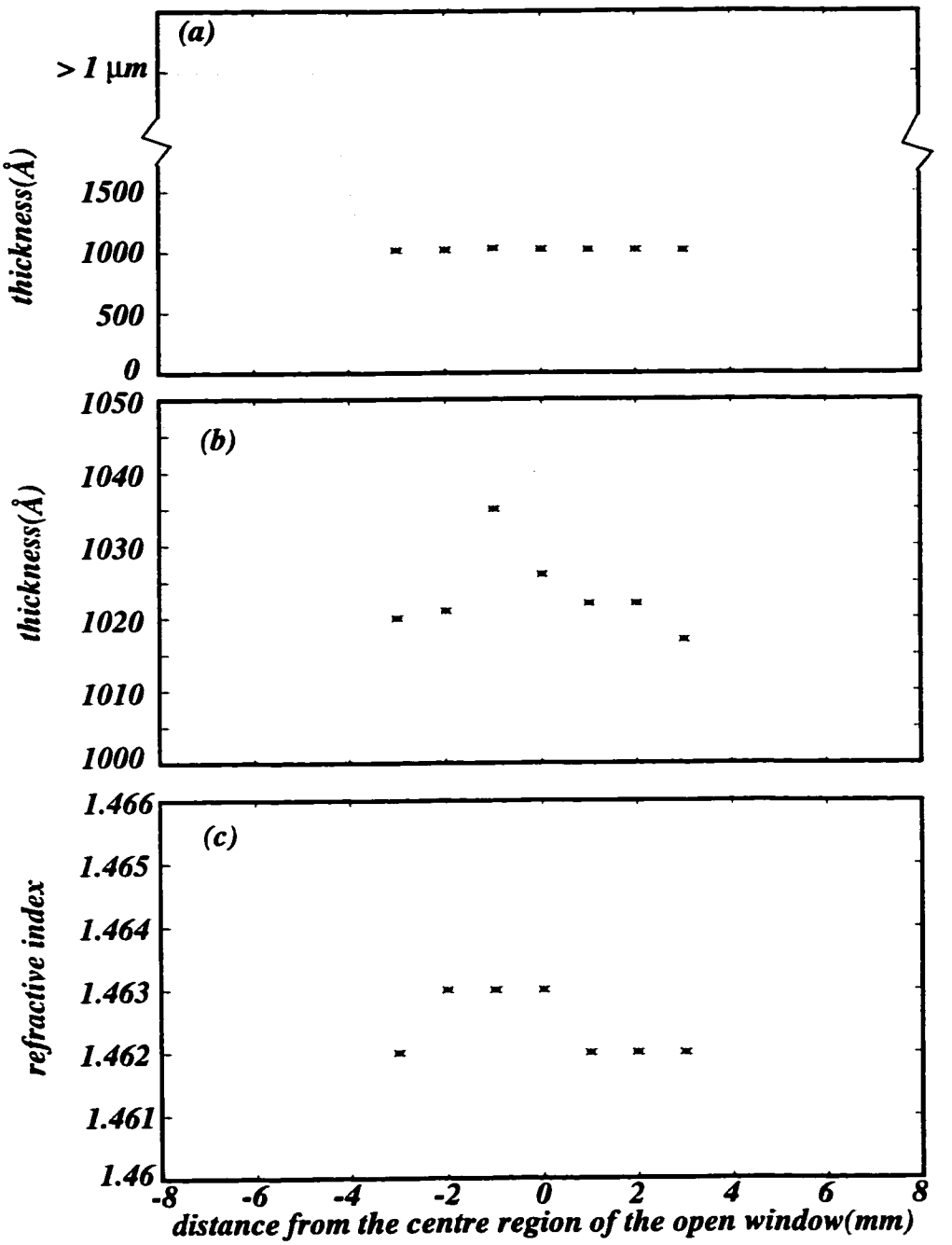

Fig. 4.5: The results of using the grid of points in the corona apparatus to grow film on bare silicon through the the area opened in the thick oxide film of a sample; a & b) thickness vs. position on the wafer; c) refractive index vs. position on the wafer.

4.3 Test of Some Other Cathode Structures

In order to supplement the overall experimental understanding of the method of using a grid of points, some other cathode structures were examined as well. Through this, the possible effects of simultaneous currents in adjacent needles on the individual currents and on the path of the current in a multi-needle structure were examined. Fig.4.6 (a,b,c) shows three different cathode structures that were tested.

Fig.4.6 (a) shows a three-needle structure made of platinum needles connected at one end. The oxide profile results of this configuration showed that the profile is the result of overlapping three bell-shaped profiles each caused by one of the needles. A top view of a typical thickness profile of the resulting films is shown in Fig.4.7(a). Despite efforts to place the needle tips at equal distances from the sample, the thickness profiles related to the three needles did not have equal peak values. This demonstrates the extreme sensitivity of the corona to the relative positions of the needles and the wafer.

Fig.4.6 (b) shows a cathode structure consisting of the holder and a Pt wire suspended parallel to the subjected wafer. For this configuration, even with the middle part of the wire slightly (~ 0.5 mm) sagging down toward the wafer, the greatest thickness of extra oxide was observed close to the two bent ends of the wire. This demonstrates that the current mostly passes through the corner areas of the cathode.

Fig.4.6(c) illustrates another electrode structure made of silicon. The fabrication procedure of the structure involves micromachining techniques similar to that previously described for the grid of points. In this structure, twelve(12), 0.5 mm-wide silicon needles are etched in a 0.5mm-thick silicon wafer. The two needles on the ends are arranged to be slightly shorter than the remaining ten. Fig.4.6(d) shows an optical micrograph of the structure.

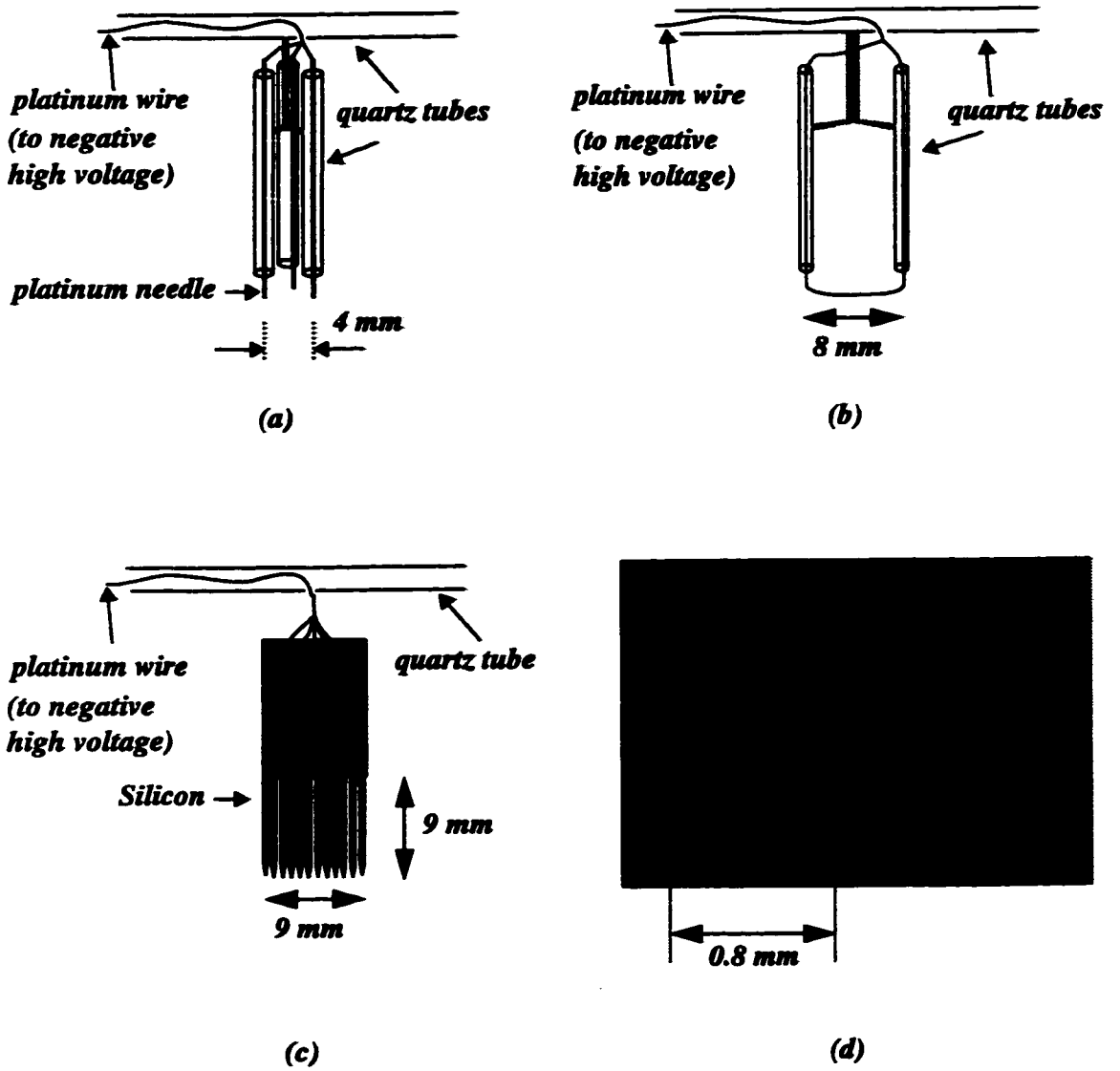

Fig. 4.6: a,b,c) Three different cathode structures used in corona apparatus; d) Photograph of the needle structure shown in (c).

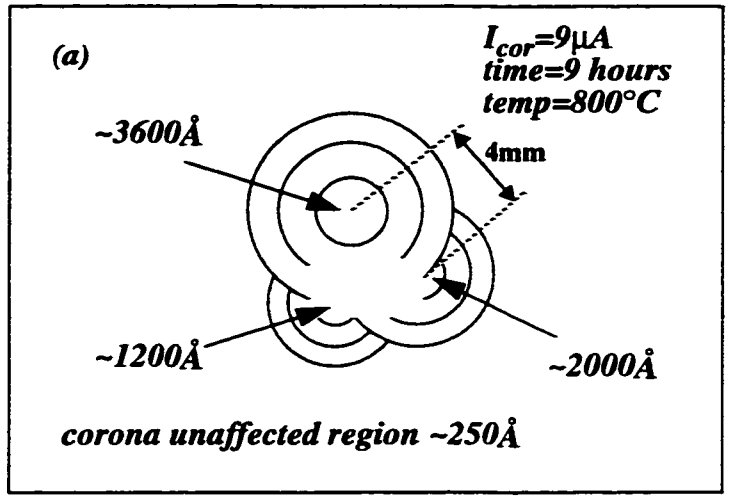

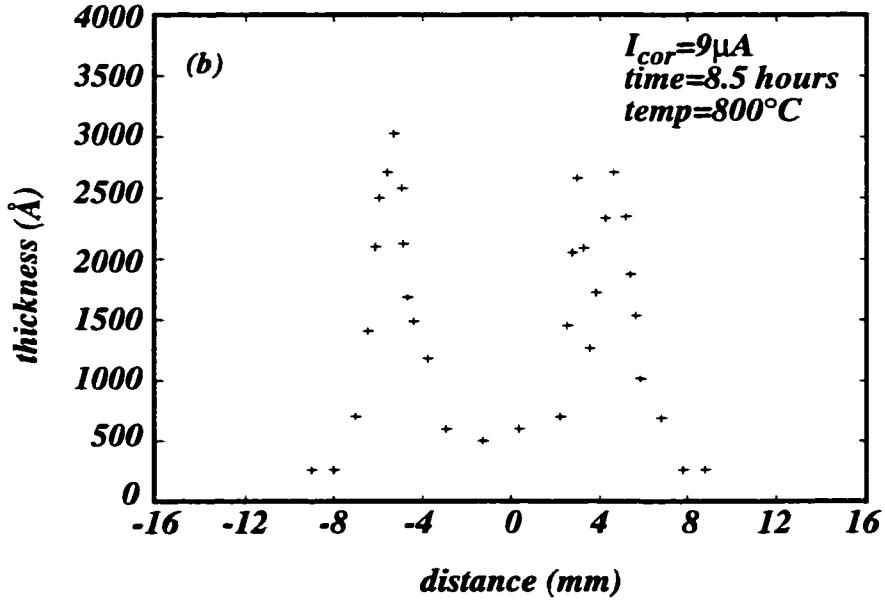

Fig. 4.7: a): Top view of a typical thickness profile of the film grown by use of the cathode structure shown in Fig.4.6 (a); each circular line indicates the places with a same thickness, and the three smallest circuits in the middle of the bigger circles, are the locations with relatively higher thicknesses. b): a typical thickness profile of the film grown by use of the cathode structure shown in Fig.4.6(c).

During the corona oxidation process, the current paths were longer from the two end-needles to the subject wafer. However, the result showed that the regions close to these two needles have higher thicknesses compared to the regions which were close to the needles in the middle. Fig.4.7(b) shows a typical result using this structure. As the figure shows, at the two end regions of the profile, the thickness is higher. It is a clear indication that electrons tend to travel from needles to the wafer along the most widely divergent paths available.

4.4 Conclusions

Efforts are presented to grow more-uniform negative-corona films on broader areas of the subjected wafers. To this end, the single-needle cathode structure is replaced by a multi-point structure. Even though the use of a multi-point structure causes overlapping of the growth-enhancement profiles from individual points, it is quite difficult to keep the corona current equal in the points (or needles).

The difficulties stem from two main issues:

(a) the great sensitivity of the corona discharge to the point-to-plane distance, which would thus require that any two points have exactly the same distance to the substrate;

(b) the tendency of the electric current carried in the corona discharge to seek the most divergent paths available, thus leading to the thickness profiles being enhanced around the edges of several cathode geometries.

These findings suggest (for future work), the use of different schemes and structures, so that the individual points can electrically separated, such that the currents can be individually controlled.

The results of corona oxidation using the grid of points with small areas opened in a thick oxide layer demonstrated that such a patterned "shield" can guide the corona current

to desired locations, and solve the problem of dominant currents at the edges of the grid wafer.

These experiments showed that there are substantial difficulties to be solved, if the technique is to be used to create uniform oxides without a patterned shielding oxide. However, study of the features observed in these experiments are important to be considered in any further work on the method.

4.5 Chapter 4 Contributions

- In the interests of growing more-uniform negative-corona SiO_2 films on broader areas of silicon wafers, experiments using multi-point or multi-needle cathode structures were conducted.
- Micromachined grid-of-points structures were fabricated and used as cathode for corona-discharge oxidations, in two different configurations.
- The oxidation rate enhancements were found to be non-uniform, leading to several other experiments to discover the nature of the causes for the non-uniformity. Two other cathode structures were examined: one made from 3 Pt needles, and another made by micromachining 12 long needles from a piece of silicon.
- Difficulties were found to be likely due to two main issues: (a) the great sensitivity of the corona discharge to the point-to-plane distance, which would thus require that any two points have exactly the same distance to the substrate; (b) the tendency of the electric current carried in the corona discharge to seek the most divergent paths available, thus leading to the thickness profiles being enhanced around the edges of several cathode geometries.
- It was found that the grid-of points method was more effective in oxidizing areas of bare Si opened through a previously-grown thick oxide layer. The thick oxide

pattern may act as a shield, guiding the corona discharge current to the desired areas.

- Regarding the relationship between the number of charge carriers passing though the film due to the corona current and the number of oxygen atoms incorporated into the film, it was found that using the grid-of-points, much fewer charge carriers (approx 10 times fewer) are required.

CHAPTER 5

Positive-Point-to Plane Experiments

5.1 Introduction

The polarity of the corona apparatus can be changed. By changing the negative voltage of the needle in the apparatus of Fig.2.4-a on page 16 to a positive voltage, a completely different condition for corona processing is created. We will refer to this process as a positive-point corona, or simply "positive-corona" process.

Thickness profiles of positive-corona films have been reported before by Modlin [22]. It has been shown that the process creates films with thickness profiles completely different from those of negative corona. This process affects a much wider region of the subjected wafer. In contrast to the negative-corona, which creates profiles with the peak thicknesses at the center directly under the needle, the positive corona creates films with peak thicknesses away from the center. Only in very thin films, does the center still have the highest thickness. In all cases of positive corona, the affected corona region is much wider than that of the negative corona.

The positive corona process produces not only a completely different oxide film profile, but also, based on the characterization results obtained in this work, produces films with quite different electrical and physical characteristics. In this chapter, the refractive index data and the C-V results of the films are presented, and compared with those of the negative corona films. The C-V results of the films, alone, reveal an essential difference between two types of films.

Different characteristics of films grown under two different voltage polarities are also reported in the study of films produced by positive- and negative-biased conventional

plasma-enhanced-chemical-vapor-deposition (PECVD) processes [18]. Note that in plasma oxidation, the terms "positive-biased" and " negative-biased" refer to the substrate voltage, "anodic" and " cathodic" respectively. In this work on corona oxidation, however, the "positive" and "negative" refer to the polarity of the corona needle voltage, thus "cathodic" and " anodic" respectively. Studies have shown that positive-biased (anodic) plasma films have electrical properties which would be acceptable for use in VLSI technology, while the negative-biased plasma films have much worse electrical properties. This is the main reason why most recent research effort has been in the study of anodic plasma oxidation.

Similarly the study of the negative corona (anodic) oxide films also shows that the films have acceptable electrical properties comparable to those of thermally grown oxide films. As will be presented in this chapter, preliminary results of the electrical properties of the positive corona films indicate that these films have poor electrical properties in accord with the findings of plasma-oxidation.

5.2 Thickness Profile and Refractive Index of the Positive Corona Films

The cleaning procedures and the detailed procedures of corona processing for growing positive corona oxide films, are similar to those of negative corona films given in Appendix B. The only difference is the different polarity of the applied voltage on the needle of the apparatus during the oxidation process. The magnitude of the needle voltage needed to hold the corona current at its specified pre-set value, was found to be lower in positive corona compared to that of a similar negative corona process with same amount of current. Typical values of needle voltage, and their variation during corona processing, for both positive and negative cases, are given in Appendix A. The temperature of the oxidation process for all the experiments reported in this chapter was 800°C.

Fig. 5.1 shows two typical profiles of positive corona grown films, along with two typical profiles of negative corona-grown films for comparison. As the figure shows, the affected corona region in the positive case is much wider than in the negative case and, as many other experiments have shown, for the same amount of time and current, the thicknesses of the positive corona films at the center are lower than those of the negative corona films. In positive corona, essentially there is no corona-unaffected region like the surrounding region far from the negative corona centre region. In previous chapters, (the study of negative corona films) this outside region was referred to as a control region; a region with a film grown by conventional thermal oxidation. In positive corona this surrounding region will be referred to as the "outer" region, as opposed to the center corona region.

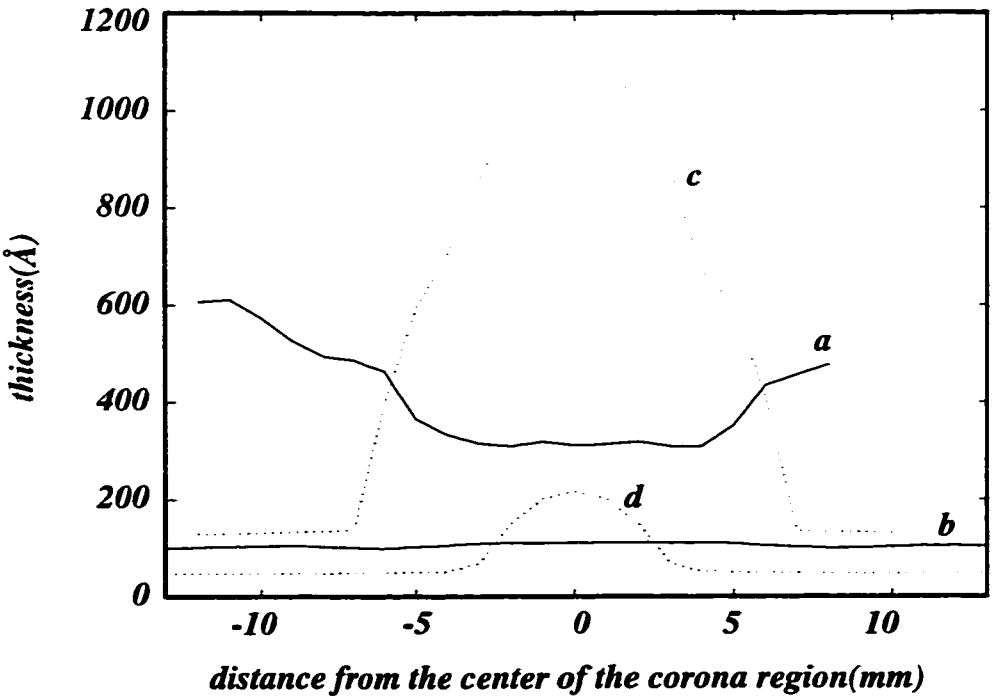

Fig. 5.1: Typical profiles of positive corona films in thin and thick film regimes grown at 800°C. Typical profiles of the negative-corona films grown in similar conditions are also shown in the figure for comparison.

(+) (a): t_{cor}= 150 minutes, I_{cor}= +3μA; (b): t_{cor}=25 minutes, I_{cor}=+2 μA.

(-) (c): t_{cor}= 150 minutes, I_{cor}= –3μA; (d): t_{cor}=25 minutes, I_{cor}=-2 μA.

Fig.5.1 also shows that in positive corona films the shape of the thickness profile changes as the film thickness increases. Thin oxides have the highest thickness in the centre region, while thicker oxides have the highest thickness in the outer regions.

For comparison, it should be noted that in the plasma oxidation of Si using oxygen plasmas in a cathodic condition, it has been reported that the oxidation generally ceases after a few tens of nanometers [18]. However, in positive corona, with the same voltage polarity on the wafer during oxidation, there was no indication of stopping the oxidation process, at least not up to several hundred nanometers (> 200 nm) .

Similar to the negative corona treatment procedure explained in Chapter 3, a positive corona treatment was applied to already-grown thermal oxide films, to create positive corona-treated films. Fig.5.2 shows some typical results. As the figure shows there is an extra growth which occurs mostly on the outer region of the film. (The curves "a" and "b" in the figure are shown again more clearly in Fig.5.3).

Figs. 5.3 show the refractive index profiles of the two positive corona treated films, along with their thickness profiles. As the figures show, the outer regions of the films have lower refractive indices compared to the centre regions. This is a different behavior from that of negative corona-grown or -treated films, for which the lower refractive indices exist at the center corona region. However, as the results show, still there is a relaxation phenomenon which occurs during treatment, indicated by the refractive indices being lower compared to those of the original oxide films thermally grown at same temperature of corona procedure. (For ~ 800 °C thermally grown oxide film, the refractive index is about 1.47).

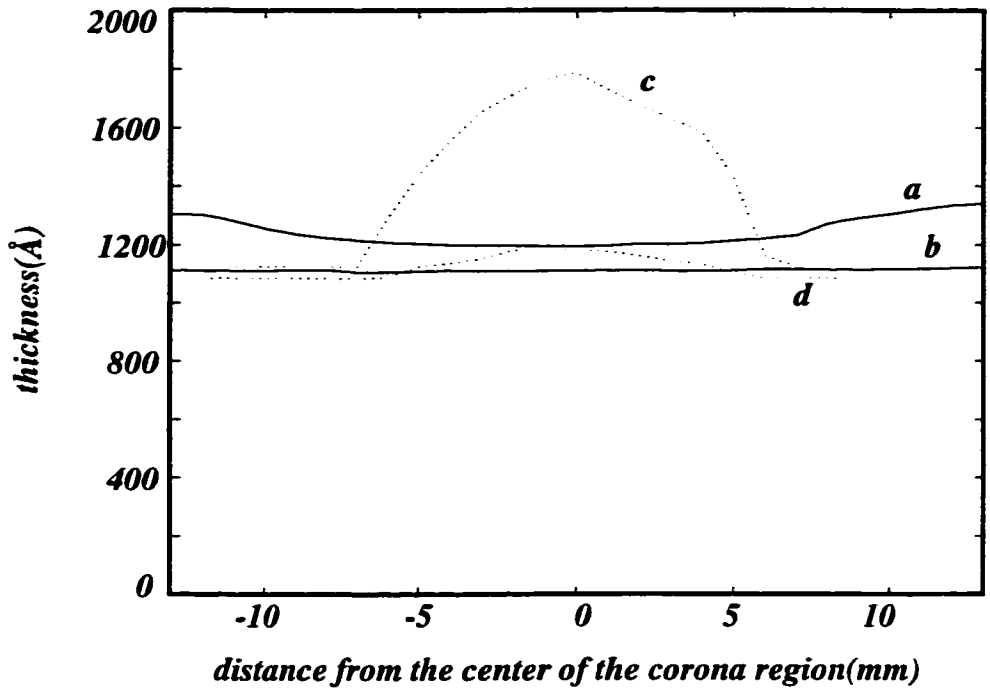

Fig. 5.2: Typical profiles of positive corona treated films , originally grown to about 1100Å thickness by conventional dry thermal oxidation at 800°C and then processed in corona apparatus at 800°C. Some profiles of the negative-corona treated films also shown in the figure for comparison.

(+) (a): t_{cor}= 180 minutes, I_{cor}= +3μA; (b): t_{cor}=25 minutes, I_{cor}=+2 μA.

(-) (c): t_{cor}= 135 minutes, I_{cor}= −3μA; (d): t_{cor}=20 minutes, I_{cor}=- 2 μA.

5.3 Q_f and D_{it} Results of Positive Corona Films

Using the same procedure that was used to fabricate MOS structures on negative corona films, MOS structures were fabricated on positive-corona grown and positive corona-treated films. The detailed fabrication procedures can be found in Appendix B.

Fig.5.4 shows a typical profile of Q_f for a positive corona film. The condition of oxi-

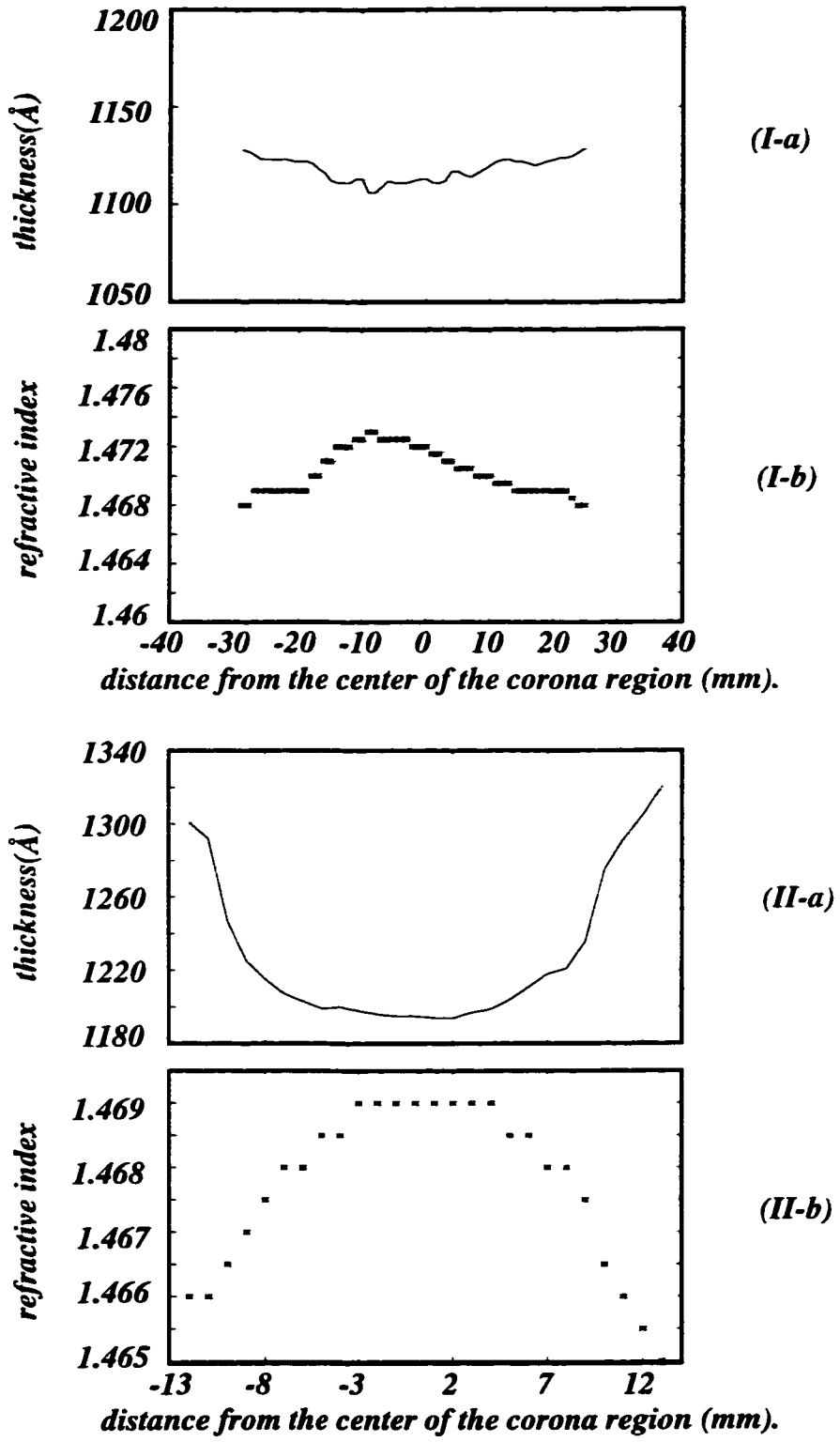

Fig. 5.3: Profiles of a): thickness and b): refractive index for two positive corona-treated films, originally grown to about 1100Å thickness by conventional dry thermal oxidation at 800°C and then processed by corona at 800°C for;

I: t_{cor}= 25 minutes, I_{cor}= +2μA, and II: t_{cor}=180 minutes, I_{cor}=+3 μA.

dation is shown in the figure. As the figure shows, Q_f in all regions of the wafer is in the range of $10^{13}/cm^2$. It is higher in the outer region, and lower in the centre corona region, appearing to approximately track the thickness profile. For relatively thick positive corona -grown or -treated film, the threshold voltages (V_{th}) were higher than the limit of our measurement equipment. For the same reason, for all the samples, D_{it} was not accurately measurable, but must be $\geq 10^{12}cm^{-2}eV^{-1}$.

As shown in Chapter 3, negative corona films have Q_f levels in the range of $10^{11}/cm^2$ similar to those found in standard thermal oxidation at similar range of oxidation temperature. The Q_f results of positive corona films show that the films have, electrically, much lower quality compared to the negative corona and standard thermal oxide films.

Some other Q_f results of positive corona films are presented later in Chapter 7 [see Tables 7.1 (on page 113) and 7.2 (on page 114)].

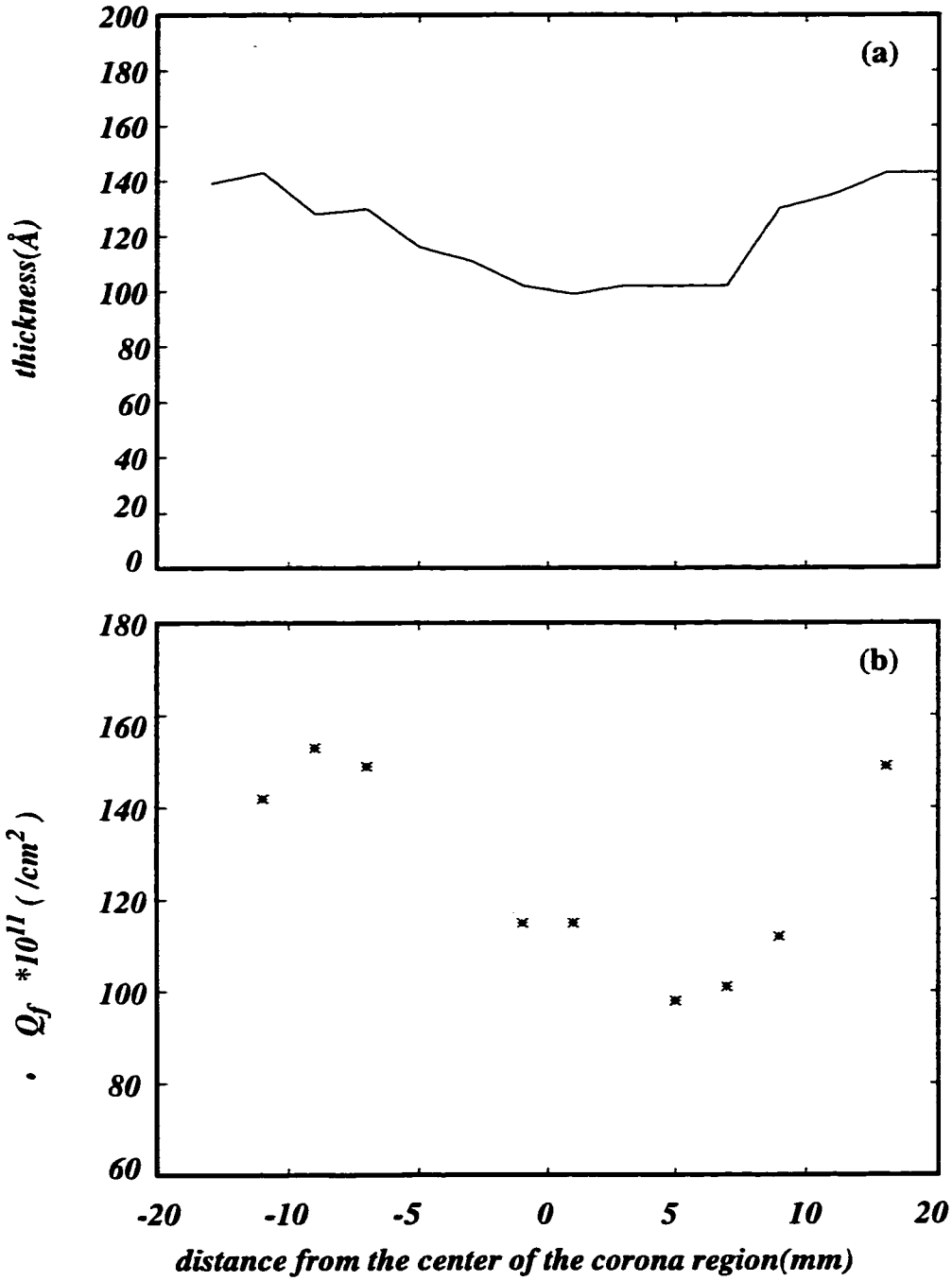

Fig. 5.4: Profiles of a): thickness and b): Q_f for a positive corona-treated film, originally grown to about 1100Å thickness by conventional dry thermal oxidation at 800°C and then processed in corona apparatus at 800°C for 25 minutes. Needle current = +2μA.

5.4 Summary Comparison Between Negative and Positive-Point Experimental Phenomena

Negative- and positive-point corona-discharge oxidation processes result in markedly different oxide thickness profiles. In the negative-point case, the maximum enhancement is exactly under the needle, with a circularly-symmetric bell-shaped profile decreasing to the level of the outer region. This outer region appears to be unaffected by the corona, since it always grows [28-30] to the same level as a standard thermally-oxidized control oxide grown at the same temperature in the same ambient.

In the positive-point case, the oxidation enhancement profile is entirely different from the negative-point case. The maximum enhancement is usually not directly under the needle. Instead, the oxidation rate is enhanced over most of the wafer surface, regardless of wafer size, up to 3-inch wafers tested. The enhancement profile is less predictable, and less radially-symmetric than in the (-) point case. Also, none of the enhancements are as great as in the (-) point case. The enhancement is moderate in a relatively circular center region, which has approximately the same radius as the (-) point enhanced region. The enhancement in the region outside this circle is greater than in the center region. Thus, unlike the (-) point case, there is no control region in this (+) point case. The relative enhancement of the inner and outer regions of the sample varies dramatically with treatment current and thickness. The enhancement of the outer region becomes much greater than that of the inner region at higher currents and greater thicknesses.

The refractive index data of both positive and negative corona films show that the relaxation of the oxide structure happens in both processes. However, the lower values of refractive index are located at the outer region in positive case, and at the center region in negative case.

The electrical properties of the negative-point oxides have been found to be relatively

close to those of thermal oxides grown at the same temperatures [28,38,39]. In particular, high-frequency C-V analysis has shown that Q_f has levels in the low-to-mid $10^{11}/cm^2$, similar to those found in standard thermal oxidation at low temperatures.

The electrical properties of (+) point oxides are drastically worse than in (-) point. High-frequency C-V analysis reveals Q_f levels often $>10^{13}/cm^2$. The Q_f levels are highest in the outer region, where the oxide thickness enhancement is greatest.

Different behavior of the films grown under two different voltage polarities is also reported in the study of the films produced by the positive and negative biased plasma-enhance-chemical-vapor-deposition (PECVD) processes [18]. The study has shown that anodic biased plasma films have much better electrical properties compared to cathodic biased films. Also, it has been reported that with positive potentials on the oxide surface, the oxidation generally stops after a few tens of nanometres [18]. The enhancement of the oxidation rate of silicon by positive corona is thus novel, in that, at least at 800°C, the enhancements for positive corona are continued to much higher thicknesses.

5.5 Chapter 5 Contributions

- The trends in positive-point corona-oxidation, first discovered by Modlin *et al.* [22], were confirmed:
  - The thickness profile shape in (+) corona is wider compared to that of (-) corona, and appears to be limited by wafer size.
  - The thickness profile in (+) corona is not as regular as it is in (-) corona; for thinner films the highest thicknesses are in the center region, while for thicker films the highest thicknesses are in the outside regions surrounding the center.
  - For a given amount of time and current, the maximum thickness enhancement of a (+) corona film is lower than the center region enhancement of a (-) corona film.
- It was found that positive corona-treated films have similar thickness profiles of thick positive corona films (the center region has lower thickness compared to its surrounding regions).
- Similarly to negative corona, positive-point corona treatments of low-temperature thermally-grown SiO_2 films, cause structural relaxation phenomena, as measured by refractive index changes. However, the refractive index of (+) corona treated films is not as low as that of (-) corona-treated films.
- Q_f and D_{it} results showed that the electrical quality of the positive corona films is much lower than standard thermally grown films grown at similar temperature.
- The results of positive corona films are consistent with some other cathodic plasma processes in terms of very poor oxide electrical properties, but quite different in terms of stopping of the film growth seen in the cathodic plasma at certain thicknesses of the film.

CHAPTER 6

FTIR Characterization, and Observations on Corona-Oxide Structure

6.1 Introduction

The distinctive behavior of the oxide film at the boundary region between negative-corona and control regions was demonstrated through electrical characterization in Chapter 3. Based on the results it was suggested that a possible structural mismatch between the two adjacent areas, control and corona, could be the source of this behavior. Corona oxide, grown at low temperatures, has refractive index lower than that expected for thermal oxides grown at similar temperatures. This could imply that the negative-corona-treated region has a more relaxed structure compared to its adjacent control region and that could be the main source of the mismatch. However, the refractive index profiles, like the ones shown in Figs. 2.5 and 2.7in Chapter 2, indicate that the transition of refractive index data between the different regions is smooth. This suggests that the refractive index change is probably not the only reason for the distinct behavior of the films at the boundary regions. To investigate more clearly the condition of the oxide at the boundary region, a study of the physical structure of the corona film is necessary.

Infrared absorption spectroscopy is a powerful tool widely used to characterize oxide film structure. In this chapter the results of Fourier Transform Infrared Spectroscopy (FTIR) analyses, on positive and negative corona samples, are presented.[55] Positive- and negative-corona films are compared and contrasted to each other and to conventional thermal oxides.

6.2 Preparation of Oxide Samples for FTIR

Ten samples, identified as S_1 to S_{10}, with a thermal oxide layer already grown on five of them, underwent the reverse RCA cleaning procedure (Appendix B). The step of dipping in diluted HF was skipped for the samples with oxide layers. Samples S_1 to S_5 had ~1100Å oxide grown by conventional dry oxidation at 800°C for about 50 hours. Four of these wafers were used for corona treatment and the fifth one remained untreated as a reference. Wafers S_6 to S_9 had bare silicon surfaces after the clean. Three of them, S_6 , S_7, and S_8 were used for corona growth, and wafer S_9 was used as a reference to check any possible effect of the corona process on the FTIR measurement of the bare silicon substrates. Sample S_{10} had ~1150Å oxide layer grown by conventional dry oxidation at 1150°C for about 33 minutes. This high temperature oxide film, with a relaxed structure and low refractive index, was used also as a reference. Table 6.1 shows the condition of the samples before the corona processes. Also shown are the corona process conditions for each sample. The negative and positive polarities of the corona current represent the negative and positive-point corona processes, respectively.

After doing the corona processes the overall procedure to characterize the oxide films was as follows:

1- The backside oxide of all the samples was etched off ;

2-The thicknesses and refractive indices of the oxide films were measured. For corona films, the measurement was done on different regions of the films;

3- FTIR spectroscopy was done on the wafers. For corona wafers this was done in least at three different locations; one in the center of the corona region, one at the boundary region between corona and control areas, and one in the control area far from the corona region.

For samples S_3 to S_6, the following procedures were followed:

Table 6.1:The conditions of samples before corona processes and the conditions of the corona processes.

Sample	type (all ~10 ohm-cm)	condition before corona procedure	corona current (μA)	corona time (minutes)	corona-process temperature (°C)
S_1	<111>, P-type	~1100Å thermal oxide(dry) grown at 800°C	-2	20	800
S_2	<111>, P-type	~1100Å thermal oxide(dry) grown at 800°C	-2	12	800
S_3	<111>, P-type	~1100Å thermal oxide(dry) grown at 800°C	-3	135	800
S_4	<111>, P-type	~1100Å thermal oxide(dry) grown at 800°C	+3	180	800
S_5	<111>, P-type	~1100Å thermal oxide(dry) grown at 800°C	---	---	---
S_6	<100>, N-type	bare silicon	-3	150	800
S_7	<100>, N-type	bare silicon	+3	150	800
S_8	<100>, N-type	bare silicon	+3	180	800
S_9	<100>, N-type	bare silicon	----	----	---
S_{10}	<100>, N-type	~1150Å thermal oxide (dry) grown at 1150°C	----	----	---

4-An Etch-back step was done to remove a fraction of the oxide films. These were done in dilute HF for times listed later in tables 6.3 to 6.6.

5-Steps 2, 3, and 4 were repeated a few times, until the oxide films were completely etched off.

6- At the end, another FTIR measurement was done on the resulting bare silicon surfaces.

For samples S_1, S_2, S_7, S_8, S_{10}: the oxide films of the samples that did not go through the etch-back process were then etched off in order to do FTIR measurement on their bare silicon substrates. The FTIR results on bare silicon surfaces were used as reference data for the FTIR analysis. Subtraction of these spectra from FTIR spectra measured in step 2, which included the effects of both oxides and substrates, gave the net FTIR spectra of the oxide films. The reference data from the bare silicon substrates of all the samples were similar to FTIR spectra of the reference bare silicon sample S_9.

All the FTIR measurements of each sample have been done at the same location (for thermal oxides) or locations (for corona oxides) at different iterations of FTIR measurements.

6.3 Thickness and Refractive Index

Fig.6.1 shows the oxide thickness and refractive index profiles of the sample S_1. The measurement was done using an ellipsometer (Gaertner L3W26C) at the wavelength 633 nm. To reduce the effect of equipment calibration on the refractive index results, and also to compare the data with the refractive index of a thermal oxide film grown at high temperature, the thickness and refractive index of high-temperature grown reference sample S_{10} was also measured in the same measurement session as sample S_1. The values of the right side axis (ΔN_f) in Fig.6.1(b) show the offset of the S_1 data compared to the refrac-

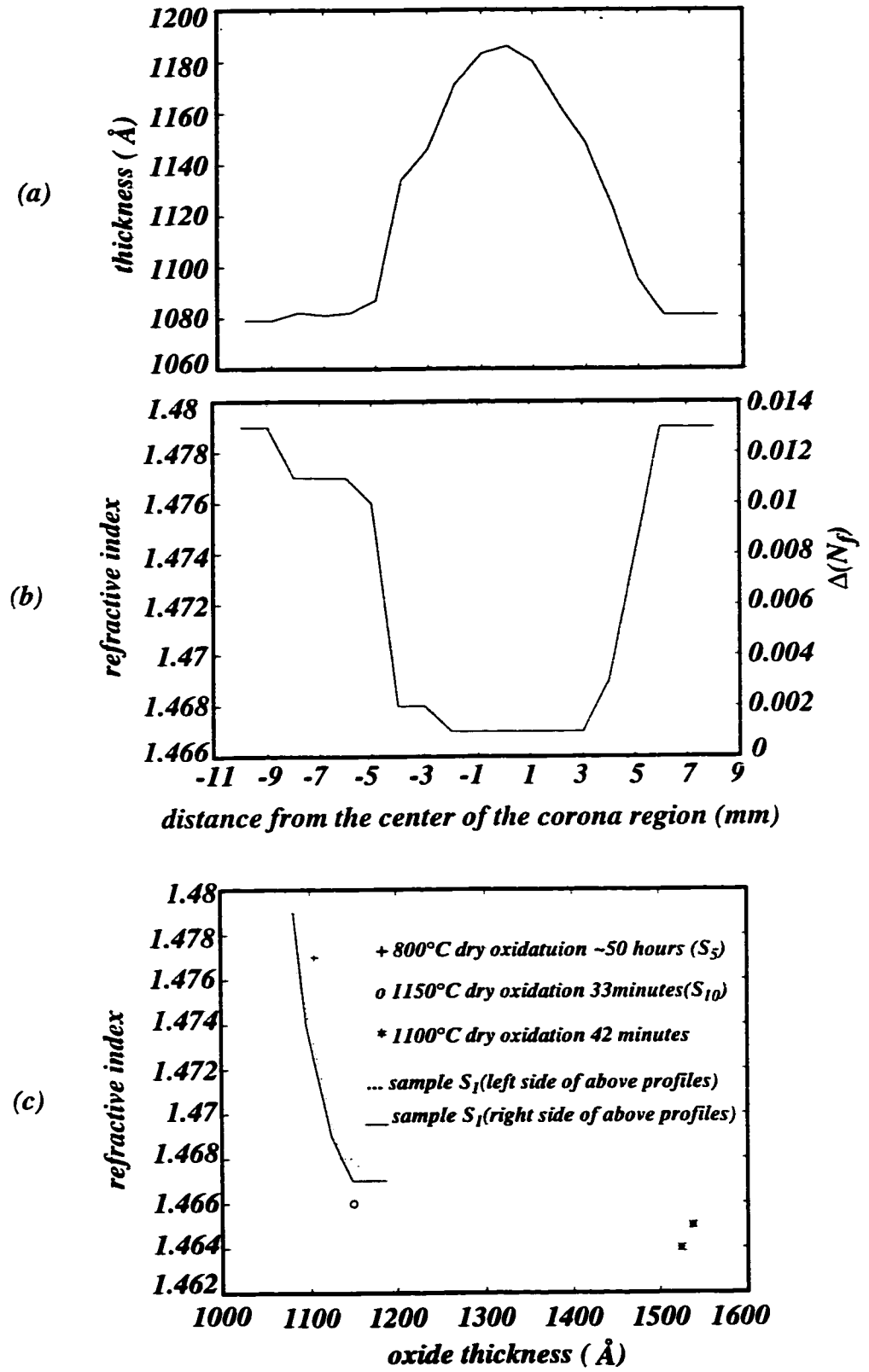

Fig. 6.1: (a) thickness, (b) refractive index, and (c) the variation of refractive index vs. oxide thickness, of sample S_1.

tive index of sample S_{10}. As the values show, at center region the refractive index is very close to the refractive index of the high temperature oxide. This indicates a relaxed structure at the corona region.

To show that the lower refractive indices at the center region are not simply related to the higher thicknesses of the film [56] at the center region, the curve in Fig.6.1(c) is drawn. The 1100°C- and 1150°C-grown films have very similar physical structure (and measured refractive indices at equal thickness [26,56]). The small variation in refractive index between the 1100°C-grown ~1500Å and 1150°C-grown ~ 1150Å oxides is due to the thickness variation [56]. The rate of change of refractive index with oxide thickness in the (-) corona case is much greater than this. Thus, it cannot be simply due to thickness change, but must be also due to a substantial density change.

Fig.6.2 shows similar data of Fig.6.1(c) for samples S_2, S_3, and S_4. For other corona samples S_6, S_7, and S_8, which had been grown on bare silicon instead of on top of 1100Å, the refractive index could not be measured accurately on the low-thickness regions [26]. The approximate thicknesses of these regions was measured with the assumption of a suitable refractive index value. The oxide thickness profiles are shown in Fig.6.3 .

Also, to have more precise data with respect to the extra oxide thickness in the corona regions, the data of Table 6.2 was calculated. The table shows the three factors that have roles in the growth of film at the corona regions [26]; the expected thermal growth, the

Table 6.2: Extra thickness at corona region due to different factors.

sample	expected extra thermal growth (Å)	expected swelling due to relaxation (Å)	remaining extra growth due to corona (Å)
S-1	6	25-30	72-77 (center)
S-2	4	25-30	27-32 (center)
S-3	40	25-30	656-661 (center)
S-4	53	25-30	35-40 (center) 70 (outer)

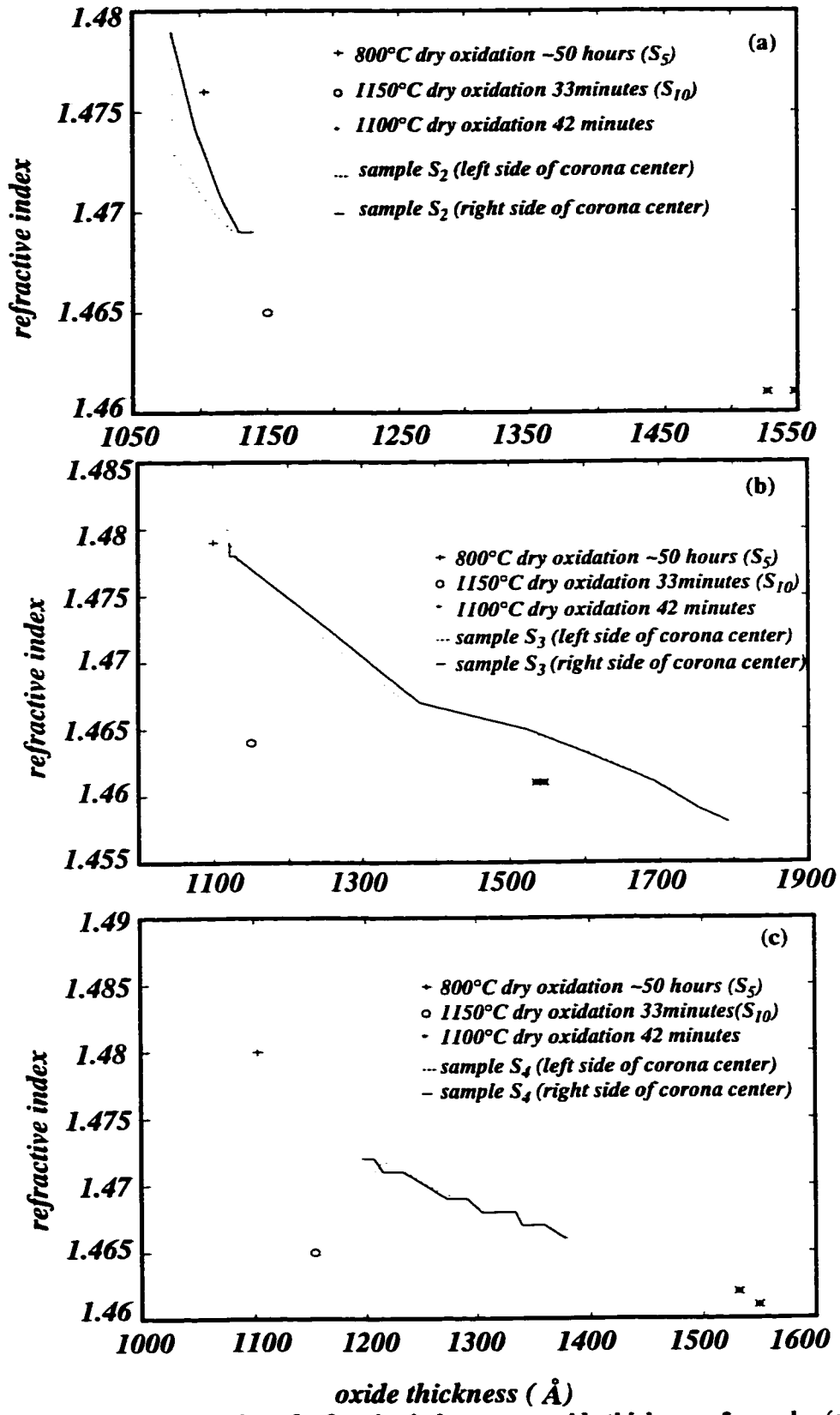

Fig. 6.2: The variation of refractive index verses oxide thickness of samples (a): S_2, (b): S_3, and (c): S_4.

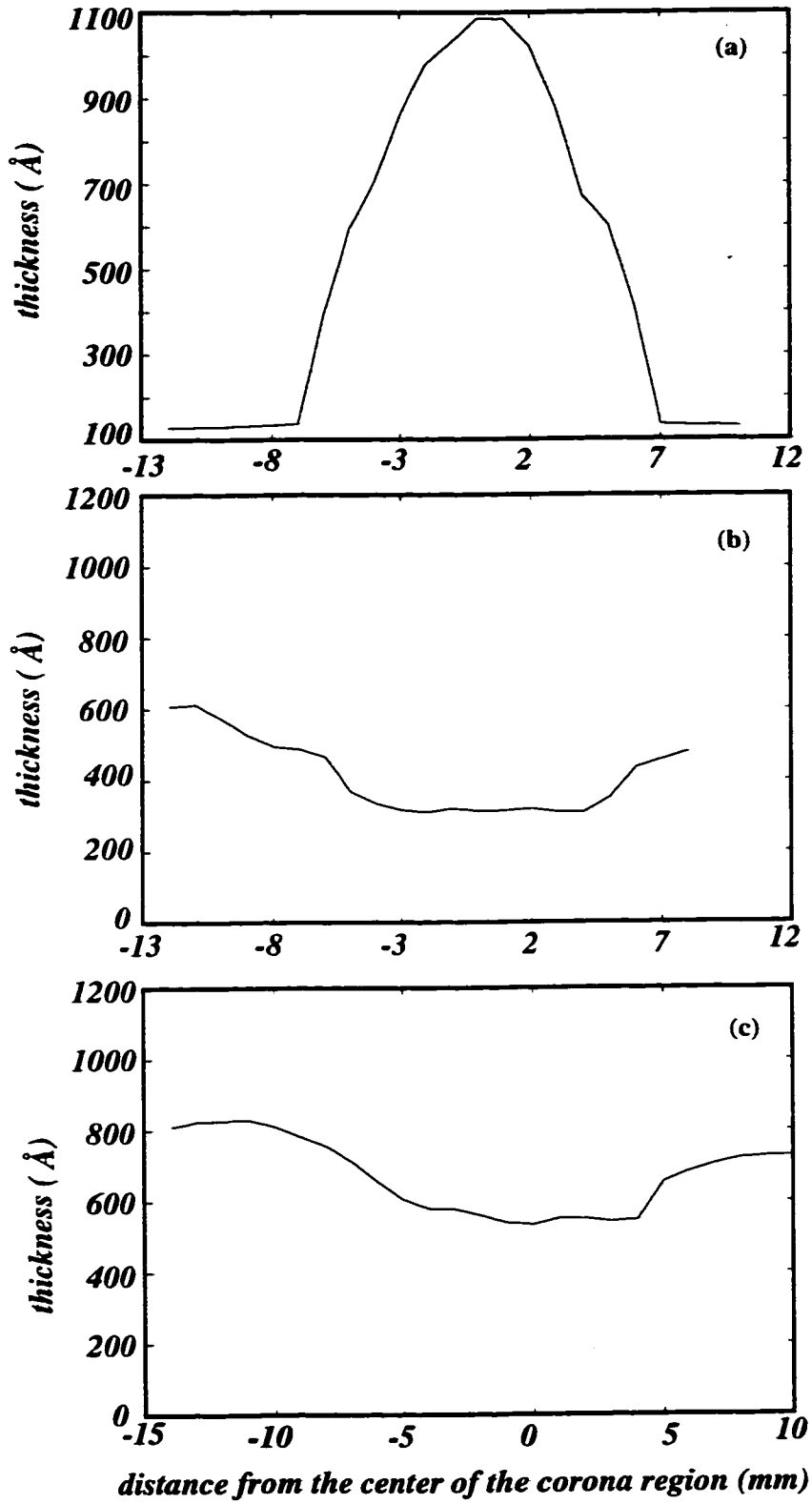

Fig. 6.3: Thickness profiles of samples (a): S_6, (b): S_7, and (c): S_8.

expected "swelling" due to relaxation , and the growth due to corona. Thus, the extra thicknesses in the corona regions are clearly not simply due to relaxation. There is extra oxide growth due to the corona as well. This table will be referred to in the discussion of FTIR results.

6.4 Etch-back Results

Samples S_3 to S_6 and S_{10} underwent etch-back processes. In this way, the etch rates of the films at different regions, and at different distance from the Si/SiO_2 interface, were obtained. Also, by doing FTIR measurement after each step of etching, the structure of the oxide at different distances from the Si/SiO_2 interface was studied.

Tables 6.3 to 6.6 show etch rates of the films. The etchant was a solution of 10 ml. of 49% HF in 500 ml. D.I. water. Measuring the thickness and refractive index after each etching process was done using a single-wavelength ellipsometer (Rudolph Scientific AutoEl II) operating at a wavelength of 633nm. When the film thickness fell below 60 nm. the thicknesses were calculated assuming the refractive index of the unetched film. The thicknesses and refractive indices of the film after each etching process are also shown in the tables.

The tables show that the etch rates of the negative corona films are higher than those of the control region. In negative corona films the locations at which the oxide was completely etched off first were the circular boundary regions between control and corona areas. For positive corona, the etch rate is lower, and is much lower at the regions far from the center. If low etch rate were an indication of oxide quality, this would tend to indicate that positive corona has better quality and negative corona has worse quality compared to that of the thermal oxide. However, the electrical behavior of negative corona films as seen in Chapter 3, is close to that of thermal oxide, and, at least in terms of Q_f, positive

Table 6.3: Etch back results of sample S_3.

location		center (0)	boundary (6 mm)	outer (20 mm)
before etch	t_{ox} (Å)	1804	1385	1119
	N_f	1.451	1.46	1.473
1'st etch (2 minutes)	t_{ox} (Å)	1626	1024	1015
	N_f	1.458	1.473	1.474
	etch rate (Å/min)	89	180	52
2'nd etch (4 minutes, 25 seconds)	t_{ox}(Å)	1268	832	798
	N_f	1.459	1.468	1.476
	etch rate (Å/min)	81.06	43.47	49.13
3'rd etch (5 minutes, 15 seconds)	t_{ox} (Å)	879	521	536
	N_f	1.463	1.476	1.483
	etch rate (Å/min)	74.10	59.24	49.90
4'th etch (6 minutes)	t_{ox} (Å)	419	bare silicon	241
	N_f	-	-	-
	etch rate (Å/min)	76.67	-	49.17
5'th etch (< 7 minutes, 20 secs)	t_{ox} (Å)	bare silicon	bare silicon	bare silicon
	N_f	-	-	-
	etch rate (Å/min)	57.16	-	38.07

Table 6.4: Etch back results of reference sample S_5.

before etch	t_{ox} (Å)	1100
	N_f	1.472
1'st etch (4 minutes, 35 secs)	t_{ox} (Å)	831
	N_f	1.477
	etch rate (Å/min)	58.69
2'nd etch (4 minutes, 30 seconds)	t_{ox} (Å)	602
	N_f	1.481
	etch rate (Å/min)	50.89
3'rd etch (6 minutes)	t_{ox} (Å)	307
	N_f	-
	etch rate (Å/min)	49.17
4'th etch (6 minutes, 50 seonds)	t_{ox} (Å)	bare silicon
	N_f	-
	etch rate (Å/min)	44.93

Table 6.5: Etch back results of sample S_4.

location		center (0)	(9 mm)	outer (17 mm)
before etch	t_{ox} (Å)	1196	1273	1378
	N_f	1.467	1.464	1.461
1'st etch (2 minutes)	t_{ox} (Å)	1107	1150	1282
	N_f	1.464	1.462	1.457
	etch rate (Å/min)	44.5	61.5	48
2'nd etch (8 minutes, 12 seconds)	t_{ox}(Å)	741	792	943
	N_f	1.473	1.467	1.463
	etch rate (Å/min)	44.63	43.66	41.34
3'rd etch (8 minutes, 12 seconds)	t_{ox} (Å)	371	434	600
	N_f	-	-	1.472
	etch rate (Å/min)	45.12	43.66	41.83
4'th etch (<13 miutes)	t_{ox} (Å)	bare silicon	bare silicon	bare silicon
	N_f	-	-	-
	etch rate (Å/min)	47.36	-	-

Table 6.6: Etch back results of sample S_6.

location		center (0)	boundary (5 mm)	outer
before etch	t_{ox} (Å)	1087	670	~100
	N_f	1.459	-	-
1'st etch (2 minutes)	t_{ox} (Å)	904	593	bare silicon
	N_f	1.461	-	-
	etch rate (Å/min)	91.50	38.50	-
2'nd etch (3 minutes, 15 seconds)	t_{ox}(Å)	653	240	bare silicon
	N_f	-	-	-
	etch rate (Å/min)	77.23	108.62	-
3'rd etch (4 minutes, 15 seconds)	t_{ox} (Å)	222	bare silicon	bare silicon
	N_f	-	-	-
	etch rate (Å/min)	101	-	-
4'th etch (4 minutes, 5 seconds)	t_{ox} (Å)	bare silicon	bare silicon	bare silicon
	N_f	-	-	-
	etch rate (Å/min)	54.36	-	-

corona films , as seen in Chapter 5, have very low quality. These results suggest the likelihood of a different structure for corona oxide films.

6.5 Fourier Transform Infrared Absorption Spectroscopy

Infrared absorption spectroscopy was used to obtain information about oxide film structure. When a beam of infrared light impinges at normal incidence on an oxide film, the transmitted light has lower intensity and a different spectrum compared to the original light. This is caused by infrared absorption at frequencies that match with natural vibrational frequencies of the atoms in the film structure. The spectra of the transmitted light reveals various information about the film.

A Nicolet Model 550 Fourier transform infrared spectrometer, located at NRC [1] was used to measure the absorption spectra of the oxide films at normal incidence.[55] The absorbance of the substrate after etching off the films was subtracted from the absorbance of the film plus substrate to get the absorbance of the film. The results showed that for all the films the intensity of the SiH, SiOH and H_2O peaks at 2260, 3650 and 3420 cm^{-1}, respectively, were below the sensitivity of the instrument, which is estimated to be 0.2 wt%. The three well-known vibrational modes of a-SiO_2 were visible in the spectra, the rocking mode (R), the symmetrical stretching mode (SS), and the asymmetric stretching mode (AS). Fig.6.4 shows a typical spectroscopy result belonging to sample S_4. As the figure indicates, rocking (R) of the oxygen (O) atom about an axis through the two Si atoms caused the vibration of the lowest frequency band near 450 cm^{-1}. Symmetrical stretching (SS) of the O atom along a line bisecting the axis formed by the two Si atoms

1. This experiment was done at the Institute for Microstructural Sciences at NRC, Ottawa, Ontario, in collaboration with Dr. Dolf Landheer.

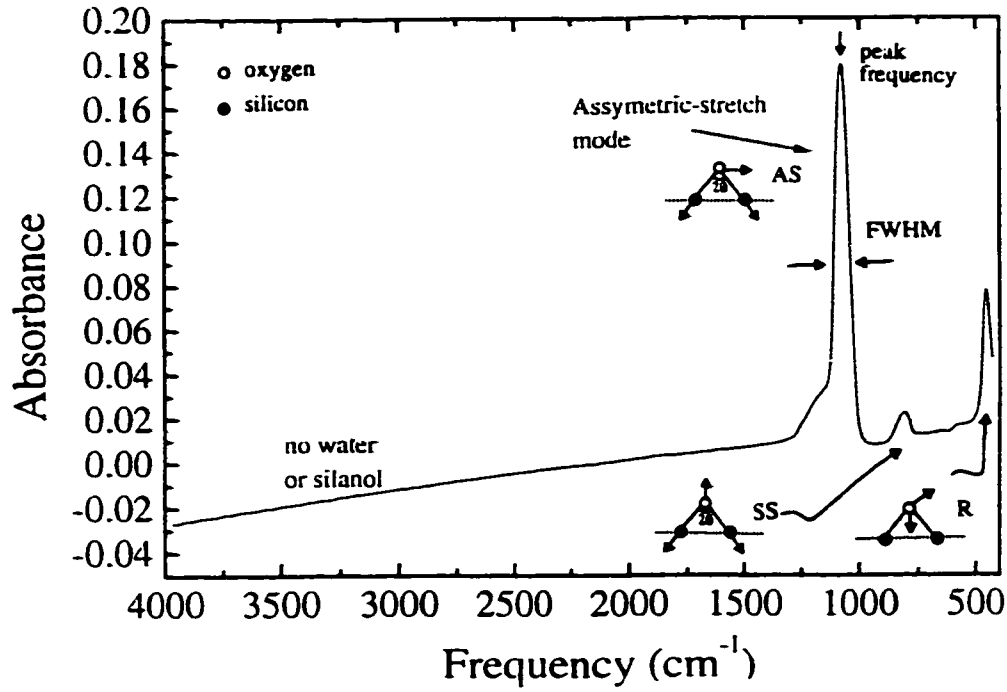

Fig. 6.4: Infrared absorption spectrum of sample S_4. The beam of infrared light impinged at normal incidence on the oxide film. The local vibrational motions of rocking(R), symmetrical stretching (SS), and asymmetrical stretching (AS) of the oxygen atoms with respect to silicon atoms also schematically shown in the figure. The Corresponding effect of each vibration on the spectrum is indicated in the figure. The upper shoulder bond of AS mode centered near 1200 cm^{-1} is caused by the AS_2 mode vibration.

caused the vibration of the frequency band near 800 cm^{-1}. Finally, asymmetric stretching (AS) of the O atom along a line parallel to the axis through the two Si atoms caused the vibration of the frequency band near 1070 cm^{-1}.

In this work we will concentrate on the characteristics of the AS mode. A conventional analysis of the absorbance spectrum involves measuring the FWHM (Full Width at Half-Maximum) and peak frequency for the whole AS feature (see Fig.6.4). The asymmetric stretching mode actually consists of two components: an AS_1 mode in which adjacent O atoms vibrate in phase with each other, and an AS_2 mode in which adjacent O atoms vibrate 180° out of phase with each other [57,58]. The upper shoulder band of the

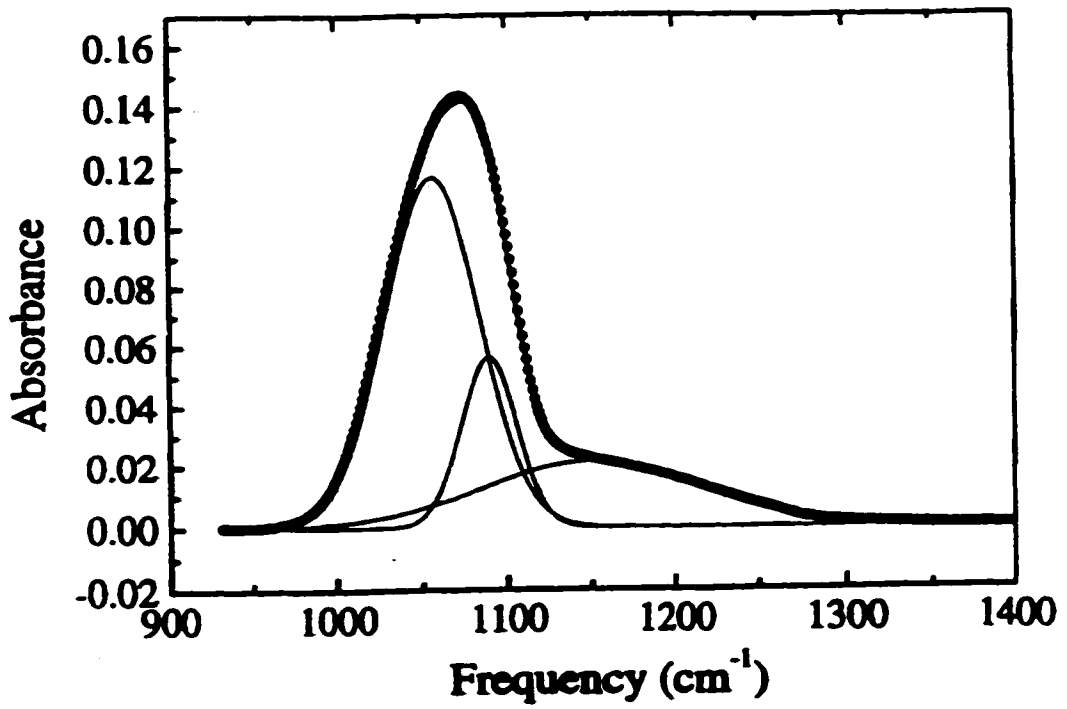

Fig. 6.5: Plot of absorbance as a function of frequency for the AS stretch vibration of sample S_5, thermal oxide grown at 800°C. The fit of the three gaussian components making up the peak and their sum are also shown.

AS mode centered near 1200 cm^{-1}(see Fig.6.4) is caused by the AS_2 mode vibration [57,59,60]

For comparison, Fig.6.5 shows the absorbance spectrum of the AS stretching vibration for the reference sample S_5. Also shown is the calculated absorbance obtained by using three gaussian functions with components v_1, v_2, and v_3 with frequencies at 1055, 1088, and 1149 cm^{-1} fit to the data. The FWHM of the components are, respectively, 65, 40 and 180 cm^{-1}. In comparison, it has been found [61] that thinner films were deconvolved using two gaussians with frequencies of 1050 and 1085 cm^{-1} and FWHM of 65 and 35 cm^{-1}, respectively. The fitting procedure produced excellent fits for the thermal oxide spectra and for all the spectra of the corona-treated and corona-grown samples.

Although the basic features of the AS vibration spectrum were not significantly changed by the corona processing, significant changes in peak position, peak height and

peak FWHM were observed.

Figs. 6.6 (a) and (b) show, respectively, the peak frequency and FWHM for the whole AS feature including the AS_1 and AS_2 components of all the samples, as a function of distance from the corona center. They clearly group into two sets, with the positive corona-processed samples S_4, S_7, and S_8 (corona treated films and films grown from the bare silicon) exhibiting higher frequencies and lower FWHM than the negative corona-processed samples S_1, S_2, S_3, and S_6. For both positive and negative corona-processed samples the frequency increases towards the outer region while the FWHM decreases. For the corona-treated samples S_1 to S_4 there is a change in slope at the boundary of the central-corona treated region. For the corona-grown samples S_6 to S_8 , measurements were only made at three positions, in the centre of the corona region, in the boundary region of the centre area (which was specified by visible change in the color of film caused by different thicknesses) , and in the region far from the boundary region. The FWHM and peak frequency for untreated thermal oxides S_5 and S_{10} grown at 800 °C and 1150 °C are also shown in Figs. 6.6 (a) and (b).

For the negative corona-processed samples the data in the control region are within experimental error of those of the unprocessed 800°C thermal oxide, while for the positive-corona treated samples the data are closer to those of the 1150°C thermal oxide which is fully-relaxed. As the negative corona current or treatment time are increased the deviations in the central corona region decrease, with the sample S_3 treated using -3μA for 135 minutes showing smaller changes in parameters from those measured for the untreated 800°C oxide than the samples S_1 and S_2 treated with -2μA 12 or 20 minutes. The frequency for the corona-grown oxides is lower than that of the samples treated with coronas of the same polarity; however, some of these differences are due to the significantly smaller thickness of the corona-grown samples.

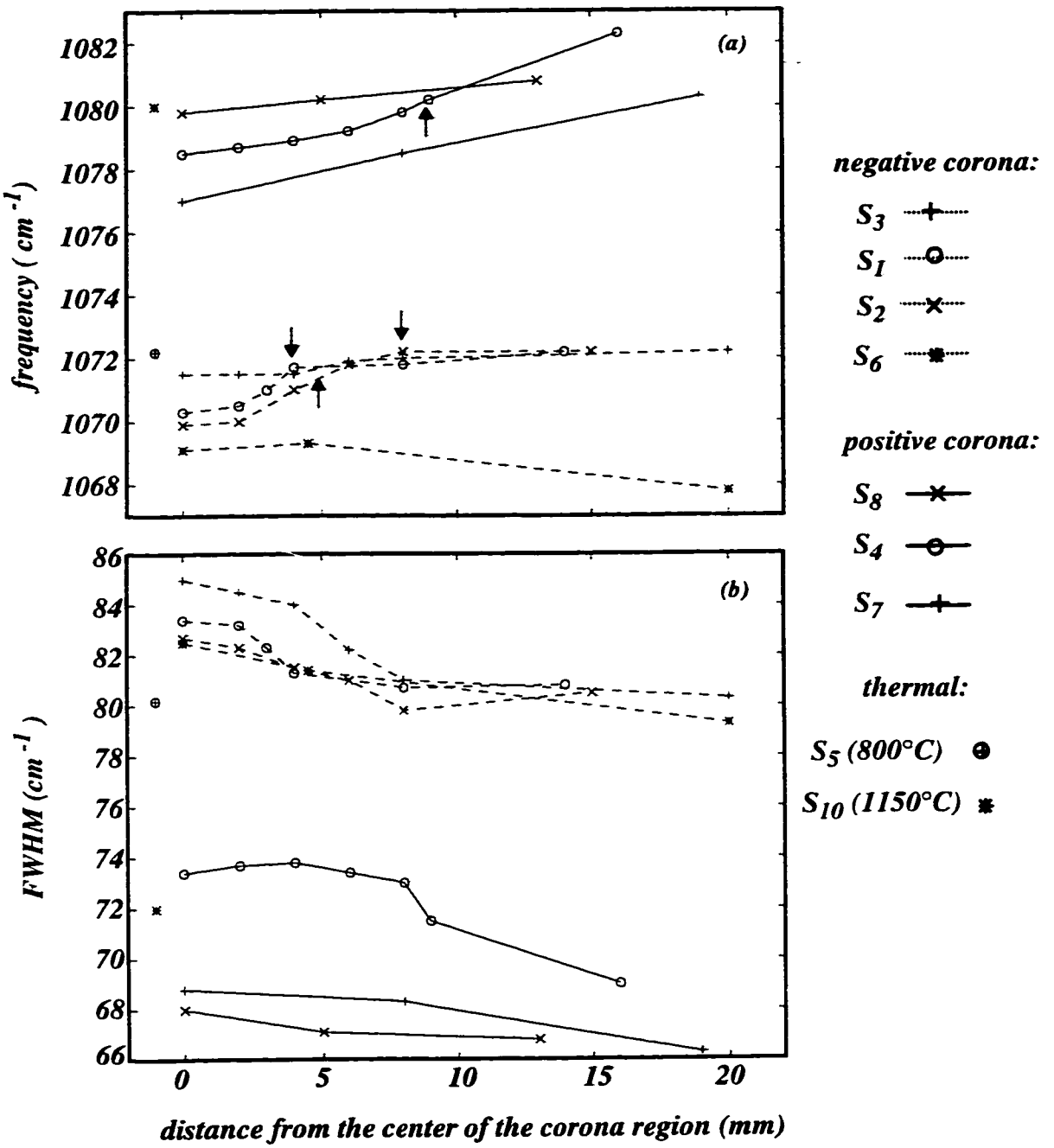

Fig. 6.6: plot of the (a): peak frequency, and (b): FWHM, of the AS stretch vibration as a function of distance from the centre of the corona region for corona-processed oxides. For the corona-treated oxides the position of the transition region between the central and outer regions is marked by an arrow. For the corona grown oxides (S_6, S_7, S_8) measurement were made at the centre, in the transition region, and in the outer region only. Data for the 800°C and 1150°C thermal oxides (S_5, S_{10}) are shown near y-axis.

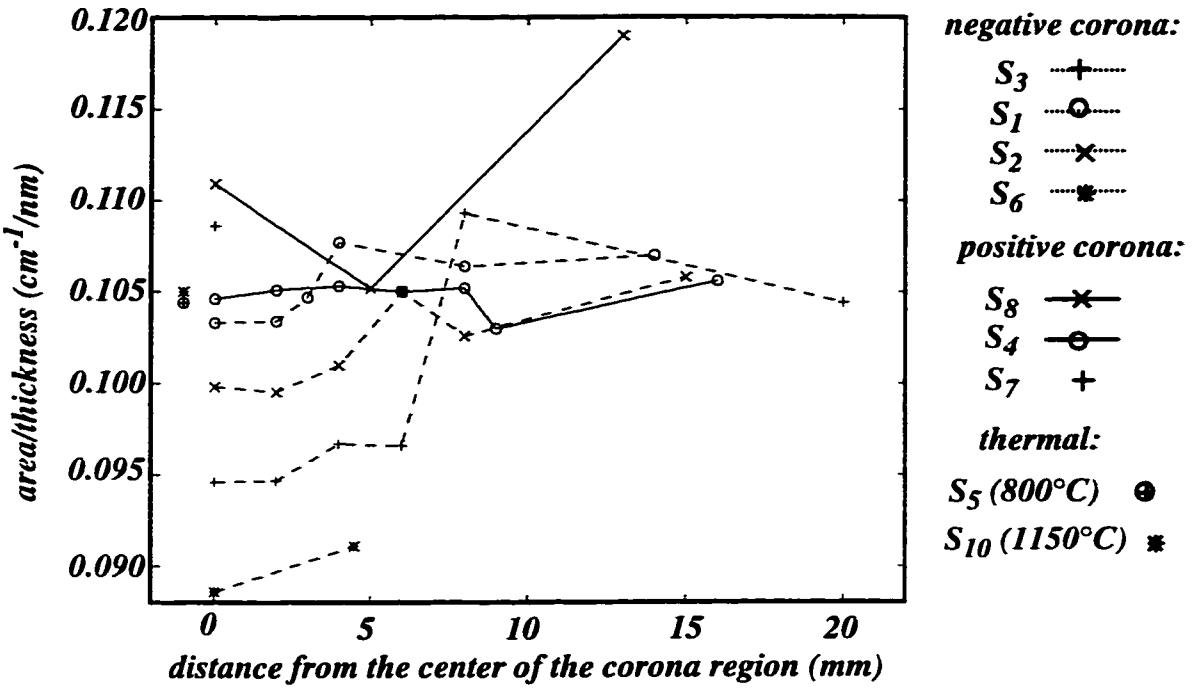

Fig. 6.7: Plot of the peak area of the AS vibration divided by the film thickness as a function of distance from the center of the corona region for corona processed oxides.The measurements were made at the same positions on the same samples as those shown in Fig.6.6. Data for the 800°C and 1150°C thermal oxides (S_5 and S_{10}) are shown near y-axis.

Measuring the mode strength of the combined AS_1 and AS_2 modes involves integrating the whole AS feature and dividing by the film thickness.The corresponding results for the corona and control films are shown in Fig.6.7. As the figure shows, in the outer regions of the corona films, deviations from the results of the 800°C thermal oxide are small. The deviation in the central region for the positive corona processed samples is also small, while for the negative corona-treated samples the central region shows deviations which increase with corona current and time. This latter trend for the changes induced by negative corona processing is opposite to the trend shown for the changes in the frequency measurements shown in Fig.6.6. The magnitude of mode strength is related to the number of corresponding bonds in the unit volume of the film. Table 6.2 on page 85 shows that a part of the extra thickness of corona-treated films is caused by "swelling" which decreases

the density of the film. This decreases the value of mode strength. However the variations of the mode strength shown in Fig.6.7 are more than that which can be explained based only on the swelling of 25-30Å in the films with thicknesses about 1100Å. As is shown in Table 6.2, there is a maximum of 30Å swelling which results in a maximum variation of (30 / 1100) * 100% ≅ 2.7% in the film density. This change of density will decrease the mode strength by 2.7%. The maximum changes in the mode strength of the negative corona-treated films shown in Fig.6.7, are 4.17% for sample S_1, 6.09% for sample S_2, and 14.42% for sample S_3.

It is well known that the peak frequency and FWHM for thermal oxides[62] are a function of film thickness. To establish whether the films exhibited the normal variations with thickness, the measurement was done in the centers of the corona-processed samples at various stages during the etch-back process. Figs. 6.8 (a) and (b) show the result, along with data obtained for the 800°C and 1100°C thermal oxides. The data indicate that the variations with film thickness are comparable for the untreated and treated oxides. It can be deduced that the films are homogeneous within the limits of this technique.

6.6 Analysis & Discussion

It has been shown that for thermal oxides grown at increasing temperature, FWHM of the AS vibration decreases and frequency increases. The data of reference samples S_5 and S_{10} in Figs. 6.6 (a) and (b) also show this feature. Fitch *et al.* [63] attribute this to decreasing stress in the films as the growth temperature is increased. To do so, they used a center force model which gives the relation [64,65] :

$$\upsilon = \upsilon_o \sin(\theta) \tag{6.1}$$

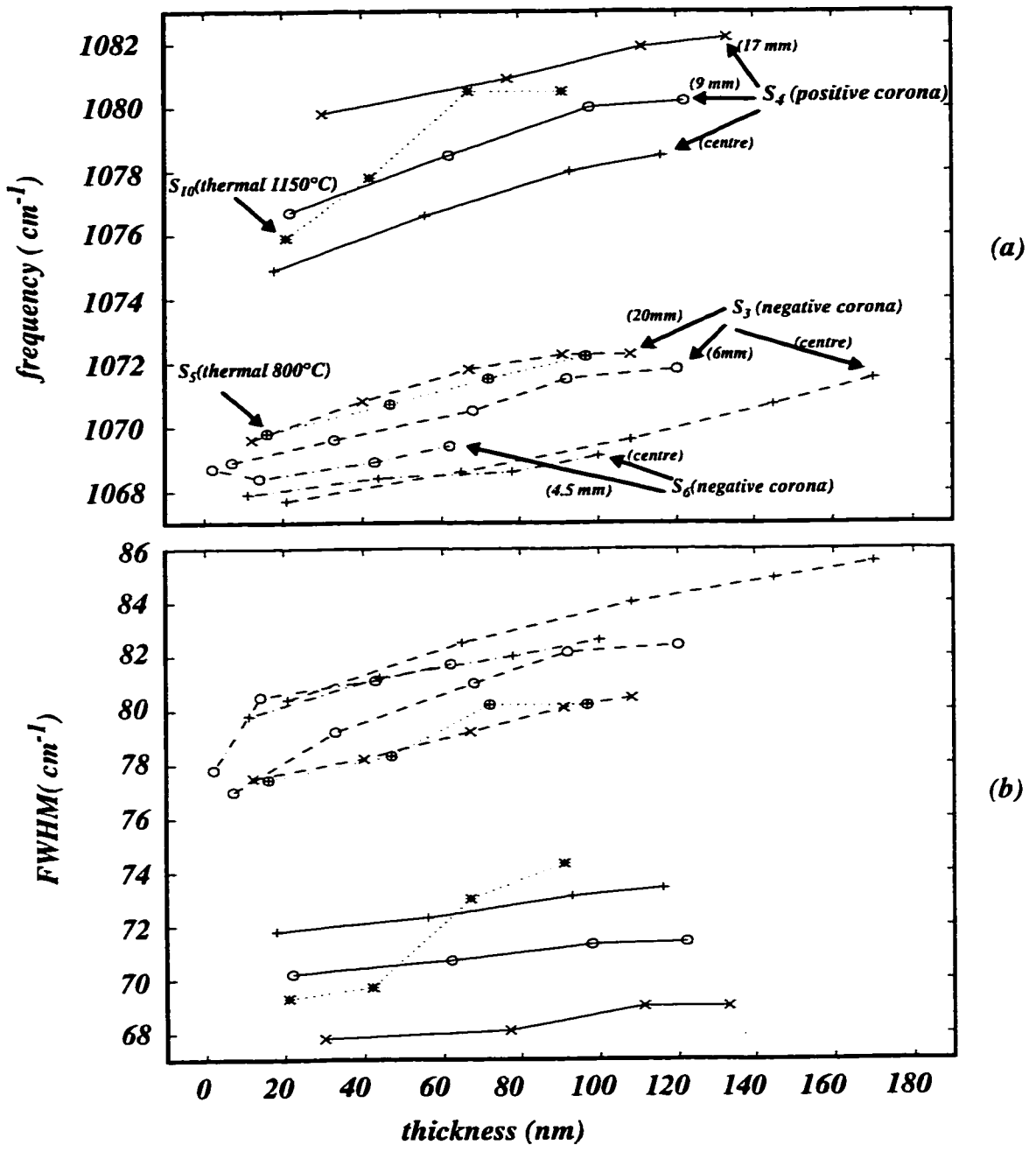

Fig. 6.8: Plot of (a): the peak frequency, and (b): the FWHM of the AS vibration as a function of thickness after etching in dilute HF. Data are shown for the center, transition, and outer region, except for the negative corona-grown sample S_6, where the outer region was thin as-grown. The numbers associated with the arrows show the position of the measured region of the film with respect to the center of corona processed area. Data for the 800°C and 1150°C thermal oxides are also shown for comparison. The indicators used in (b) are similar to the ones used in (a).

where υ is the stretching frequency, θ is half the Si-O-Si bond angle (see Fig.6.4), and υ_o =1134cm^{-1}. The average distance between two Si atoms is equal to $d_{Si\text{-}Si} = 2\, r_o \sin(\theta)$, where r_o is the Si-O bond length. It has been shown that r_o is a slowly varying function of θ [63], and that the angle θ mainly determines the distance between Si atoms. For a high-temperature grown oxide which has a relaxed structure, $d_{Si\text{-}Si}$ is higher, and as a result θ, which has values around 75 degrees, is higher as well. Equation 6.1 shows that for this higher value of θ , the frequency υ would be higher as well. To show why for high temperature relaxed oxide FWHM is lower, the derivative of equation 6.1 can be taken, which gives:

$$d\nu = \upsilon_o \cos(\theta)\, d\theta \tag{6.2}$$

assuming $d\theta \cong \Delta\theta$, and $d\upsilon \cong \Delta\upsilon \cong$ FWHM, Equation 6.2 shows that higher values of θ result in lower values of FWHM.

Within the frame of this modeling, it can be deduced that the outer "control" regions of the negative-corona films (with higher values of υ compared to the "center" regions of the films) have relatively higher θ's, higher $d_{Si\text{-}Si}$'s , and more relaxed structures (lower densities). This is in clear contradiction to the fact that the center regions of negative-corona films, found based on the refractive indices results, have more relaxed structure compared to the surrounding "control" regions. This means that the center region of the negative corona films shows characteristics that are opposite those expected on the basis of the previously established relaxation observed for thermal and corona-treated oxides. In other words, as the oxide relaxes, the bond angle should increase and the frequency should increase as described by Equation 6.1.

These apparent discrepancies can only be resolved by assuming that the structure of

these corona-treated films undergoes modifications that result in changes in the FTIR spectra not simply described by the thickness and density variations. To further describe these structural changes, the FTIR data for the positive corona-treated sample S_4 and the negative corona treated samples S_1, S_2 and S_3 are replotted in Fig.6.9 and compared with the thermal oxide data of Ref.(63). In the figure the refractive index measured at different positions measured from the center of the corona region are plotted as a function of the stretching frequency. The solid line is the data for thermal oxides on <100> Si wafers obtained from Ref.(63) . The data for our 800°C (sample S_5) and 1100°C (sample S_{10}) thermal oxides are also shown, and are slightly shifted from the data of Fitch *et al.* [63]. This shift cannot be a result of the fact that our films are thinner (~1100Å vs 1300Å in Ref.(63)) since this would shift the measured frequency in the opposite direction [62], but

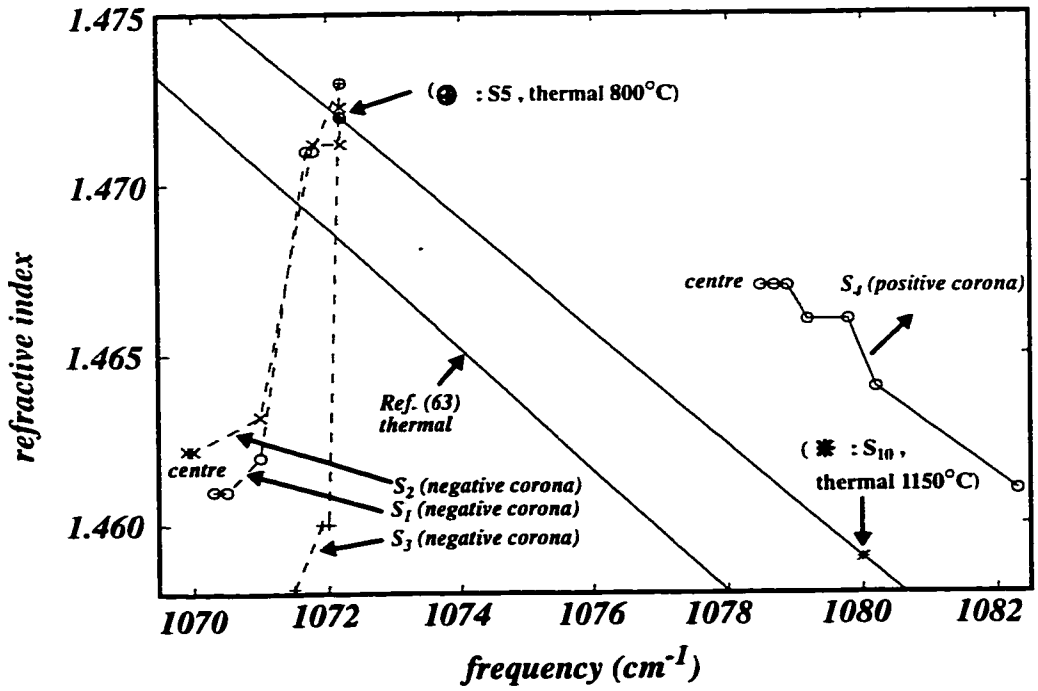

Fig. 6.9: Plot of refractive index versus frequency for positive and negative corona-treated oxides. The data for the 800°C and 1150°C thermal oxides, joined by a solid line, are also shown. The thermal oxide data from Ref. (63) are represented by the other solid line.

are probably due to slight differences in the oxidation conditions and the differing substrate orientation. The data for the positive corona-treated film are shifted to higher frequencies when compared to thermal oxides. For the negative corona data in the central region, the small negative shift in peak frequency is accompanied by the large decrease in refractive index associated with the decrease in density caused by the corona treatment. Similar trends of changes have been also reported for some anodic-plasma oxide films [66].

To show the variation of FWHM and frequency data for corona samples and compare them with similar data for thermal oxides films, the following equation, which resulted from dividing of Equation 6.2 by Equation 6.1, was used:

$$d\nu/\nu = \theta \cot(\theta)\,(d\theta/\theta) \tag{6.3}$$

Equation 6.3 shows that a plot of $d\upsilon/\upsilon$ vs $\theta\cot(\theta)$ gives a measure of the fractional variation ($d\theta/\theta$) of the bond angle. The values of $d\upsilon/\upsilon$ ($\cong$ FWHM/υ) for samples S_1- S_5, and S_{10} were extracted from data of Figs. 6.6 (a) and (b). Also the corresponding values of θ (and from that the values of $\theta\cot(\theta)$) for each υ, were calculated from Equation 6.1. Fig.6.10 shows the $d\upsilon/\upsilon$ data vs. the $\theta\cot(\theta)$ data. The linear fit to the data of thermal samples gives a value $d\theta/\theta$=0.359, considerably higher than the values for thermal oxides ($d\theta/\theta$=0.236), and the value for oxides produced by remote plasma enhanced chemical-vapor deposition (RPECVD) ($d\theta/\theta$=0.296) found in Ref. (63). This higher slope is probably a result of differences in the thermal oxidation and the differing substrates (<111> vs. <100>) used for these studies. For negative-corona treatments with higher currents or for longer times the data points move above the line representing the thermal oxide data.

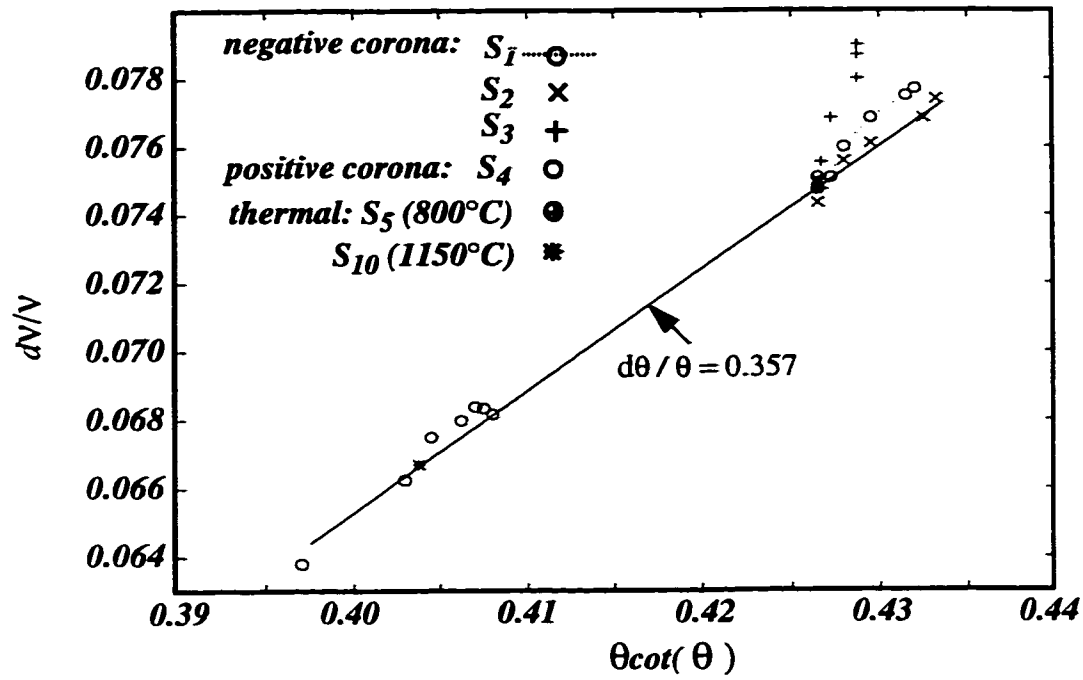

Fig. 6.10: Plot of dV/V (FWHM divided by peak frequency) vs. θ cot(θ) (2θ is the Si-O-Si bond angle), for negative and positive corona treated samples and the 800°C and 1150°C thermal oxides. The solid line is a linear regression to the corona data.

6.7 Conclusions

FTIR analysis was used to study the structure of the both positive and negative corona films. Also, to examine the behaviour of the film properties at different depths in the oxide layers, the etch-back technique was used along with the FTIR analysis.

The FTIR results show that the basic features of the AS vibration spectrum were not changed by the corona processing. However, significant changes in peak position, peak frequency, and peak FWHM were observed. The peak frequency and FWHM of positive corona-treated films shift in a direction consistent with relaxation of SiO_2 films, but the magnitudes of the changes do not follow the trends observed for the relaxation of thermal oxides as growth temperature is increased. The relationship between refractive index and

frequency deviates from that observed for thermal oxides. However, the relationship describing the variation of the ratio of FWHM to peak frequency in terms of the variation of bond angles does fall on the same line as the data for the starting thermal oxides.

For negative-corona treated films, the shift in peak frequency and FWHM are in the opposite (unexpected) direction. The curve of refractive index vs. vibration frequency showed that for negative corona films, higher frequencies correspond to higher refractive indices. This is in contrast to the well-known behavior of thermally grown films where increased oxidation temperature (lower refractive index), is correlated with an increase in vibration frequency. For FWHM, the trends of changes for negative corona films were as well different from those of thermal oxides. Measured at different distances from the center corona region, the mode strength data of the negative corona-treated films indicate a different behavior at the center region compared to that of the control region.

For negative corona films, the data belonging to the outer (control) regions was closer to that of the 800°C thermally grown films, while for positive corona films the data was closer to that of the 1150°C thermal film. For negative corona films, the etch rate in ~1% HF increases, by a factor of approximately 2, in the central region, and it is unaffected in the outer (control) regions. For positive corona films, the etch rate is lower compared to that of thermal oxides. Coupled FTIR and etch-back measurements indicate that both positive - and negative-corona-processed films are homogeneous.

The results of this chapter indicate that the negative corona films have a different structure compared to those of positive corona and thermally grown films. In the case of corona treatment, the negative corona process is capable of changing the structure of an already thermally grown film. The different structure of the negative corona films may explain the distinctive electrical behaviour of the corona film at its boundary region as seen in the results of Chapter 3.

6.8 Chapter 6 Contributions

- FTIR was used to examine and compare both (+) and (-) point-corona-processed cases with each-other and with thermally-grown controls.
- By an etch-back experiment with FTIR measurements after each etch step, the structure of the oxide at different distances from the Si/SiO_2 interface was examined.
- Within the limits of the technique used in this work, it was found that the corona films are relatively homogeneous.
- It was found that despite having the refractive index equal to that of high temperature grown oxide, negative corona films have AS mode frequency close to that of low temperature thermally grown oxide.
- It was found that positive corona films have AS mode frequency close to that of high temperature thermally grown oxide.
- The results suggest that negative corona films have a different structure from that of thermal oxide films.
- The results support the previously suggested hypothesis in Chapter 3 that the distinct behaviour of the oxide films at the boundary regions between negative corona and control regions could be a result of a structural mismatch.

CHAPTER 7

Simulation and Modeling of Growth Mechanisms

7.1 Introduction

As shown in Chapters 3 and 5, negative- and positive-point corona discharge oxidation processes (anodic and cathodic cases, respectively) result in markedly different oxide thickness profiles. In the negative case the enhancement is exactly under the needle with a circularly-symmetric bell-shaped profile over a small area of the wafer. In the cathodic case, the enhancement varies in a complex manner over the entire wafer surface.

It was shown [30] that the extra oxide grown during the negative-point process could be accounted for by distinct components. Most importantly, the dominant component could usually be accounted for by a quantity of O^- ions roughly equal to the integrated charge flux from the measured current in the negative corona. It should be noted that in (-) corona, the gas discharge is localized, with a current density profile approximately bell-shaped, with maximum immediately under the high-voltage needle. It must be assumed that the enhancement is directly related to the current density, which obeys this bell-shaped profile. In contrast, in (+) corona, the enhancement is present across most of the wafer. Since it is unlikely that the actual corona-discharge space charge region in the gas extends out to the edges of a 3-inch wafer, with the point-to-plane gap being only ~5-10mm, we must assume that there is influence from the voltage or current or some other radiation outside of the corona discharge.

This chapter explores the mechanisms involved in corona-discharge enhanced oxidation processes in order to obtain insights of general relevance in silicon oxide growth processes. First, a general review on oxidation mechanisms is given. Then, to explain some

important phenomena related to corona oxidation, a model proposed for low temperature voltage-enhanced U-V-assisted oxidation is reviewed. Finally, to relate growth rates of both positive and negative corona processes to physical parameters of the processes, several experimental cases of both polarities are analyzed to fit equivalent linear and parabolic rate constants, in accord with the standard oxidation model [33]. The fitted enhancements are examined in light of basic mechanisms, and associated physical parameters.

7.2 General Review on Some Models for Oxidation Mechanisms

A brief description of Deal and Grove's linear-parabolic model [33]was presented in Chapter 2. The model is based on the moving of neutral oxygen molecules, and three different factors which determine the oxidation rate : oxidant surface concentration, oxidant diffusion, and the interface reaction. Also in Chapter 2, a brief description of a model with a completely different view of oxidation, proposed by Wolters *et al* [34], was explained. This model is based on the movement of ionic oxidants. The creation of space charges near the SiO_2/Si interface is suggested to be the limiting factor in the oxidation process. Besides these two models, there are also many other models that each try to explain previously unexplained physical features, explain the kinetics of the process, and improve the modeling of the oxidation process. These models include electric field enhancement of diffusing ions [67,68], "fast" diffusion of oxidant through microchannels and micropores in the oxide [69], changing of diffusion coefficients caused by the effect of stress in the oxide layer [70,71], parallel oxidation by two separate oxidizing species [73], and so on.

In a similar manner, since the discovery of plasma anodization of silicon, much effort has been devoted to investigate the kinetics of the process [16-18, 74, 75, 79-86]. Here, as a key issue, the question of the nature of the oxidant species in the growing oxide film has

been addressed by many researchers. Also, in that regard, since during the oxidation there is an electrical current flowing through the oxide, the nature of the charge carriers has been addressed as well [16, 83-86]. Much of the research generally concludes that oxygen ions are the oxidant species, and the enhancement in the film growth rate is due to field-assisted transport of the ions [14, 81,82,86]. These moving ions form a percentage of the oxide current. The remainder of the current is accounted for by the flow of electrons. Also, it is concluded that the creation of oxide charge during the oxidation process, is a limiting factor for growth of the film in the linear regime. This model of plasma oxidation [81,82,86] in fact has much in common with the ionic movement model suggested by Wolters *et al.* for standard thermal oxidation.

Nevertheless, there have been some other suggestions to explain the rate of oxide growth in plasma oxidation. For example, in the first anodic plasma oxidation of silicon reported by Ligenza [32] , it was suggested that the process was diffusion- limited and high growth rate was explained to be due to a high oxidant concentration at the surface. As an another example, in the model suggested by Peeters and Li [74], a loss term for oxidant ions (O^-) during their migration to the SiO_2/Si interface is considered as a crucial factor in the process that limits the oxidation rates for thick oxides.

7.2.1 Oxidation in the Presence of UV Light and Electric Field

Using Ultra-Violet (UV) irradiation to assist the thermal oxidation of silicon has been the subject of some research work [89, 87,88]. Oren and Ghandhi [87] showed that auxiliary light stimulation enhanced thermal oxide growth. Young [89], in a study of the kinetics of photon-enhanced oxidation of silicon, used visible and UV light in a series of experiments. The results of that study led to presenting an electron-active oxidation model applicable for both thermal and "thermal+photonic" cases. The model is mainly based on

the following suggested phenomenon: the emission of the electrons from the substrate into the oxide film and consequently, dissociation of molecular oxygen near the interface by these electrons to create oxygen atoms which have high enough diffusivity to reach Si/SiO_2 interface. There, oxygen atoms combine with Si atoms of the substrate, and create the SiO_2 structure. In the case of applying UV light, the electron flux level emitted from the silicon increases. This causes dissociation of more oxygen molecules, which ultimately causes a higher rate of oxidation.

Shining UV radiation directly on the wafer has also the additional effect of breaking Si-Si bonds at the Si-SiO_2 interface, as suggested by Schafer and Lyon [96], and confirmed by Young and Tiller [93]. The breaking of the Si-Si bonds causes the O atoms or O^- ions to be bonded to the Si atoms relatively easily.

Dolique and Reader [20] examined the effect of using basic UV-assisted processes in addition to a voltage, applied to the silicon wafer. The study showed a considerable enhancement in oxidation rate, compared to that using only UV light. Also, it was found that the growth rate is linear up to higher thicknesses than in standard thermal oxidation. By referring to the ionic growth model of standard thermal oxidation by Wolters *et al* [34], it was suggested that applying the voltage across the growing oxide enhances the flow of O^-. They also suggested that the increase in the linear growth regime was due to an increased charge concentration at the oxide/ambient interface. Taylor *et al* [79] further suggested that parabolic growth starts when the charge at the surface of the oxide becomes too small to supply the oxidation with O^- ions at the same rate. In the case where a voltage is applied, this prolongs the supply of the charge in the linear regime, thus causing the diffusion controlled (parabolic) regime to start later.

7.3 Numerical Simulation of Enhancement Profiles

The enhancement in oxidation rate in the corona process can be explained qualitatively based on the same effects that were suggested for biased plasma oxidation, and oxidation in the presence of UV and electric field. However, as shown above there are various models and kinetics suggested to explain the processes. Moreover, despite many similarities that exist between the corona process and the other above processes, it is quite possible that they have different kinetics.

To explore the kinetics of corona oxidation, in this work, a simulation program based on a linear-parabolic model is developed. A simulation program is designed using linear and parabolic rate constants (as well as an initial thickness, X_{in})[90]. Equivalent values of these parameters are extracted for many experimental results. The results are used to discuss the possible physical interpretations of the extracted rate constants.

7.3.1 Description of the Simulation Program

The program that was used to simulate the oxide profiles of negative and positive corona films is given in Appendix D. The program uses a linear-parabolic growth rate law [33], with spatial variations in the main oxidation parameters. Since the linear-parabolic constants are commonly related to the Deal-Grove physical parameters, these were taken as a starting point for the assignment of the spatial variations.

As shown in Chapter 2, the linear rate constant (B/A) and parabolic rate constant (B) of the linear-parabolic model are related to D, k_i, C* as follows.

$$B \propto C^*.D \qquad \text{and,} \qquad B/A \propto C^*.k_i$$

For the corona process, to account for the effect of the corona on growth rate, the linear-parabolic rate constants at different locations of the sample are defined as follows:

$$C_c^*(x)=F_1(x).C^*, \qquad k_{ic}(x)=F_2(x).\,k_i \qquad \text{and,} \qquad D_c(x)=F_3(x).D$$

$$\Rightarrow \qquad B_c(x)=B*F_1(x)*F_3(x), \qquad (B/A)_c(x)=(B/A)*F_1(x)*F_2(x)$$

where x is distance from the center area of the corona, $C_c^*(x)$, $k_{ic}(x)$, and $D_c(x)$ are, respectively, the modified values of oxidant concentration, interface reaction, and oxidant diffusion for corona process, $F_1(x)$, $F_2(x)$, and $F_3(x)$ are modification factors (functions of position on the wafer) which account for the differences due to the corona, and finally $B_c(x)$ and $(B/A)_c(x)$ are parabolic and linear rate constants of the corona process.

Fig . 7.1 shows profiles of $F_1(x)$, $F_2(x)$, and $F_3(x)$, which were found to best match the experimental data. Figures (a),(b), and (c) show the profiles for positive corona, while Figures (d), (e), and (f) show the profiles for negative corona. Fig. 7.1(a) shows the modification factor expected for the oxidant concentration C* at different locations on the sample in the (-) corona process. $(1 + cxf * |I_{cor}|)$ is the enhancement factor at the center of the corona region, and HLcn is half of the width of the corona-affected region. For the region outside this length, F_1 is equal to "1" (the corona-unaffected region with no modification on the oxidant concentration). The other five curves in Fig. 7.1 are formulated in a similar manner.

More discussion on the functions shown in Fig. 7.1 is brought in the following section, along with presentation of the simulation results.

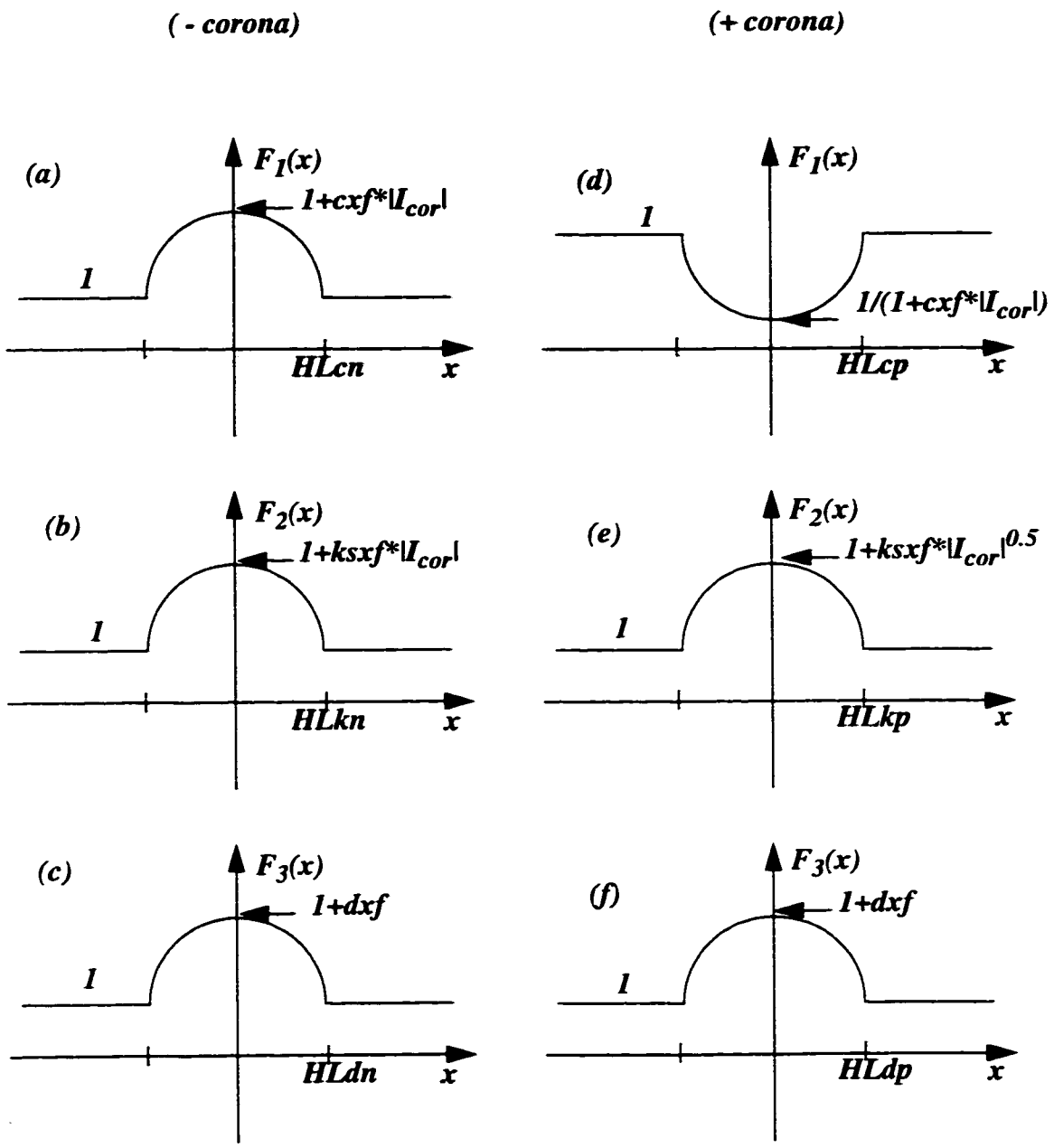

Fig. 7.1: Functions F_1, F_2 and F_3 used to modify the linear-parabolic parameters of standard thermal oxidation to apply for : a,b,c) negative corona process, and: d,e,f) positive corona process.

7.3.2 Simulation Results

Tables 7.1 and 7.2 list several cases of both (-) point and (+) point corona oxidations or treatments. The profiles attained by these experiments are shown in Figs. 7.2 and 7.3. The oxidation rates at certain important features of the profiles,

- the (-) point peak thickness
- the (-) point "control" thickness
- the (+) point center thickness
- the (+) point outer thickness (approximately)

are modeled by use of the simulation program explained above.

For each of the cases in Figs. 7.2 and 7.3 and Tables 7.1 and 7.2, the oxidation rate was fit, in Figs. 7.4 and 7.5, to a linear-parabolic rate law, using rate constants (B/A) and (B) taken from the literature [33], modified by functions F_1, F_2, and F_3 (as defined above), to take account of the corona effect. It was attempted to find factors which were constant for all cases of a given polarity, allowing variation of only the corona current, I_{cor}. As is seen in Tables 7.1and 7.2, two different sets of factors were used for the (-) and (+) cases.

It was found that the negative corona case could be fit by linear variations with I_{cor}. The (+) corona case was more complicated. While other fits may be possible, we found that, for (+) corona, F_2 depends on $|I_{cor}|^{0.5}$, in order to account for the variations of thickness in the outer regions, while F_1 depends inversely on $|I_{cor}|$, in order to account for the relative reduction in the center region. Note that when $I_{cor} = 0$, F_1 and F_2 reduce to unity. The constant factor $F_3 = 1$ for standard thermal oxidation, and needs to take on different (but constant) values for each of the (-) and (+) corona cases.

These rate constants are assumed to vary spatially across the oxide. In the (-) point case, they are all assumed to vary together. In other words, they all have the same radii of

Table 7.1: Experimental Corona Cases and Fitted Rate Constants for negative corona films.

ID	X_{in} (nm)	Si type	I_{cor} μA	t min	(B/A) (E-3) μm/h	(B) (E-3) μm^2 /h	F_1 center outer	F_2 center outer	F_3 center outer	$(B/A)_c$ (E-3) center outer	$(B)_c$ (E-3) center outer	Q_f/q (E11) center outer
1-	0	100	-2	25	1.51	1.29	1.24 1	25 1	6 1	44.6 1.51	9.24 1.29	5 15
2-	0	100	-2	35	1.51	1.29	1.24 1	25 1	6 1	44.6 1.51	9.24 1.29	5* 15*
3-	18	100	-2	7	1.51	1.29	1.24 1	25 1	6 1	44.6 1.51	9.24 1.29	5* 5.5*
4-	0	100	-3	150	1.51	1.29	1.36 1	37 1	6 1	74.0 1.51	10.3 1.29	–
5-	108	111	-2	12	2.53	1.29	1.24 1	25 1	6 1	76.7 2.53	9.43 1.29	~8* ~7.5*
6-	108	111	-2	20	2.53	1.29	1.24 1	25 1	6 1	76.7 2.53	9.43 1.29	~8* ~7.5*
7-	108	111	-3	135	2.53	1.29	1.36 1	37 1	6 1	124 2.53	10.3 1.29	~8* ~7.5*

*Indicates representative values on different samples.
All initial oxidations and corona processes were at 800°C in dry O_2.
For center region: $F_1 = (1 + 0.12* |I_{cor}|)$, $F_2 = (1+12*|I_{cor}|)$, $F_3 = 6$
For outer region: $F_1=F_2=F_3=1$

Table 7.2: Experimental Corona Cases and Fitted Rate Constants for positive corona films.

ID	X_{in} (nm)	Si type	I_{cor} μA	t min	(B/A) (E-3) μm/h	(B) (E-3) μm^2 /h	F_1 center outer	F_2 center outer	F_3 center outer	$(B/A)_c$ (E-3) center outer	$(B)_c$ (E-3) center outer	Q_f/q (E11) center outer
1+	0	100	+.5	25	1.51	1.29	0.943 1	18.68 13.8	2.5 2.12	26.6 21.5	3.05 2.75	126 162
2+	0	100	+1	25	1.51	1.29	0.893 1	26 19.75	2.5 2.12	35.0 29.8	2.89 2.75	36.4 57
3+	0	100	+8	25	1.51	1.29	0.510 1	71.71 71.71	2.5 2.5	55.7 108	1.67 3.23	74 125
4+	0	100	+3	180	1.51	1.29	0.735 1	44.30 44.30	2.5 2.5	49.3 66.6	2.39 3.23	–
5+	108	111	+3	180	2.53	1.29	0.735 1	44.3 44.3	2.5 2.5	82.8 112	2.39 3.23	–

All initial oxidations and corona processes were at 800°C in dry O_2.
For center region: $F_1=1/(1+0.12*|I_{cor}|)$, $F_2=(1+25*|I_{cor}|^{0.5})$, $F_3=2.5$
For outer region: $F_1 \leq 1$, $F_2 \leq (1+25*|I_{cor}|^{0.5})$, $F_3 \leq 2.5$

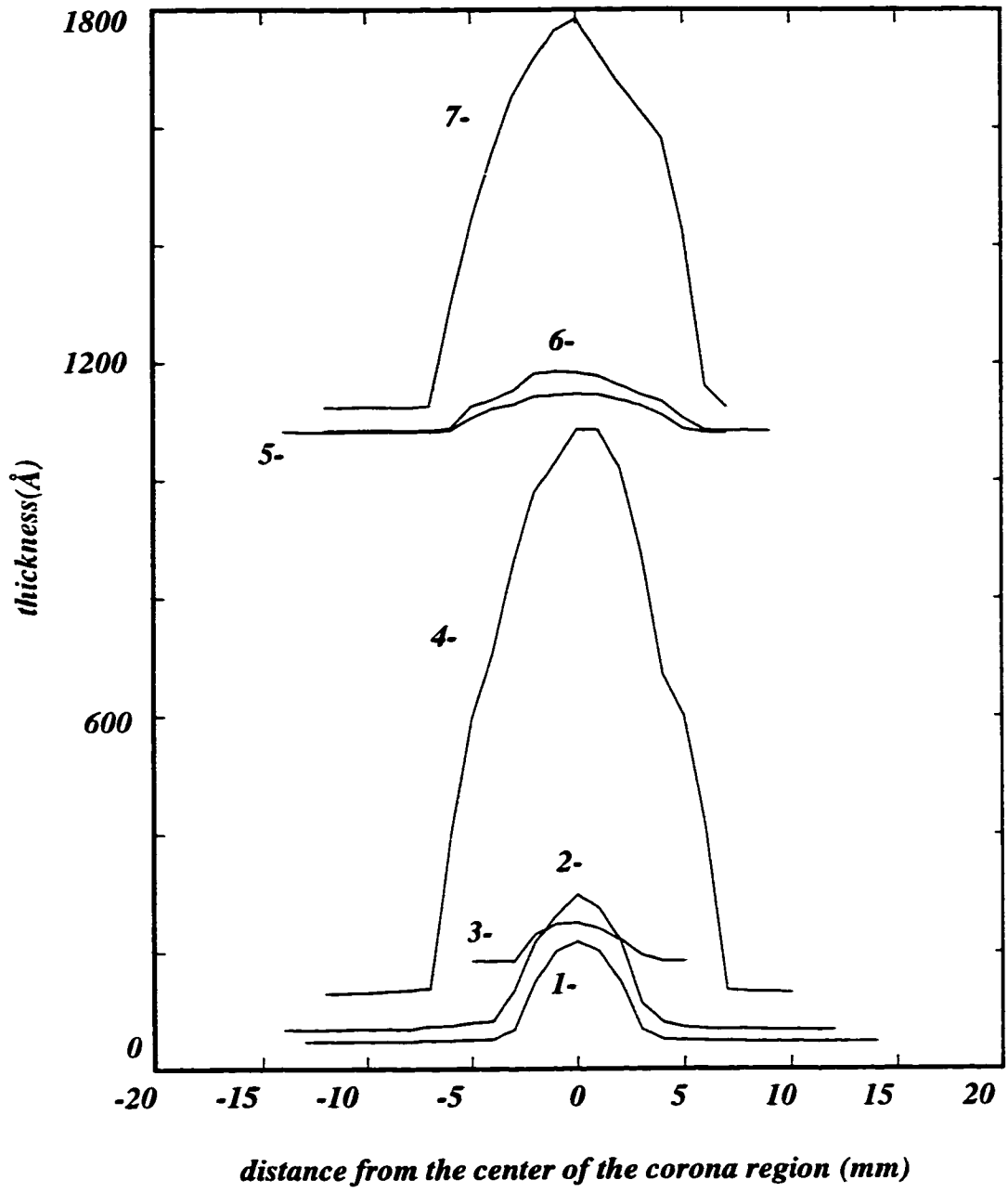

Fig. 7.2: Experimental oxide thickness profiles for negative corona films. See Table 7.1 for curve IDs.

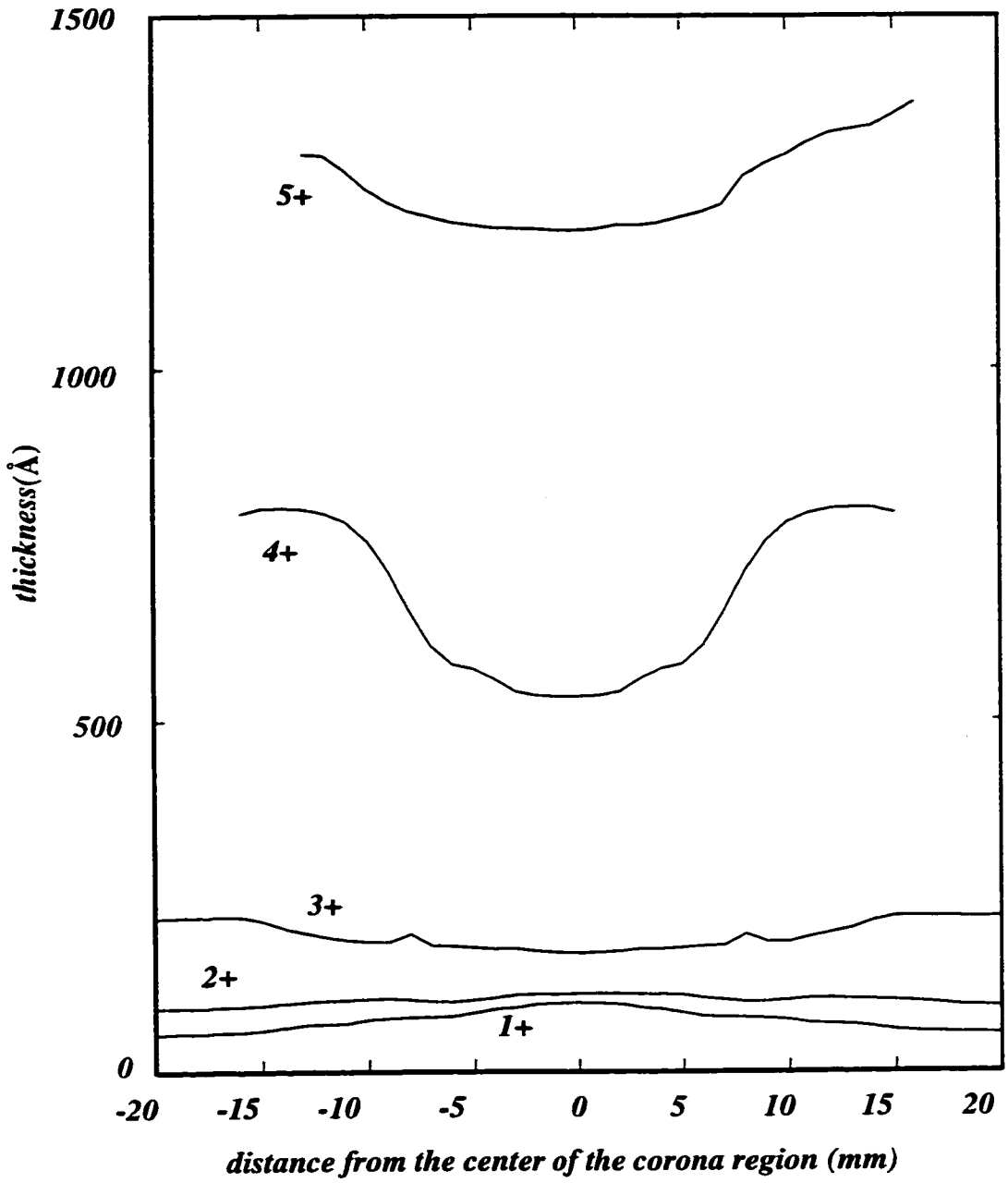

Fig. 7.3: Experimental oxide thickness profiles for positive corona films. See Table 7.2 for curve IDs.

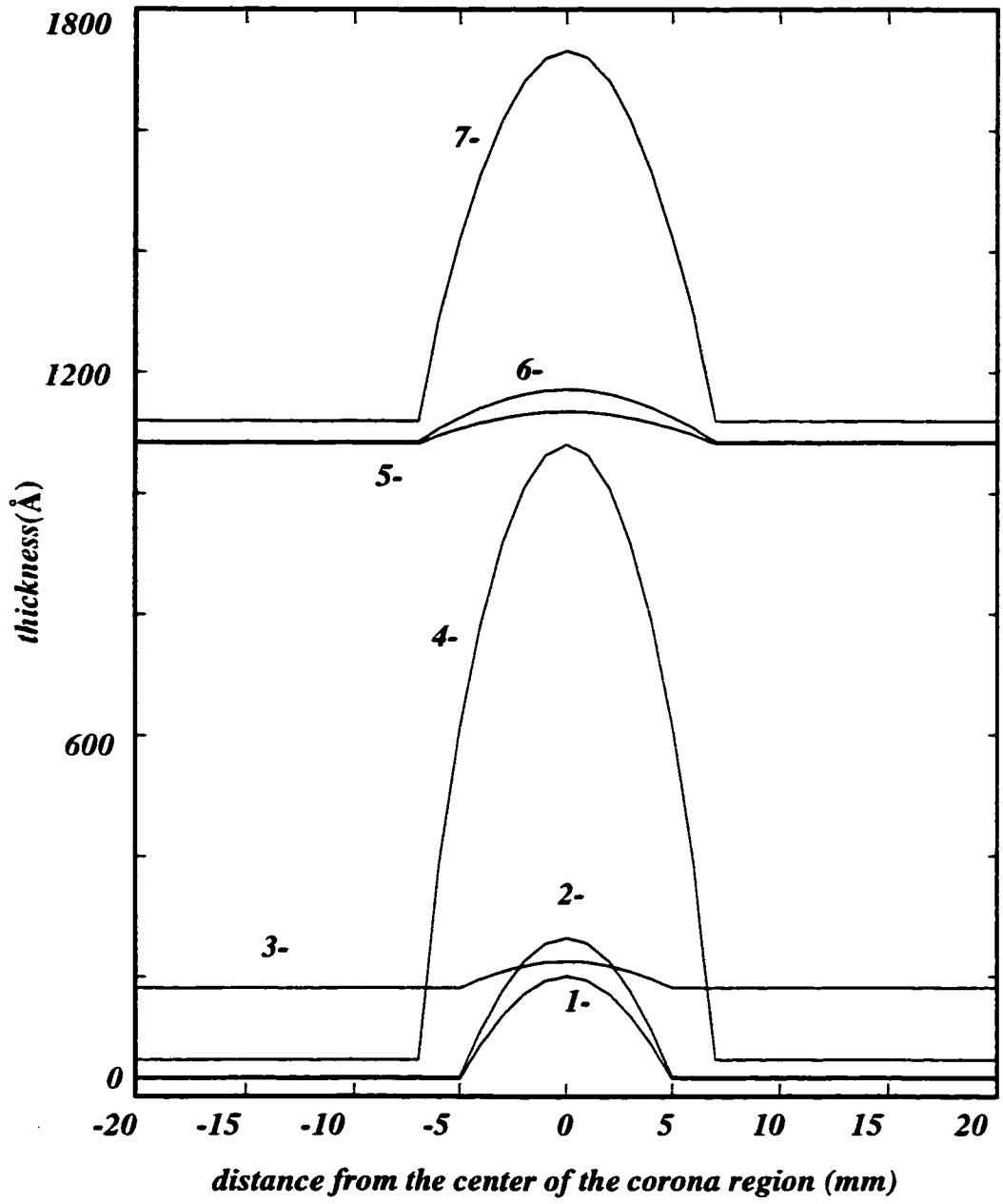

Fig. 7.4: Simulated oxide thickness profiles for negative corona films. See Table 7.1 for curve IDs.

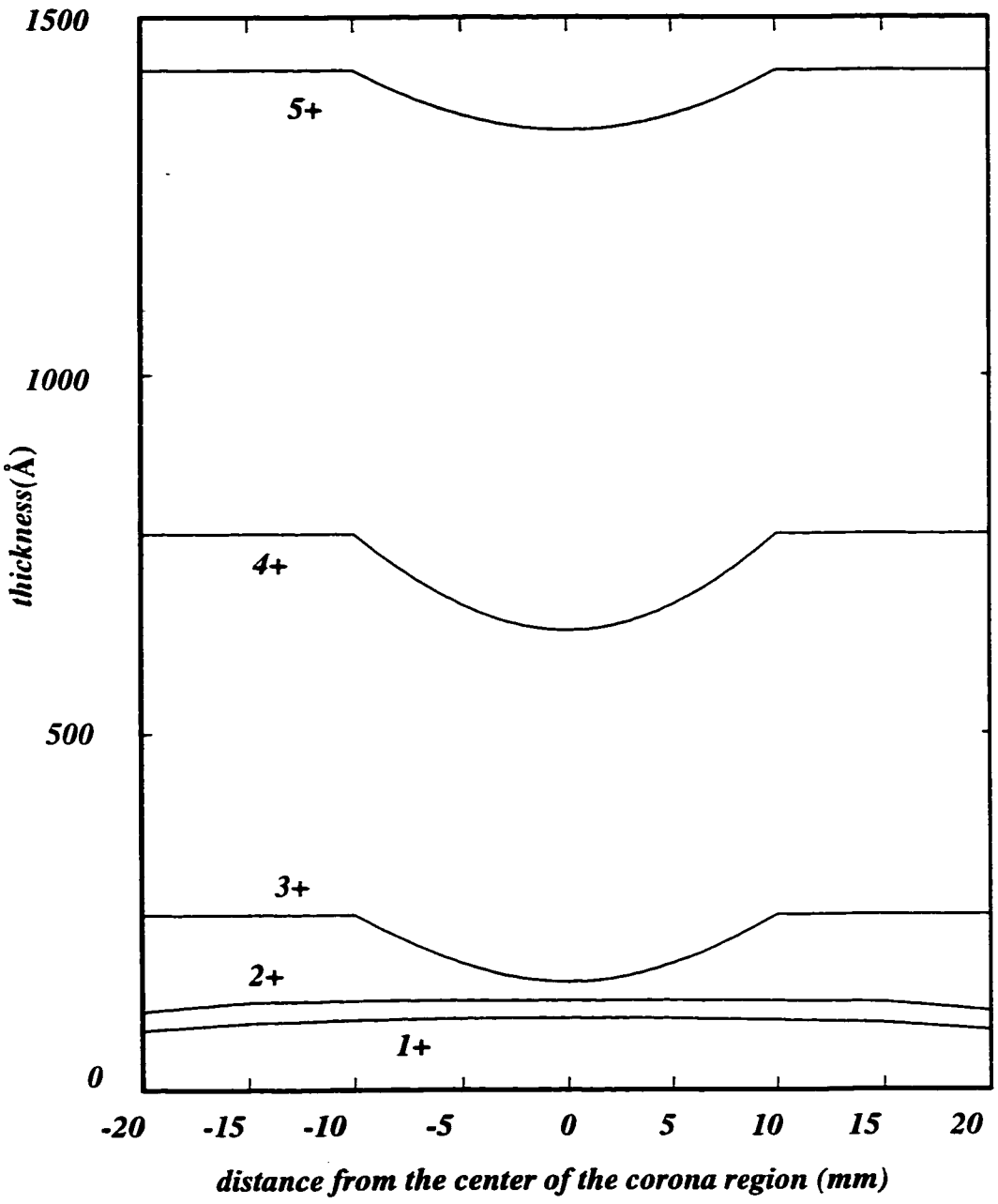

Fig. 7.5: Simulated oxide thickness profiles for positive corona films. See Table 7.2 for curve IDs.

influence, about 5-8mm, corresponding to the circular corona-affected region. (This condition was applied during simulation by giving equal values to HLcn, HLkn, and HLdn in the range of 5-8 mm). In the (+) point case, they vary with different radii of influence across the surface. Factor F_1 has radius ~10mm, corresponding to the center region, while F_2 and F_3 have much larger effective radii, >> 100mm, allowing influence out to the edge of the wafer. An exception to this is found at low thickness on bare silicon, where the radii of influence of F_2 and F_3 need to be ~40mm in order to fit the profiles.

7.3.3 Interpretation Through C*, D, k_i

The Deal-Grove model [33] is a useful starting point for any discussion of silicon oxidation. As shown in Chapter 2, the model describes the increase of oxide thickness, X_{ox} , with time, t, by the equation $X_{ox}^2+AX_{ox}=Bt$. The coefficients $A\cong 2D/k_i$, $B=2C^*D/M_{ox}$, and $B/A\cong C^*k_i/M_{ox}$ were originally defined in terms of an effective oxygen diffusion constant, D, an interface reaction rate constant, k_i, and the molecular oxygen concentration in the oxide at the gas/oxide surface, C*. The parameter M_{ox} is the density of oxygen in the grown film (~4.45×10^{22} cm^{-3}).

Based on a discussion by Mott *et al.* [91], Stoneham *et al.* [92] have proposed the existence of an intermediate "reactive" layer within a few nanometers of the Si/SiO_2 interface that is impermeable to molecular oxygen. This impermeability would then be responsible for the low reaction coefficient, k_i, normally found for the Deal-Grove model. The positive fixed charge in this region creates a field that can draw electrons from the Si substrate by thermionic emission. These electrons could lead to dissociative attachment to the molecular oxygen diffusing toward the impermeable region, forming O and O^-. These could react in the intermediate layer and penetrate to the interface, thus advancing the growth front into the silicon substrate. It has been proposed [93,95] that the arrival of elec-

trons in the oxide is, in fact, the rate limiting step during Si oxidation and these ideas have been advanced to describe the enhanced growth during UV illumination [20,89]. The corona could thus enhance the Deal-Grove reaction coefficient k_i by enhancing the supply of electrons in the intermediate layer. This could reasonably lead to strong dependences of k_{ic} on I_{cor}, such as that given in the fitting factor F_2 for negative corona, $k_{ic} = k_i(1 + 12 |I_{cor}|)$, where k_i is the enhanced interface reaction coefficient.

In order to fit the body of experimental data for negative corona, other enhancements in C_c and D_c would also be necessary, corresponding to the factors F_1 and F_3. Since the (-) corona current drives O^- ions [23,29] in the corona toward the SiO_2 surface, it is plausible to hypothesize that the concentration of oxidant species entering the oxide is enhanced as a function of I_{cor}. Also, since O^- or monatomic O are likely to have an enhanced diffusion constant, the factor F_3 could reasonably be substantially greater than 1 (e.g. = 6, as obtained in the simulation).

It should be noted that the network mixing during (-) corona, reported in O^{18} tracer experiments in Ref. [29], renders it unlikely that the enhancement in B_c is due to simple enhanced diffusion of O_2 molecules through interstitial sites in the SiO_2 network. Rather, the possibility of oxidation due to two parallel oxidant fluxes[73], such as O_2 and monatomic O or lattice vacancies [73], is supported here.

While in (-) corona the electrons could be supplied by current flow from the surface toward the Si/SiO_2 interface, in (+) corona, the emission of electrons from the Si substrate would be aided by the applied field. This would again lead to enhanced k_{ic}, possibly with a different dependence, such as $k_{ic} = k_i (1 + 25 |I_{cor}|^{0.5})$.

However, within the framework of the Deal-Grove variables, it would be impossible to model the (+) corona profiles without assuming that this enhancement in k_{ic} is felt over a broader area out to the edges of the treated wafer. An enhancement in D_c over the broad

area is also necessary to fit at higher thicknesses. Further, it would be impossible to model the (+) corona profiles without assuming a substantial reduction in C_c^* in the center region.

7.3.4 Alternative Linear-Parabolic Interpretation

A linear-parabolic formalism can also be interpreted in terms of an ionic mechanism. Peeters and Li [74] developed a theory for plasma anodization, describing the growth of the oxide film in terms of the subsurface O^- number density, at the oxide/ambient interface, C_i, the oxygen ion mobility, μ, a loss coefficient, k, which describes the loss of the ions as they traverse through the oxide from the plasma-oxide interface, and the electric field, E, in the oxide film. The variation of thickness of the oxide film with time is given by $\beta t=\exp(X_{ox}/\alpha)-1$, where $\alpha=\mu E/k$, $\beta=\gamma C_i k/M_{ox}$, and γ is the probability that an oxygen atom reaching the Si/SiO_2 interface will react. An estimate of $\mu/k=3.78\times10^{-11}$ cm^2/V at 800°C can be obtained [75] from the data of Vuillermoz *et al.* [76]. For $E=5\times10^6$ V/cm, α will be equal to 1.9 μm . For our corona-processed films $X_{ox}<<\alpha$ so that exponential equation above can be expanded in a power series in X_{ox}/μ. Retaining the first three terms in the expansion and rearranging gives $X_{ox}^2+AX_{ox}=Bt$, where $A=2\mu E/k$, $B=2\gamma C_i\mu^2E^2/kM_{ox}$, and $B/A=\gamma C_i\mu E/M_{ox}$. This is the same as the Deal-Grove equation and the correspondence with the Deal-Grove model is complete if D is replaced by $\gamma\mu^2E^2/k$ and k_i is replaced by $\gamma\mu E$. Peeters and Li assume that $\gamma\sim1$, in accordance with Mott [91], who proposed that atomic oxygen species have a very high probability of reacting in or passing through the intermediate layer. The Deal-Grove reaction coefficient, k_i would thus be replaced in the Peeters and Li model by the oxygen ion velocity ($v=\mu E$), while the diffusion constant would be replaced by a quantity involving the ion velocity and its loss coef-

ficient ($D = v^2/k$). The correspondence between the parameters in the two models is presented in Table 7.3, along with the dependencies on needle current I_{cor} in the negative corona case.

Table 7.3: Model Parameter Correspondences.

Deal-Grove Parameter [33]	Peeters and Li Parameter [74]	Current Dependence
C^*	Ci	$F_1=(1+0.12*\|I_{cor}\|)$
k_i	$\gamma\mu E$	$F_2=(1+12*\|I_{cor}\|)$
D	$\gamma\mu^2E^2/k$	$F_3=6$

This model supports the basic hypothesis that the linear-parabolic formalism used in our simulation can apply to the movement of ionic species instead of simply O_2 molecules. However, the independence of F_3 with I_{cor} would seem to be problematic in this model. In order for F_2 and F_3 to correspond properly, the loss coefficient, k, must vary with I_{cor} in the same way that $(\gamma\mu^2E^2)$ varies with I_{cor}.

However, the model [74] does not treat the cathodic plasma case, and cannot explain the enhanced growth which is observed in positive corona.

7.3.5 Electrochemical Interpretation

It has been proposed that oxygen ions, rather than oxygen molecules, are the species responsible for transport through the oxide even for thermal oxidation. As was described in Chapter 2, Wolters *et al.* [34] suggest that these oxygen ions (O^{2-} or O^-) are in equilibrium with the electrons and oxygen molecules in the oxide film. The ions diffuse through the bulk against the field generated by the charge separation caused by their drift. The low interface reaction rate is then a result of the fields opposing the ions responsible for oxida-

tion, particularly the high field in the layer near the interface where positive fixed charge resides. This leads to a power-parabolic law (instead of a linear-parabolic law) for the oxide growth-rate.

Although the model remains controversial for silicon oxidation, it could potentially be useful in explaining the enhancements observed during both positive and negative corona oxidation. The equations as developed for thermal oxidation in Ref. [34], and shown in Eq.(2.17), could be modified taking into account the voltage drop across the oxide and the electron currents through the oxide caused by the corona. Wagner's theory [34,35] on metal oxidation, used by Wolters *et al.* [34] to model standard thermal oxidation can be extended to handle a flux of ions such as driven by the corona:

$$Flux_{ion} = \frac{-(\sigma_e^{-1} + \sigma_{ion}^{-1})^{-1}}{8q^2} \frac{d\mu_{o2}}{dX} + \frac{\sigma_{ion} I_{cor}}{2|q|\,(\sigma_e + \sigma_{ion})} \tag{7.1}$$

where σ_e is the electronic conductivity, σ_{ion} is the ionic conductivity, and μ_{o2} is the thermodynamic potential of O_2 in the Si/SiO_2 oxidation system, which depends critically on the oxygen concentration. The hopping model of Verwey [77] can be used to calculate a field-dependent σ_{ion}.

This development would suggest that the corona, through the injection of electrons into the oxide, can result in an increase in the concentration of reactive species (ions) responsible for oxidation. Phenomenologically, in negative corona, this can be treated by postulating that the corona results in an increased concentration of reactant C* in the Deal-Grove formalism. In positive corona, on the other hand, this concentration would have to be decreased, in order to account for the less-enhanced rate in the center region. In order

for the ion flux to be enhanced for both positive and negative values of I_{cor}, other parameters of the equation (mostly σ_{ion}), must be enhanced by the corona process.

A highly attractive feature of the electrochemical model [33] is its inherent consideration of fixed oxide charge located at or near to the Si/SiO_2 interface. Flat-band voltage shifts in C-V measurements indicate that there is a significant positive charge, Q_f, in all oxides. For thermal oxidation it is estimated that Q_f is located at a position X_Q within 4 nm of the Si/SiO_2 interface, in a region where up to 10^{15} non-stoichiometric Si states have been shown to exist [78]. These states can potentially act as positive charge sites. It is likely that the charge is also close to the interface for the corona-processed oxides so that for thick films $X_Q/X_{ox}<<1$ and $(X_{ox}-X_Q)/X_{ox}\sim 1$. By Gauss' law the field, E_1 , between the fixed charge and Si/SiO_2 interface, and the field, E_2, between the fixed charge and SiO_2/gas interface are given in terms of the oxide thickness X_{ox} and surface potential V_{ox} by [34]:

$$E_1 = E_{ox} + \frac{Q_f}{\varepsilon}\frac{(X_{ox}-X_Q)}{X_{ox}} \cong E_{ox} + \frac{Q_f}{\varepsilon} \tag{7.2}$$

$$E_2 = E_{ox} - \frac{Q_f}{\varepsilon}\frac{X_Q}{X_{ox}} \cong E_{ox} \tag{7.3}$$

with $E_{ox}=V_{ox}/X_{ox}$. The value of fixed charge determined from C-V measurements represents a lower-bound on Q_f since it is likely that some of the fixed charge will anneal out during cool-down from the growth temperature.

For negative corona E_{ox} is negative and Q_f is positive so that $|E_2|>|E_1|$. If $Q_f/q=N_f > \sim 7\times10^{11}$ cm^{-2}(see Tables 7.1 and 7.2) is taken for the central region of the negative

corona, this leads to values of $Q_f/\varepsilon > 3.3\times10^5$ V/cm. This would make the contribution of the fixed charge to the field small by Eqs. (7.2) and (7.3). However, the true Q_f is not known during growth. If Q_f is large enough, E_1 could become small or even positive and the flow of ions through the region near the interface could become limited by diffusion.

For the central region of a positive corona-treated sample, a representative value of $Q_f/q=N_f > \sim 7\times10^{12}$ cm^{-2} so that $Q_f/\varepsilon > 3.3\ 10^6$ V/cm. In the outer region Q_f/ε can be a factor of 2 higher. The field in region 1 is large and opposes the drift of positive ions. However, if Q_f during growth is large enough, the approximation in Eq.(7.3) may not be valid and E_2 may in fact become small allowing a negative ion diffusion mechanism to become operative. For the high fields generated by the fixed charge in region 1 tunnelling may also be an important source of electrons. The lower fixed charge observed in the central corona region as compared to that in the outer region would lead to a smaller field, lower electron injection, lower dissociative attachment rates in the intermediate layer, and lower growth rate in the central region as is observed.

7.4 Summary

Several experimental profiles of both positive- and negative-point corona discharge oxidation processes (anodic and cathodic, respectively) are simulated using linear-parabolic rate constants, modified to account for the corona current. Three enhancement factors are required for a reasonable fit. The interface reaction constant may be enhanced in both anodic and cathodic cases due to movement or emission of electrons. The effective oxidant concentration under the corona needle is hypothesized to be increased in the anodic case, and decreased in the cathodic case. The effective diffusion constant must be enhanced, but does not need to vary with corona current. Perhaps is corresponds to a different diffusing species. For a variety of reasons, other models may be required to explain

all the phenomena for both polarities.

For the negative corona case, a field-aided ionic transport model [74] is further considered, which leads neatly to a linear-parabolic formalism. However, the correspondence between the physical quantities and the three simulation parameters mentioned above, is problematic, and the model is applicable only to the anodic case.

An electrochemical model [34] has been considered since it takes account of the fixed charge in the oxides, which can be very large for the positive-corona case. To fully evaluate the applicability of this model, it needs to be extended to account for the change in ionic conductivity with surface potential V_{ox} which changes during corona oxidation to maintain a constant current through the oxide.

7.5 Chapter 7 Contributions

- A simulation program was designed to model the oxidation enhancements observed in both anodic and cathodic corona processes. Based on a linear- parabolic formalism, three enhancement factors were used to modify the linear and parabolic rate constants. Spatial variations were accounted for by different radii of influence for each of the three factors. The three factors were designed to vary in different ways with applied corona current.
- Good fits to the model were obtained for negative corona. Satisfactory fits to the model were obtained for positive corona.
- The fits to the linear-parabolic model were interpreted in terms of the common physical oxidation quantities, C*, D, and K_i. Based on this interpretation, it was found that:

  — in negative corona, there is an enhancement in oxidant concentration in the oxide at the gas/oxide surface. In positive corona there is a reduction in this parameter.

  — In both negative and positive corona processes, there is in enhancement in the Si/SiO_2 interface reaction factor.

  — In both negative and positive corona processes, there is an enhancement in the oxidant diffusion constant.

  - The physical meanings of these enhancements were interpreted in light of various prior insights from several different oxidation researchers.

CHAPTER 8

Summary of Contributions, and Suggestions for Future Work

8.1 Overview

This experimental investigation has examined different aspects of oxide films grown or treated by the corona procedure. Four lines of investigations are included in this work: 1) Study of the electrical characteristics of the films (Chapters 3 and 5) ; 2) Study of the structure of the films (Chapter 6) ; 3) Investigation toward creation of films on broader areas of the wafer (Chapter 4); and finally, 4) Study of the kinetics of the growth (Chapter 7).

Through electrical characterization of the negative corona films, it was found that the films have characteristics comparable to those of standard thermal oxide films. Also, by using a two-step corona procedure the distinct behaviour of the films at their boundary with control oxide area was revealed. C-V tests on positive corona films showed that the positive corona process creates films with high oxide charges.

FTIR analysis of the films gave insight into the structure of the corona films. It was found that the expected relation between refractive index of the films and frequency and FWHM of AS vibration spectrum, is not valid for negative corona films. It was suggested that the negative corona films have a different structure from that of thermal oxide film. For positive corona films the behaviour was found similar to that of thermal oxide films.

Preliminary work to produce uniform negative corona films in larger areas of the wafer was presented in this work. The strategy and procedures involved in using a grid of

points fabricated out of a piece of Si wafer (instead of the platinum needle) was described. Experimental results of the new structure revealed some important features of the technique.

Using a simulation program the oxidation rates in both positive and negative corona processes were modeled based on a linear-parabolic equation. Based on the results, the mechanisms involved in the processes were discussed.

Below are listed the primary contributions of this dissertation:

8.2 Contributions

1- Study of the Electrical Characteristics of the Corona Films

Refer to Chapter 3:

- The trends found by previous researchers in negative-point corona processing of thicker oxides were confirmed for thinner oxides:
  - Q_f was found to be in the level of ~mid-$10^{11}/cm^2$. This is close to that previously found for thick corona films, and to that of thermally grown films.
  - D_{it} was found to be in the level of ~mid-$10^{10}/cm^2eV$. This is also comparable to those of thick corona films, and standard thermally grown films.
  - the presence of edge phenomena seen previously in the Q_f and D_{it} results of thicker corona films, was also seen in thin corona films.
- Preliminary oxide reliability tests show that the negative-corona oxide is more resistant to creation of oxide defects. Also, ΔQ_f data indicates that bulk oxide in the center region of the corona film, may have better quality compared to that in surrounding regions. The trends of charge creation during electrical stress are comparable to those of standard thermally grown films.

- Ramp voltage tests showed that the V_{bd} are slightly higher for corona treated oxides compared to thermally-grown films.
- Edge phenomena were found in Q_{bd} results. There were low values of Q_{bd} at the boundary regions of the corona oxides.
- Overlapped corona treatments showed that if a boundary region of a corona film is located in the area of a second subsequent corona process, its properties recovered for satisfactory Q_f and breakdown strength. Also if a boundary region of a corona film is located in the area of a previously grown corona film, its Q_f and breakdown strength are not degraded.
- Most of the results are consistent with a structural difference between thermally grown and negative-corona grown films.

Refer to Chapter 5:

- The trends in positive-point corona-oxidation, first discovered by Modlin *et al* [22], were confirmed:
  - The thickness profile shape in (+) corona is wider compared to that of (-) corona, and appears to be limited by wafer size.
  - The thickness profile in (+) corona is not as regular as it is in (-) corona; for thinner films the highest thicknesses are in the center region, while for thicker films the highest thicknesses are in the outside regions surrounding the center.
  - For a given amount of time and current, the maximum thickness enhancement of a (+) corona film is lower than the center region enhancement of a (-) corona film.
- It was found that positive corona-treated films have similar thickness profiles of thick positive corona films (the center region has lower thickness compared to its surrounding regions).

- Similarly to negative corona, positive-point corona treatments of low-temperature thermally-grown SiO_2 films, cause structural relaxation phenomena, as measured by refractive index changes. However, the refractive index of (+) corona treated films is not as low as that of (-) corona-treated films.
- Q_f and D_{it} results showed that the electrical quality of the positive corona films is much lower than standard thermally grown films grown at similar temperature.
- The results of positive corona films are consistent with some other cathodic plasma processes in terms of very poor oxide electrical properties, but quite different in terms of stopping of the film growth seen in the cathodic plasma at certain thicknesses of the film.

2- Study of the Structure of the Corona Films

Refer to Chapter 6:

- FTIR was used to examine and compare both (+) and (-) point-corona-processed cases with each-other and with thermally-grown controls.
- By an etch-back experiment with FTIR measurements after each etch step, the structure of the oxide at different distances from the Si/SiO_2 interface was examined.
- Within the limits of the technique used in this work, it was found that the corona films are relatively homogeneous.
- It was found that despite having the refractive index equal to that of high temperature grown oxide, negative corona films have AS mode frequency close to that of low temperature thermally grown oxide.
- It was found that positive corona films have AS mode frequency close to that of high temperature thermally grown oxide.

- The results suggest that negative corona films have a different structure from that of thermal oxide films.
- The results support the previously suggested hypothesis in Chapter 3 that the distinct behaviour of the oxide films at the boundary regions between negative corona and control regions could be a result of a structural mismatch.

3- Investigation Toward Creation of Uniform Films on Broader Area of the Wafer

Refer to Chapter 4:

- In the interests of growing more-uniform negative-corona SiO_2 films on broader areas of silicon wafers, experiments using multi-point or multi-needle cathode structures were conducted.
- Micromachined grid-of-points structures were fabricated and used as cathodes for corona-discharge oxidations, in two different configurations.
- The oxidation rate enhancements were found to be non-uniform, leading to several other experiments to discover the nature of the causes for the non-uniformity. Two other cathode structures were examined: one made from 3 Pt needles, and another made by micromachining 12 long needles from a piece of silicon.
- Difficulties were found to be likely due to two main issues: (a) the great sensitivity of the corona discharge to the point-to-plane distance, which would thus require that any two points have exactly the same distance to the substrate; (b) the tendency of the electric current carried in the corona discharge to seek the most divergent paths available, thus leading to the thickness profiles being enhanced around the edges of several cathode geometries.
- It was found that the grid-of points method was more effective in oxidizing areas

of bare Si opened through a previously-grown thick oxide layer. The thick oxide pattern may act as a shield, guiding the corona discharge current to the desired areas.

- Regarding the relationship between the number of charge carriers passing though the film due to the corona current and the number of oxygen atoms incorporated into the film, it was found that using the grid-of-points, much fewer charge carriers (approx 10 times fewer) are required.

4- Study of the Kinetics of the Growth

Refer to Chapter 7:

- A simulation program was designed to model the oxidation enhancements observed in both anodic and cathodic corona processes. Based on a linear- parabolic formalism, three enhancement factors were used to modify the linear and parabolic rate constants. Spatial variations were accounted for by different radii of influence for each of the three factors. The three factors were designed to vary in different ways with applied corona current.
- Good fits to the model were obtained for negative corona. Satisfactory fits to the model were obtained for positive corona.
- The fits to the linear-parabolic model were interpreted in terms of the common physical oxidation quantities, C*, D, and K_i. Based on this interpretation, it was found that:
  - In negative corona, there is an enhancement in oxidant concentration in the oxide at the gas/oxide surface. In positive corona there is a reduction in this parameter.
  - In both negative and positive corona processes, there is an enhancement in

the Si/SiO2 interface reaction factor.

– In both negative and positive corona processes, there is an enhancement in the oxidant diffusion constant.

• The physical meanings of these enhancements were interpreted in light of various prior insights from several different oxidation researchers.

8.3 Suggestions for Future Work

This work has revealed some related aspects of the corona films. However, still there are many other aspects that must be studied in detail before reaching a point at which the process could be considered as a candidate in the line of VLSI fabrication processes. The list of the necessary work would be a very long list, and prioritizing it would also be a difficult task. Nevertheless, this author would like to offer some suggestions for future work based on his observations during the course of this research:

- Continuing the work that has been presented in Chapter 4. Using some electrically separated cathode structure, together with the grid-wafer structure introduced in that chapter would be a step to improve the uniformity of the film. Also, an apparatus should be attempted in which a flat quartz piece with some open windows was inserted between cathode and anode.

- Fabrication of MOS transistors by using corona oxidation to grow gate oxide. Through this some important measurement techniques such as hot-carrier stress, and carrier-separation can be applied on corona films.

- Using polysilicon instead of metal in fabricating MOS capacitors on negative corona films followed with electrical characterization of the films to study the effect of gate material on film characteristics.

- Even though the preliminary results of this work show that the positive corona films have poor electrical properties, a low etch rate of the film indicates a potential use of the films as a field oxide or as a temporary layer during a fabrication process. In that respect, detailed knowledge of the characteristics of the film would be necessary before introducing the process into VLSI technology.

- The effects of corona procedures on the substrate and on dopant profiles is also an important issue.

References

[1] E. H. Nicollian, J. R. Brews, *MOS Physics and Technology*. New York: Wiley-Inter Science, 1982.

[2] S. M. Sze , *Physics of Semiconductor Devices*. New York: Wiley, 1969.

[3] C. R. Helms, B. E. Deal, *The Physics and Chemistry of SiO_2 and Si/SiO_2 Interface*. New York: Plenum Press, 1988.

[4] C. R. Helms, B. E. Deal, *The Physics and Chemistry of SiO_2 and Si/SiO_2 Interface-2*. New York: Plenum Press, 1993.

[5] H. Z. Massoud, E. H. Poindexter, C. R. Helms, *The Physics and Chemistry of SiO_2 and Si/SiO_2 Interface*-3. Pennington, N.J.: The Electrochemical Society, Inc., 1996.

[6] A. Philipossian, B. Doyle, K. Van Wormer, " Nitrogen Incorporation in Gate Dielectrics: A Correlation Between Auger Electron Spectroscopy and Surface Charge Analysis Techniques, "*J. Electrochem. Soc.*, vol. 142, no. 10, pp. L171-L172, 1995.

[7] R. Wrixon, A. Twomey, P.O. Sullivan, A. Mathewson, " Enhanced Thickness Uniformity and Electrical Performance of Ultrathin Dielectrics Grown by RTP Using Various N_2O-oxynitridation Processes, " *J. Electrochem. Soc.* , vol. 142, no. 8, pp. 2738-2742, 1995.

[8] M. F. Ceiler, Jr., P.A. Kohl, S.A. Bidstrup, " Plasma-Enhanced Chemical Vapor Deposition of Silicon Dioxide, " *J. Electrochem. Soc.* , vol.142, no.6, pp. 2067-2071, 1995.

[9] G. Eftekhari, " Effects of Oxide Thickness and Oxidation Parameters on the Electrical Characteristics of Thin Oxides Grown by Rapid Thermal Oxidation of Si in N_2O, " *J. Electrochem. Soc.*, vol. 141, no. 11, pp. 3222-3225, 1994.

[10] K. Kim, Y. H. Lee, M. S. Sun, C. J. Youn, K. B. Lee, H. J. Lee, " Thermal Oxidation of Silicon in N_2O Ambients, " *J. Electrochem. Soc.*, vol. 143, no. 10, pp. 3372-3376, 1996.

[11] C. F. Yen, C. L. Chen, " Controlling Fluorine Concentration and Thermal Anneal-

ing Effect on Liquid-Phase Deposited $SiO_{2-x}F_x$ Films, " *J. Electrochem. Soc.*, vol. 142, no. 10, pp. 3579-3583, 1995.

[12] K.L. Wang, S.G. Thomas, M.O. M.O.Tanner, " SiGe Band Engineering for MOS, CMOS and Quantum Effect Devices, " *J. Materials Sci.: Material in Electronics*, vol. 6, pp. 311-324, 1995.

[13] B.S. Meyerson, " UHV/CVD Growth of Si and Si:Ge Alloys: Chemistry, Physics, and Device Applications, " *Proceedings of the IEEE*, vol. 80, no. 10, pp. 1592-1608, 1992.

[14] V.Q. Ho and T. Sugano, " Selective Anodic Oxidation of Silicon in Oxygen Plasma, "*IEEE Trans. Electron Devices, vol.* ED-27, no. 8, pp. 1436-1443, 1980.

[15] K.J. Barlow, S. Taylor, W. Eccleston, and A. Kiermasz, " The Low-Temperature Anodization of Silicon in a Gaseous Plasma, " *IEEE Tran Electron Devices*, vol. ED-36, no. 7, pp. 1279-1285, 1989.

[16] S. Gourrier, M. Bacal, " Review of Oxide Formation in a Plasma, " *Plasma Chemistry and Plasma Processing*, vol. 1, no. 3, pp. 217-232, 1981.

[17] H. Wong, T. F. Hung, Y. K. Chan, and M. C. Poon, " Effects of Electric Field on the Oxide Growth with Plasma Anodization of Silicon, " *SPIE*, vol. 2364, pp.114-119, 1994.

[18] D.A.Carl, D.W.Hess, M.A.Lieberman, T.D.Nguyen, and R.Gronsky, " Effects of DC Bias on the Kinetics and Electrical Properties of Silicon Dioxide Grown in an Electron Cyclotron Resonance Plasma, " *J. Appl. Phys.*, vol. 70, no. 6, pp. 3301-3313, 1991.

[19] S. Taylor, W. Eccleston, and P. Watkinson, " Advances in Electrical Properties of Plasma-Grown Oxides of Silicon, " *Electronics Letters*, vol. 23, no. 14 , pp. 732-733, 1987.

[20] A. Dolique and A.H. Reader, " Low-Temperature Voltage Enhanced UV-Assisted Oxidation of Silicon, " *J. Non-Crystal. Solids*, vol. 187, pp. 29-34, 1995.

[21] J. F. O'Hanlon, " Gas Discharge Anodization, " *Oxides and oxides Films*, vol. 5,

Edited by A.K. Vijh, pp. 105- 161, 1977.

[22] D. N. Modlin, *Effects of Electric Fields and Oxygen Ion Beams on Silicon Oxidation Kinetics*. Ph.D. Thesis, Stanford University, Stanford, CA, 1983.

[23] D. N. Modlin, W. A. Tiller, " Effects of Corona-Discharge Induced Oxygen Ion Beams and Electric Fields on Silicon Oxidation Kinetics, " *J. Electrochem. Soc.*, vol. 132, no. 5, pp. 1163-1168, 1985.

[24] L. M. Landsberger, W. A. Tiller," Stress Relaxation Technique for Thermally Grown SiO_2, " *Appl. Phys. Lett.*, vol. 49, no. 3, pp. 143-145, 1986.

[25] L. M. Landsberger, W. A. Tiller, " Relaxation Index, Relaxation Times and Viscoelastic Model in Dry-Grown SiO_2 Films on Si, " *Appl. Phys. Lett.*, vol. 51, no.18, pp. 1416-1418, 1987.

[26] L. M. Landsberger, *Structural Relaxation Effects in Dry Thermally-Grown Silcon Dioxide Films on Silicon*. Ph.D. Thesis, Stanford University, Stanford, CA, 1988.

[27] L. M. Landsberger, D. B. Kao, W. A. Tiller, " Conformal Two-Dimensional SiO_2 Layers on Silicon Grown by Low Temperature Corona Discharge, " *J. Electrochem. Soc.*, vol. 135, no. 7, pp. 1766-1771, 1988.

[28] L. M. Landsberger, W. A. Tiller, " Two-Step Oxidation Experiments to Determine Structural and Thermal History Effects in Thermally-Grown SiO_2 Films on Si, " *J. Electrochem. Soc.*, vol. 137, no. 9, pp. 2825-2836, 1990.

[29] L.M.Landsberger and W.A.Tiller, " Stress Relaxation in SiO_2 Films on Silicon by a Negative Point Oxygen Corona Discharge, " *J. Electrochem. Soc.*, vol. 139, no.1, pp. 218-227, 1992.

[30] L.M.Landsberger, " Mechanisms of Oxidation Rate Enhancement in Negative-Point Oxygen Corona Discharge Processing of SiO_2 Films on Si, " *The Physics and Chemistry of SiO_2 and the Si-SiO_2 Interface 2*, Edited by C. R. Helms and B. E. Deal, Plenum Press, New York, pp. 63-70, 1993.

[31] M.R.Madani, P.K. Ajmera, " Characterization of Silicon Oxide Films Grown at Room Temperature by Point-to-Plane Corona Discharge, " *J. Electron. Mat.*, vol.22,

no.9, pp. 1147-1152, 1993.

[32] J.R. Ligenza, " Silicon Oxidation in an Oxygen Plasma Excited by Microwaves, " *J. Appl. Phys.*, vol. 36, no. 9, pp. 2703- 2707, 1965.

[33] B.E.Deal and A.S.Grove, " General Relationship for the Thermal Oxidation of Silicon, " *J. Appl. Phys.*, vol. 36, no. 12, pp. 3770-3778, 1965.

[34] D.R.Wolters and A.T.A.Zegers-van-Duijnhoven, " Silicon Oxidation and Fixed Oxide Charges, " *J.Electrochem. Soc.*, vol. 139, no. 1, pp. 241-249, 1992.

[35] C. Wagner, " Beitrag Zur Theorie des Anlaufvorgangs, " *Z. phys. chem.* B, vol. 21, pp. 25-41, 1933.

[36] S. Taylor, K. J. Barlow, W. Eccleston, and A. Kiermasz, " Oxidation Systems for Growth of Thin Oxides at Low Temperature, " *Electronics Letters*, vol. 23, no. 7, pp. 309-310, 1987.

[37] D. N. Modlin, W. A. Tiller, " Apparatus for Producing controlled Positive or Negative Corona Discharge Semiconductor Material Processing, " *Rev. Sci. Instrum.*, vol. 55, no. 9, pp. 1433 -1441, 1984.

[38] S. M. Sayedi, L. M. Landsberger, and M. Kahrizi, " Electrical Characterization of Thin SiO_2 Films Created by Negative-Point Oxygen Corona Discharge Processing, " presented in *Canadian Conf. on Elec. and Comp. Engineering*, T. J. Malkinson, Editor, pp. 64-67, Calgary, Canada, May, 1996.

[39] S.M. Sayedi, L.M. Landsberger, M. Kahrizi, S. Belkouch, D. Landheer, " Electrical Characterization of the Thin Anodic Corona-Discharge Processed SiO_2 Films on Silicon, " presented in *Electrochemical Society Conference*, Montreal, Canada, May 1997.

[40] D. J. DiMaria, E. Cartier, D. Arnold, " Impact Ionization, Trap Creation, Degradation, and Breakdown in Silicon Dioxide Films on Silicon, " *J. Appl. Phys.* , vol. 73, no. 7, pp. 3367-3384, 1993.

[41] X. -J. Yuan, J. S. Marsland, W. Eccleston, D. Bouvet, J. Mi, M. Dutoit, " Charge Trapping and Interface State Generation in Rapid Thermal Processed Oxide and

Nitrided Oxide MOS Capacitors by Electron Photo Injection From Al Gate and Si Substrate, " *J. Electrochem. Soc.*, vol. 142 , no. 3, pp. 1021-1024, 1995.

[42] E. Rosenbaum, J. C. King, and C. Hu, " Accelerated Testing of SiO_2 Reliability, "*IEEE Trans. Electron Devices*, vol. 43, no. 1, pp. 70-80, 1996.

[43] J. J. Simonne, J. Buxo, *Insulating Films on Semiconductors*. Amsterdam: Elsevier Science Publishers B.V., 1985.

[44] M. W. Hillen, M. M. Heyns, S. K. Haywood, and R. F. De Keersmaecker, " Influence of Charge Build-Up on Breakdown and Wear-Out in Thin SiO_2 Layers on Si, " *Proceeding of First International Conference on Conduction and Breakdown in Solid Dielectrics*, pp. 355-359, Toulouse, France, 1983.

[45] C. Silvestre and J. R. Hauser, " Time Dependent Dielectric Breakdown Measurements on RPECVD and Thermal Oxides, " *J. Electrochem. Soc.*, vol. 142, no. 11, pp. 3881-3889, 1995.

[46] D.R.Wolters and J.J.Van der Schoot, " Breakdown by Charge Injection, " *Insulating Films on Semiconductors*, Edited by J.J. Simonne and J.Buxo, Elsevier Science Publishers B.V., Amsterdam , pp.145-149, 1985.

[47] E. Hasegawa, A. Ishitani, K. Akimoto, M. Tsukiji, and N. Ohta, " SiO_2/Si Interface Structures and Reliability Characteristics, " *J. Electrochem. Soc.*, vol. 142, no. 1, pp. 273-282, 1995.

[48] S. Holland and C. Hu, " Correlation Between Breakdown and Process-Induced positive Charge Trapping in Thin Thermal SiO_2, " *J. Electrochem. Soc.*, vol. 133, no. 8, pp. 1705-1712, 1986.

[49] C. M. Osburn and D. W. Ormond, " Dielectric Breakdown in silicon Dioxide on Silicon I & II, " *J. Electrochem. Soc.*, vol. 119, no. 5, pp. 591-603, 1972.

[50] N. Klein, " Electrical Breakdown in Thin Dielectric Films, " *J. Electrochem. Soc.*, vol. 116, no. 7, pp. 963-972, 1969.

[51] M. W. Hillen, I. S. Darakchiev, and R. F. De keersmaecker, " Influence of Processing Conditions on Breakdown and Charge Build-Up in Thin SiO2 Gate Dielectrics, "

Proceeding of First International Conference on Conduction and Breakdown in Solid Dielectrics, pp. 443-447, Toulouse, France, 1983.

[52] J. F. Verwey and D. R. Wolters, " Breakdown Fields in Thin Oxide Layers, " *Insulating Films on Semiconductors*, Edited by J. J. Simonne and J. Buxo, Elsevier Science Publishers B.V., Amsterdam , pp. 125-132, 1985.

[53] D. R. Wolters, J. J. Van der Schoot, and T. Poorter, " Damage Caused by Charge Injection, " *Insulating Films on Semiconductors*, Edited by J. J. Simonne and J. Buxo, Elsevier Science Publishers B.V., Amsterdam , pp. 256-260, 1983.

[54] J. J. Van der Schoot and D. R. Wolters, " Current Induced Dielectric Breakdown, "*Insulating Films on Semiconductors*, Edited by J. J. Simonne and J. Buxo, Elsevier Science Publishers B.V., Amsterdam, pp. 270-273, 1983.

[55] S.M. Sayedi, D. Landheer, L.M. Landsberger, M. Kahrizi, " Fourier-Transform Infrared Spectroscopy of Corona-Processed Silicon Dioxide Films, " presented in *Electrochemical Society Conference*, Montreal, Canada, May, 1997.

[56] E. Taft and L.Cordes, " Optical Evidence for a Silicon-Silicon Oxide Interlayer, " *J. Electrochem. Soc.*, vol. 126, no.1, pp. 131-134, 1979.

[57] C.T. Kirk, " Quantitative Analysis of the Effect of Disorder-Induced Mode Coupling on Infrared Absorption in Silica, " *Phys. Rev. B*, vol. 38, no. 2, pp. 1255-1273 (1988).

[58] L. Galeener and G. Lucovsky, " Longitudinal Optical Vibrations in Glasses: GeO_2 and SiO_2, " *Phys. Rev. Lett.*, vol. 37, no. 22, pp. 1474-1478, 1976.

[59] P. Lange and W.Windbracke, " Characterization of Thermal and Deposited Thin Oxide Layers by Longitudinal-Transverse Optical Excitation in Fourier Transform IR Transmission Measurements, " *Thin Solid Films*, vol. 174, pp. 159-164, 1989.

[60] A. Goullet, C. Charles, P. Garcia, and G. Turban, " Quantitative Infrared Analysis of the Stretching Peak of SiO_2 Films Deposited from Tetraethoxysilane Plasmas, " *J. Appl. Phys.*, vol. 74, no. 11, pp. 6876-6882, 1993.

[61] I.W. Boyd, " Deconvolution of the Infrared Absorption Peak of the Vibrational

Stretching Mode of Silicon Dioxide: Evidence for Structural Order?, " *Appl. Phys. Lett.*, vol. 51, no. 6, pp. 418-420, 1987.

[62] C. Martinet and R.A.B. Devine, " Analysis of the Vibrational Mode Spectra of Amorphous SiO_2 Films, " *J. Appl. Phys.*, vol. 77, no. 9, pp. 4343-4348, 1995.

[63] J.T. Fitch, C.H. Bjorkman, G. Lucovsky, F.H. Pollak, and X. Yin, " Intrinsic Stress and Stress Gradients at the SiO_2/Si Interface in Structures Prepared by Thermal Oxidation of Si and Subjected to Rapid Thermal Annealing, " *J. Vac. Sci. Technol. B* , vol. 7, no. 4, pp. 775-781, 1989.

[64] P.N. Sen and M.F. Thorpe, " Phonons in AX_2 Glasses: From Molecular to Band-Like Modes, " *Phys. Rev. B*, vol. 15, no. 8, pp. 4030-4038, 1977.

[65] F.L. Galeener, " Band Limits and the Vibrational Spectra of Tetrahedral Glasses, " *Phys. Rev. B*, vol. 19, no. 8, pp. 4292-4297, 1979.

[66] J. T. Fitch, S.S. Kim, and G. Lucovsky, " Thermal Stabilization of Device Quality Films Deposited at Low Temperatures, " *J. Vac. Sci. Technol. A*, vol. 8, no. 3, pp. 1871-1877, 1990.

[67] A. S. Grove, *Physics and Technology of Semiconductor Devices*. New York: Wiley, 1967.

[68] W.A. Tiller, " On the Kinetics of the Thermal Oxidation of Silicon, " *J. Electrochem. Soc.*, vol. 127, no. 3, pp. 625-632,1980.

[69] E. A. Irene, " Silicon Oxidation Studies: Some Aspects of the Initial Oxidation Regime, " *J. Electrochem. Soc.*, vol. 125, no. 10, pp. 1708-1714, 1978.

[70] E. A. Irene, " Silicon Oxidation Studies: A Revised Model for Thermal Oxidation, "*J. Appl. Phys.*, vol. 54, no. 9, pp. 5416-5420, 1983.

[71] A. Fargeix, G. Ghibando, G. Kamarinos, " A Revised Analysis of Dry Oxidation of Silicon, " *J. Appl. Phys.*, vol. 54, no. 5, pp. 2878-2880, 1983.

[72] R.L. Mozzi and B.E. Warren, " The Structure of Vitreous Silica, " *J. Appl. Crystallogr.* vol. 2, pp. 164-172, 1969.

[73] C.J. Han and C.R. Helms, " Parallel Oxidation Mechanism for Si oxidation in Dry

O_2, " *J. Electrochem. Soc.*, vol. 134, no. 5, pp. 1297-1302, 1987.

[74] J. Peeters and L. Li, " *A New Model for The Plasma Anodization of Silicon at Constant Current,* " *J. Appl. Phys.* vol. 72, no. 2, pp. 719-724, 1992.

[75] C. Martinet and R.A.B. Devine, " Low-Temperature Oxidation of Si in a Microwave Electron Cyclotron Resonance Excited O_2 Plasma, " *Appl. Phys. Lett.* , vol. 67, no. 23, pp. 3500-3502, 1995.

[76] B. Vuillermoz, A. Straboni, and A. Vareille, " High Frequency Anodization of Silicon, " *Insulating Films on Semiconductors*, Edited by J.F. Verweij and D.R. Wolters, Elsevier, Amsterdam, pp. 234-237, 1983.

[77] E.J.W. Verwey, " Electrolytic Conduction of a Solid Insulator at High Fields, " *Physica* 2, pp. 1059-1062, 1935.

[78] F.J. Grunthaner, M.H. Hecht, P.J. Grunthaner, and N.M. Johnson, " The Localization and Crystallographic Dependence of Si Suboxide Species at the SiO_2/Si Interface, " *J. Appl. Phys.*, vol. 61, no. 2, pp. 629-638, 1987.

[79] S.Taylor, W.Eccleston and K.J.Barlow, " Theory for the Plasma Anodization of Silicon Under Constant Voltage and Constant Current Conditions, " *J. Appl. Phys.*, vol. 64, no. 11, pp. 6515-6522, 1988.

[80] J. Peeters, L. Li, " Oxidation of Silicon in Plasma Afterglows: New Model of Oxide Growth Including Recombination of Diffusing O Atoms, " *J. Appl. Phys.*, vol. 73, no. 5, pp. 2477-2485, 1993.

[81] L. Li and J.Peeters, " A Model for Plasma Anodization of silicon at Constant Voltage, " *J. Appl. Phys.*, vol. 74, no. 1, pp. 639-644, 1993.

[82] J. L. Moruzzi, A. Kiermasz, and W. Eccleston, " Plasma Oxidation of Silicon, " *Plasma Phys.*, vol. 24, no. 6, pp. 605-614, 1982.

[83] A. Kiermasz, W. Eccleston, and J. L. Moruzzi, " Theory of the Growth of SiO_2 in an Oxygen Plasma, " *Solid-State Electron.*, vol. 26, no. 12, pp. 1167-1172, 1983.

[84] J. V. Cole, H.H. Lee, " General Relationships for Plasma Oxidation, " *J. Electrochem. Soc.*, vol. 138, no. 2, pp. 567-571, 1991.

[85] K.J. Barlow, A. Kiermasz, W. Eccleston, " An Improved Theory for the Plasma Anodization of Silicon, " *IEE Proceedings*, vol 132, no.4, pp. 181-183, 1985.

[86] C. Vinckier, S. D. Jaegere, " Yields of the Plasma Oxidation of Silicon by Neutral Oxygen Atoms and Negative Oxygen Ions, " *J. Electrochem. Soc.*, vol. 137, no. 2, pp. 628-631, 1990.

[87] R. Oren, S.K. Ghandhi, " UltraViolet-Enhanced Oxidation of Silicon, " *J. Appl. Phys.*, vol. 42, no. 2, pp. 752-756, 1971.

[88] V. Cracium, I.W. Boyd, A.H. Reader, W. J. Kersten, F. J. G. Hakkens, P. H. Oosting, D. E. W. Vandenhoudt, " Microstructure of Oxidized Layers Formed by the Low-Temperature UltraViolet-Assisted Dry Oxidation of Strained $Si_{0.8}Ge_{0.2}$ Layers on Si, " *J. Appl. Phys.*, vol. 75, no. 4, pp. 1972-1976, 1994.

[89] E.M. Young, " Electron-Active silicon Oxidation, " *Appl. Phys. A*, vol. 47, pp. 259-269, 1988.

[90] S.M. Sayedi, L. M. Landsberger, D. Landheer, M. Kahrizi, " Mechanisms of Film Growth Rate Enhancement in Anodic and Cathodic Corona-Discharge Oxidation Processes, " presented in *Electrochemical Society Conference*, Montreal, Canada, May, 1997.

[91] N. F. Mott, S. Rigo, F. Rochet, and A.M. Stoneham, " Oxidation of Silicon, " *Philos. Mag.* B, vol. 60, no. 2, pp. 189-212, 1989.

[92] A.M. Stoneham, C.R.M. Grovenor, and A. Cerezo, " Oxidation and the Structure of the Silicon/Oxide Interface, " *Philos. Mag.* B, vol. 55, no. 2, pp. 201-210, 1987.

[93] E.M. Young and W.A. Tiller, " Photon Enhanced Oxidation of Silicon, " *Appl. Phys. Lett*, vol. 42, no.1, pp. 63-65, 1983.

[94] E.M. Young and W.A. Tiller, " Ultraviolet Light Stimulated Thermal Oxidation of Silicon, " *Appl. Phys. Lett*, vol. 50, no. 2, pp. 80-82, 1987.

[95] E.A. Irene and E.A. Lewis, " Thermionic Emission Model for The Initial Regime of Silicon Oxidation, " *Appl. Phys. Lett.*, vol. 51, no. 10, pp. 767-769, 1987.

[96] S.A. Schafer, S. A. Lyon, " Optically Enhanced Oxidation of Semiconductors, " *J.*

Vac. Sci. Technol., vol. 19, no. 3, pp. 494-497, 1981.

[97] D. J. DiMaria, R. Ghez, D. W. Dong, " Charge Trapping Studies in SiO_2 Using High Current Injection From Si-rich SiO_2 Films, " *J. Appl. Phys.*, vol. 51, no. 9, pp. 4830-4841, 1980.

[98] D. J. DiMaria, " Hole Trapping, Substrate Current, and Breakdown in Thin Silicon Dioxide Films, " *IEEE Electron Device Letters*, vol. 16, no. 5, pp. 184-186, 1995.

[99] D. J. Dumin, " Wearout and Breakdown in Thin Silicon Oxide, " *J. Electrochem. Soc.*, vol. 142, no. 4, pp. 1272-1277, 1995.

[100] D. J. DiMaria, " Determination of Insulator Bulk Trapped Charge Densities and Centroids From Photocurrent-Voltage Characteristics of MOS Structures, " *J. Appl. Phys.*, vol. 47, no. 9, pp. 4073-4077, 1976.

[101] S. M. Sze, *VLSI Technology*. McGraw-Hill Book Company, p. 155, 1983.

Appendix A

Corona Discharge Apparatus and Experimental Parameters

A detailed schematic illustration of the apparatus used in this study shown in Fig. A.1 [22, 26]. Basic features of the apparatus mentioned before in Chapter 2 can be found with more details in references [22,26]. In this appendix, some data related to the parameters of the experiments are presented.

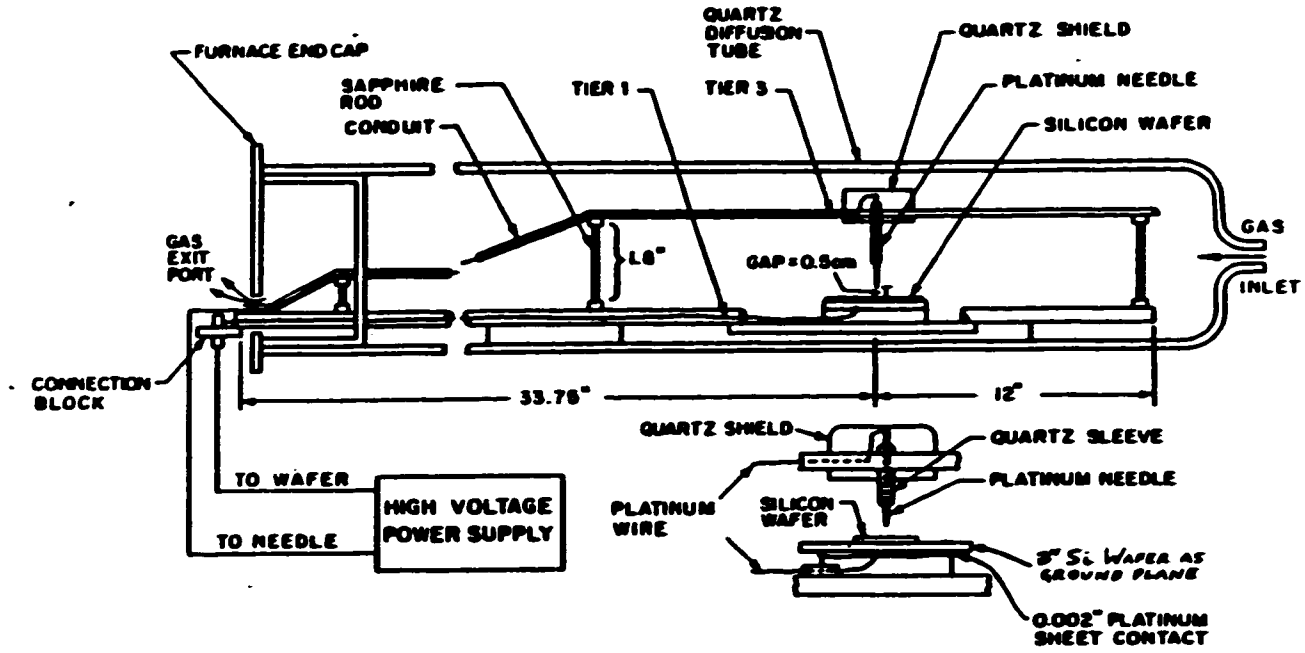

Fig. A.1: Illustration of the corona apparatus used in this work. [22,26[

Fig. A.2(a) shows schematically the position of the sample inside the apparatus in respect to the circuit connected to it. Four main parameters of V_h, V_l, I_h, and I_l shown in

the figure can be monitored during experiment. R_l in the figure represents the effect of leakage current between the apparatus needle and the ground wire. Practically R_2 is very big, and as a result I_l is considered the wafer current. In the case of constant-current operation, by use of feedback control circuits, this current is held constant.Fig. A.2(a) shows a typical variation of the apparatus voltages and currents during a negative corona experiment done in the constant-current mode. The thickness profile of the resulting oxide is shown in Fig.A.3.

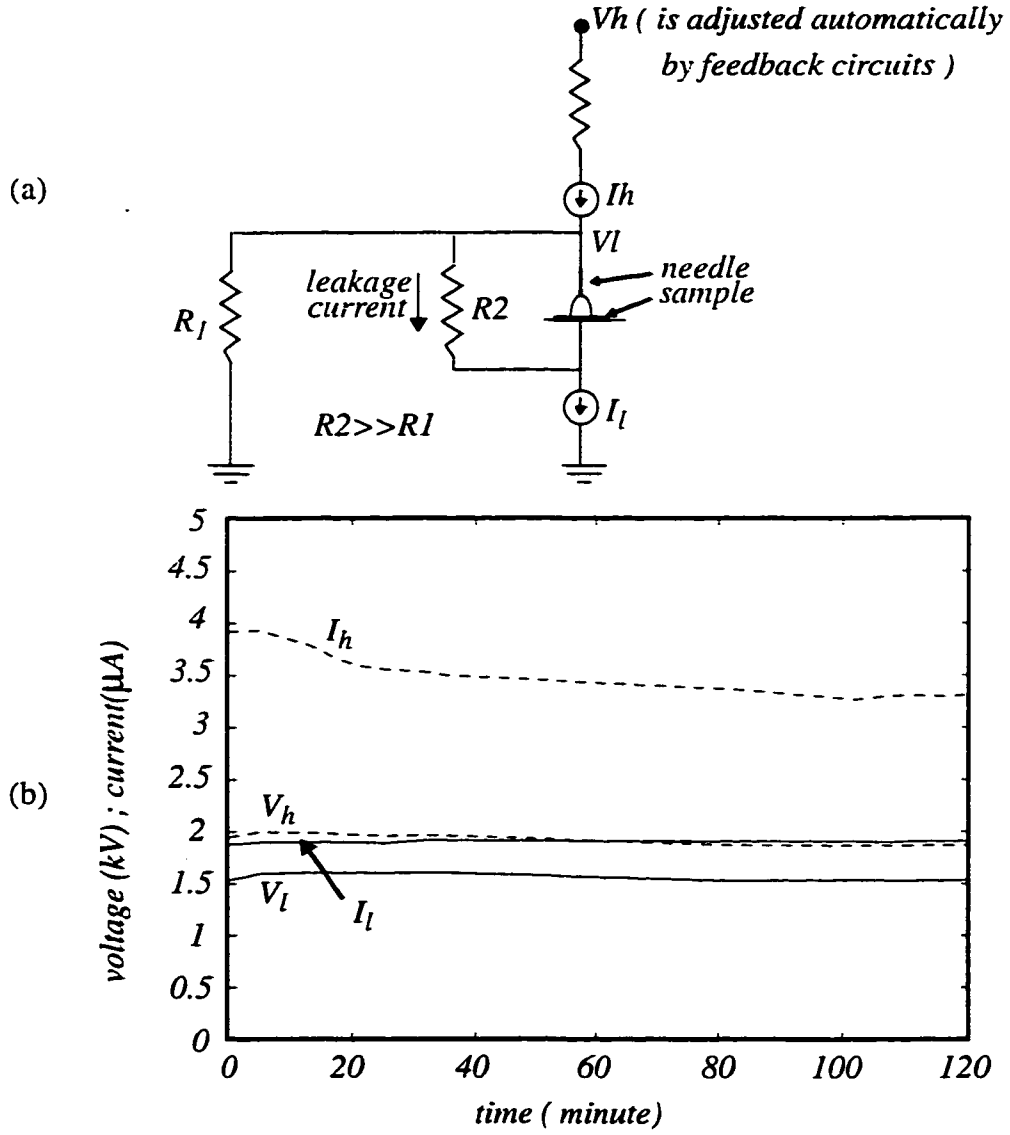

Fig. A.2: a): Position of the sample with respect to the circuits connected to it, b): voltage and current changes for a negative corona experiment with t_{cor}=2hours, I_{cor} set to 2 μA, and temperature = 840°C.

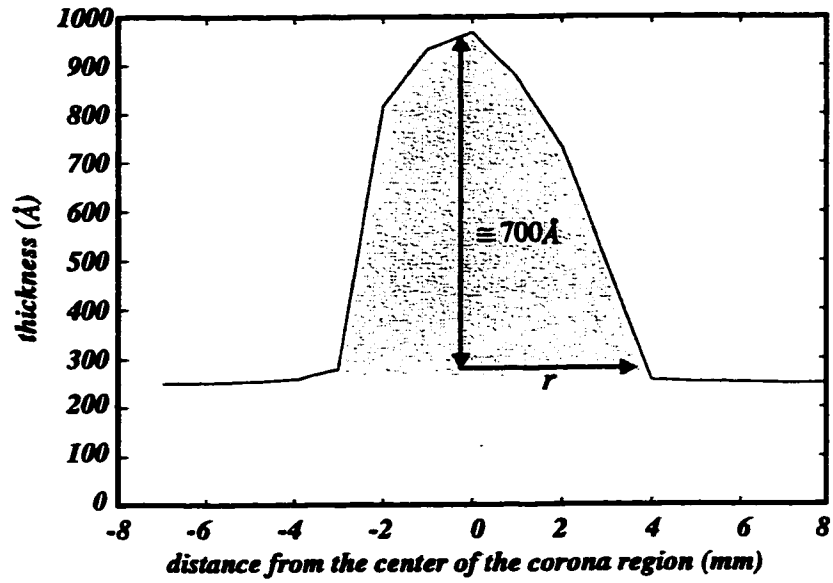

Fig. A.3: Thickness profile of an oxide film resulting from the experiment shown in Fig. A.2(b). The shaded area shows the part of the oxide that is grown due to the corona effect.

A.I Relation Between Corona Current and Oxide Volume in the Negative Corona Process

It has been shown [26] that in a negative-point corona process, the number of electrons which are passed through the film during the process is close to the number of oxygen atoms incorporated into the oxide structure as the result of the corona. To examine that phenomenon for the results of this work, and more importantly, to examine that if the phenomenon is valid for the results of experiments in which the grid-wafer was used (as the cathode as presented in Chapter 4, the following calculations are done for the profile result shown above in Fig.A.3, for two cases of thin oxide profiles presented in Chapter 3 (one corona-grown, Fig.3.3 (a), and one corona-treated film, Fig.3.4 (a)), and for two results of Chapter 4, Fig. 4.5(a and b), which are related to the use of a grid-wafer as the cathode.

For the thickness profile shown in Fig.A.3 the extra thickness of the oxide, at different locations of the film, resulted from corona effect, can be approximated as follows:

$$t_{ox\text{-}cor}(r)=700*10^{-8}-43.75*10^{-6}*r^2$$

where r is distance from the center. The volume of extra oxide can be calculated by integrating above equation;

$$\int_0^{2\pi}\int_0^{0.4} t_{ox\text{-}cor}* r*dr*d\theta = 175.9*10^{-8}cm^3$$

multiplying above number to the number of oxygen atoms in unit volume of oxide ($4.6*10^{22}$ cm^{-3}) results the number of oxygen atoms in the oxide film:

$$\underline{\text{number of oxygen atoms}} \cong 175.9*10^{-8} * 4.6*10^{22} = \underline{8.09 * 10^{16}}$$

The number of electrons which pass through the film during a corona process step is calculated based on the time of the corona process (2 hours) and the current of the process (1.91 μA):

$$\underline{\text{number of electrons}} \cong 1.91*10^{-6} * 2*3600 * 6.24 *10^{18} = \underline{8.58*10^{16}}$$

As the results show, the two above numbers are very close.

For Fig.3.3 (a) time of corona process is 25 minutes, corona current is 2 μA, the extra thickness at the center is about 170 Å and r is about 0.3 cm. Similar calculations to the above yield:

$$\underline{\text{number of oxygen atoms}} \cong 24*10^{-8}*4.6*10^{22}=\underline{1.11*10^{16}}$$

$$\underline{\text{number of electrons}} \cong 2*10^{-6} * 25 *60* 6.24 *10^{18} = \underline{1.87*10^{16}}$$

For Fig.3.4 (a) time of corona treatment is 2 minutes, corona current is 2 μA, the extra thickness at the center is about 22 Å and r is about 0.35 cm. Similar calculations to the above yield:

number of oxygen atoms $\cong 5.2*10^{-8}*4.6*10^{22}=2.40*10^{15}$

number of electrons $\cong 2*10^{-6} * 2 *60* 6.24 *10^{18} = 1.49*10^{15}$

The above results show a close relation between the number of oxygen atoms and number of electrons.

For the case of using a grid-wafer (instead of a single needle), two oxide profiles of Fig. 4.5(a and b) in Chapter 4are examined. Considering the shape of the curves for two profiles, the approximate volumes of oxides can be calculated by multiplying the average of the extra oxide thicknesses (that is due to corona effect) to the areas of the effected areas of the wafers. For Fig. 4.5(a) the area is about 8 (the width that shown in the figure) * 6 (the width of the wafer) =48 cm^2, and for Fig. 4.5(b) it is about 6.5 (the width that shown in the figure) * 6 (the width of the wafer) = 39 cm^2.

For Fig. 4.5(a) :

oxide volume created due to corona effect $\cong$

$$48 * (400-100)*10^{-8}= 1.4*10^{-4}cm^3$$

number of oxygen atoms $\cong 1.4*10^{-4}*4.6*10^{22} = 6.62 * 10^{18}$

The number of electrons which pass through the film during a corona process step, based on the time of the corona process (3 hours) and the current of the process (10 μA):

number of electrons $\cong 10 *10^{-6} * 3 *3600 * 6.24 *10^{18} = 6.73 *10^{17}$

For Fig. 4.5(b) :

oxide volume created due to corona effect $\cong$

$$39 * (1000\text{-}400)*10^{-8} = 2.34*10^{-4}\text{cm}^3$$

number of oxygen atoms $\cong 2.34*10^{-4}*4.6*10^{22} = \underline{1.08*10^{19}}$

The number of electrons passed through the film during corona process based on time of corona process (3 hours) and current of the process (10 μA):

$\underline{\text{number of electrons}} \cong 4*10^{-6}*22*3600*6.24*10^{18} = \underline{1.98*10^{18}}$

As the results show, for these two cases the numbers of oxygen atoms are greater than the numbers of electrons.

A.II Comparison of Needle Voltages, in Negative and Positive Corona Processes

The values of voltages and currents during both negative and positive corona processes showed that for equal magnitude of currents, and for the same geometric conditions of the needle and wafer, the voltages needed for the needle (to hold current at its pre-set level), are greater in the negative corona case. Two examples of the voltage values for each case are shown in Fig. A.4.

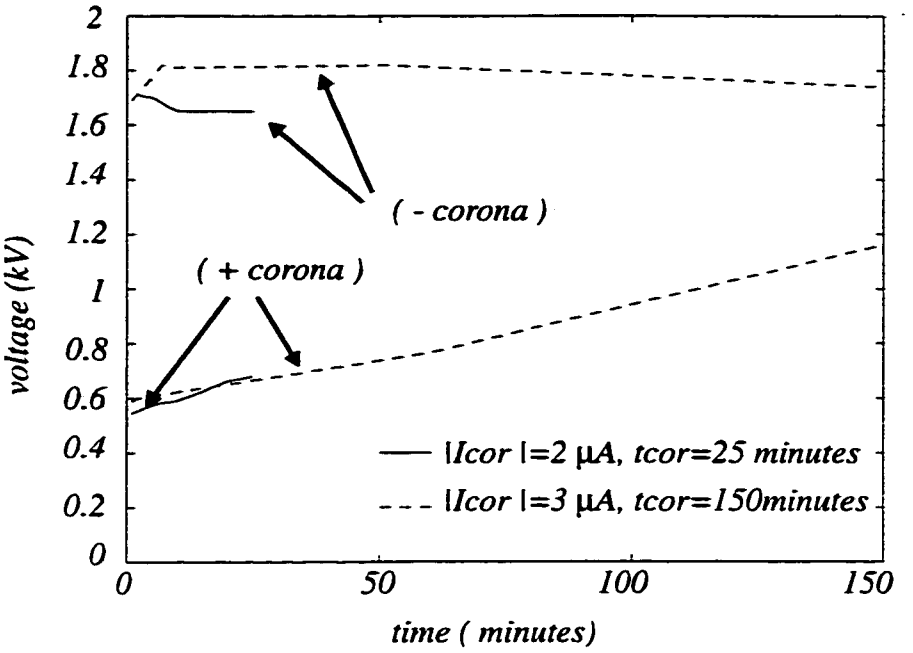

Fig. A.4: Two examples of needle voltage changes for each case of negative and positive corona process. The temperature of oxidation for all four results shown was 800°C.

Appendix B

Detailed Description of Fabrication Procedures

B.I Reverse RCA Cleaning Procedure

- 1 : 1 H_2SO_4 : H_2O , 5 minutes on hot plate, boiling.
- Rinse in D.I. water.
- 1 : 1 : 5 HCl : H_2O_2 : H_2O , 5 minutes on hot plate, boiling .
- Rinse in D.I. water.
- Dip in HF : H_2O (1 : 50) for 30 seconds.
- Rinse in D.I. water.
- 1 : 1 : 5 NH_4OH : H_2O_2 : H_2O , 5 minutes on hot plate, no boiling.
- Rinse in D.I. water.

B.II Corona Oxidation and Treatment Protocols

The following describes the processing sequence for preparing corona-grown, corona-treated, and two-step corona-treated oxide films.

Corona-grown film:

1- Begin with a slice of wafer (approximately square-shaped having side approximately 3 cm.

2- Reverse-RCA cleaning procedure.

3- Keep in D.I. water before loading into oxidation tube.

4- Transport wafer(s) (under D.I. water) to laminar flow station at entry to oxidation tube.

5- Adjust furnace temperature setting.

6- Ensure that N_2 flows in tube.

Under laminar flow:

7- Carefully remove furnace baffle and pull out apparatus.

8- Blow dry wafer on lint-free paper with N_2 .

9- Load the wafer on the silicon ground plate (under needle) .

10- Push slowly the apparatus into the tube and replace furnace baffle (in 10-15 minutes to avoid thermal shock.)

11- Connect thermocouple wire to apparatus thermocouple and monitor temperature on thermocouple readout from now on.

12- When T reaches the intended process temperature (800°C) change the gas flow from N_2 to O_2.

13- After 1 minute, turn on the high voltage supply in constant current mode,(I=~ 0.5 μA to ~ 40 μA.)

14- After the specific experimental time (e.g. 25 minutes), turn off the corona current.

15- After 1 minute change the ambient from O_2 to N_2.

16- After 1 minute, remove the baffle and slowly pull the apparatus out from the tube (in 10-15 minutes.)

17- Using tweezers carefully remove the wafer from the ground plate.

18- Cool the wafer by N_2 gun.

19- put the wafer in a clean petri-dish.

Corona-treated film:

The procedure is mostly like the one of corona-grown film with two main differences:

- between steps 3 and 4 there is a step of conventional dry oxidation at

800°C to grow a certain thickness of thermal oxide.

- at step 14 the time of corona process is lower(e.g. 2 minutes).

Two-step Corona-treated film:

The procedure is mostly like that of the corona-grown film with some differences:

-between steps 3 and 4 there is a step of conventional dry oxidation at 800°C to grow a certain thickness of thermal oxide.

- at step 14 the time of corona process is lower (e.g. 2 minutes).

- at step 17 instead of removing the sample, the location of sample under the needle is changed slightly (about 3 mm) and following that:

18- Slowly push the apparatus into the tube and replace furnace baffle (in 10-15 minutes to avoid thermal shock.)

19- Connect thermocouple wire to apparatus thermocouple and monitor temperature on thermocouple readout from now on.

20- When T reaches the intended process temperature (800°C) change the gas flow from N_2 to O_2.

21- After 1 minute, turn on the high voltage supply in constant current mode,(I=~ 0.5 μA to ~ 40 μA.)

22- After the specific experimental time (e.g. 2 minutes), turn off the corona current.

23- After 1 minute change the ambient from O_2 to N_2.

24- After 1 minute, remove the baffle and slowly pull the apparatus out from the tube (in 10-15 minutes.)

25 - Using tweezers carefully remove the wafer from the ground plate.

26- Cool the wafer by N_2 gun.

B.III Metallization

Two different procedures were used for metalization. One uses a shadow mask, and the other uses photoresist and lithography procedures. The latter was especially used in fabricating MOS structures with smaller areas.

B.III .1 Using a Shadow Mask:

1- Set the wafer on Shadow mask. (The mask includes many circular holes with diameters of 0.5 - 1 mm. The distance between centers of adjacent circles is 2mm (Fig. B.1))

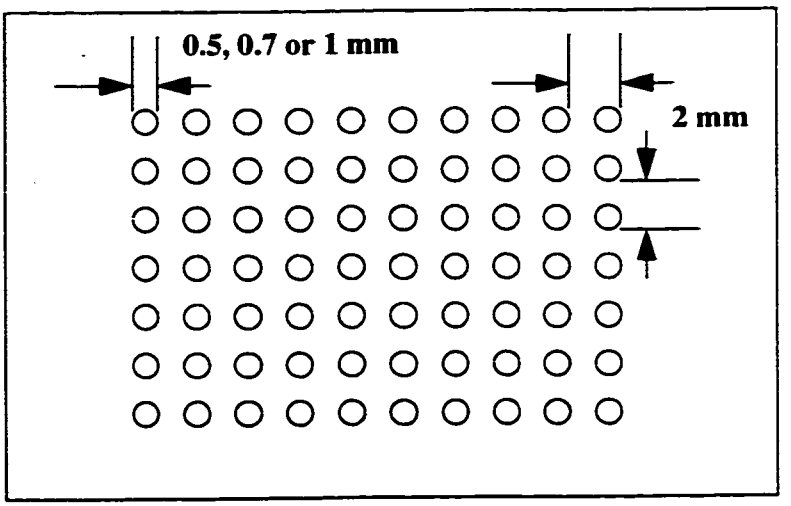

Fig. B.1: The Shadow mask used in metallization process.

2- Load wafer and Mask into Aluminium evaporator. (thermal evaporation using an Aluminium filament)

3- Evaporate about 1000Å Al on top of the wafer through the Shadow mask.

4- Etch wafer backside oxide using cotton Q-tip and 1 : 20 HF : H_2O .

5- Evaporate (unmasked) about 1000Å Al on backside of wafer

6- Anneal the wafer in annealing tube in ambient of 80% N_2 and 20% H_2, at 400°C for 10 minutes.

The wafer is now ready for electrical testing.

B.III .2 The photo-lithography procedure:

1- Set the wafer on spinner chuck and secure it with vacuum.

2- Blow off dust particles with N_2 gun.

3- Apply 3-4 drops of positive photoresist with a filter-equiped syringe.

4- Spin at 3000 rpm for 30 seconds.

5- Soft Bake in forced-air convention oven for 30 minutes at 95 °C.

6- Allow wafer to cool for 15 minutes.

7- Expose to UV light through the mask that has desired pattern on it.

8- Dip in stirred developer solution for few minuters so that the photoresist is stripped away from exposed area.

9- Rinse in D.I. water.

10- Blow dry with N_2 gun.

11- Dry in forced-air convention oven for 30 minutes at 95 °C.

12- Load wafer into Aluminium evaporator. (thermal evaporation using an Aluminium filament)

13- Evaporate about 1000Å Al on top of the wafer through the open windows

of the photoresist layer.

14- Soak the wafer in acetone for a few minutes so that the photoresist with the Al on top of it is lifted off.

15- Rinse in D.I. water.

16- Blow dry with N_2 gun.

17- Etch backside oxide using cotton Q-tip and 1 : 20 $HF : H_2O$.

18- Evaporate about 1000Å Al on backside of wafer

19- Anneal the wafer in annealing tube in ambient of 80% N_2 and 20% H_2, at 400°C for 10 minutes.

The wafer is now ready for electrical testing.

Appendix C

Oxide Charges and Electrical Measurements Details

C.I Oxide Charge Types

The following categorizes different oxide charge types and explains their locations in the gate oxide (Fig. C.1) [1,3,4]:

Oxide fixed charges are predominantly positive and exist approximately within 50Å of the interface. They are immobile under an applied electrical field and do not exchange charge with the silicon when gate bias is varied. Since they are predominantly positive, they shift the threshold voltage (V_{th}) negatively.

Interface trap charges occur because of the existence of interface traps, within 10Å of the Si/SiO_2 interface, which are energy levels distributed through out the band gap of the energy band diagram of a semiconductor at Si/SiO_2 interface. The reason for these extra energy states is the abrupt termination of the periodic semiconductor crystal at the interface. These traps become charged by exchange of electrons or holes with the silicon when the gate bias is varied.

Oxide trapped charges occur because of the existence of defects in the oxide bulk. They are located often near interfaces. Oxide traps become charged when charges are injected through the oxide . They can also be caused by ion implantation or ionizing radiation.

Mobile ionic charges most commonly reflect the presence of ionized alkali metal atoms such as sodium or potassium. They are located either at the metal-SiO_2 interface, where they originally entered the oxide layer, or at the Si/SiO_2 interface where they have drifted under an applied field. These are not commonly a problem due to the extreme cleanliness enforced on fabrication processes.

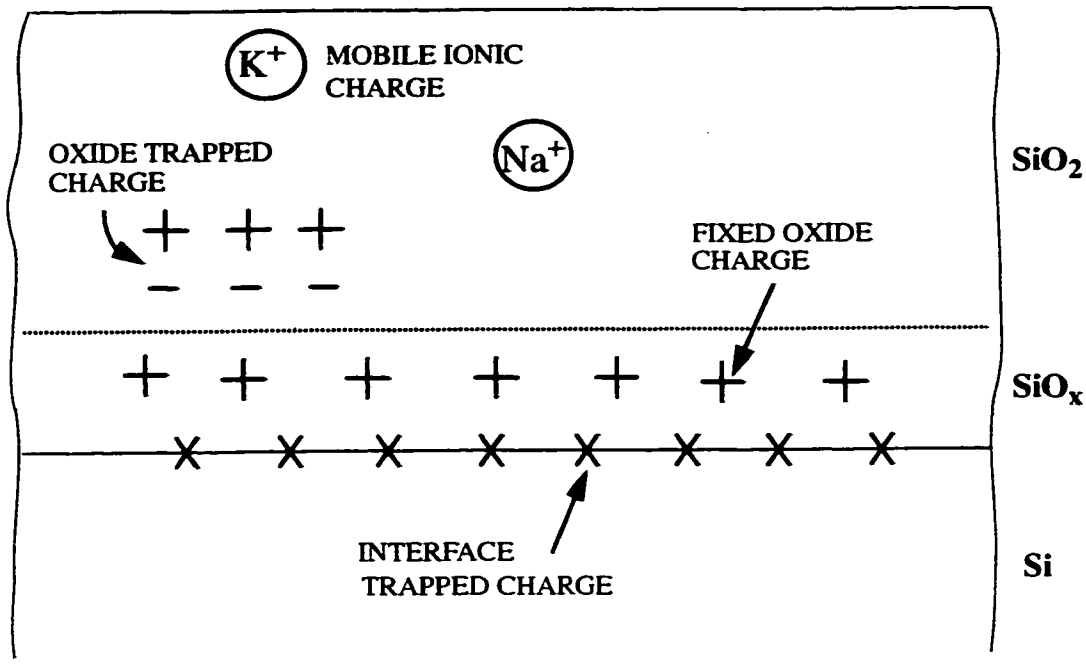

Fig. C.1: Different types of oxide charges in an oxide film (Redrawn from Ref [101]).

C.II Evaluation of Oxide Quality

The main reasons for changes of MOSFET parameters during use are one or both of: (a) the change in concentration of bulk and interface charges, and (b) change in the centroid of the location of the charges. These changes can dramatically influence the threshold voltage (V_{th}) of the MOSFET.

The rate of change of charge density mostly depends on the density of the charge traps in the oxide. These traps are defect sites which are created during fabrication or during application of electrical stress on the oxide [40]. Good understanding of the position and density of these traps and the probable mechanism of change of density and

centroid of these traps is the main aim of many studies related to evaluation of oxide quality. In fact, these sites via their charging (or discharging) have the potential to change the parameters of the MOSFET.

To determine the density and position of charge traps it is necessary somehow that they be filled by charges so that later or simultaneously by electrical measurements the position and centroid of them can be determined. Different techniques like Fowler-Nordheim tunneling, photo injection, hot carrier and so on are used to charge the traps [41, 97,98, 100].

There are many ways to evaluate the amount and position of trapped charges; for example, C-V measurements determine the product of the amount of oxide charges and their centroid; Photo-I-V or I-t measurement determines both the amount and centroid of the bulk charges; by combination of the C-V and Photo-I-V (or I-t) measurements the number of interfacial Si/SiO_2 charges and the number of interface states can be determined.

In addition to the charging and discharging of as-fabricated traps that can change the MOSFET parameters, the number of charge traps can be changed during electrical stressing of oxide. These traps can accept or donate charges, increasing the change of MOSFET parameters. Trap creation, impact ionization and their relation to the energy of the electrons which pass through the oxide during stressing of the oxide are some relevant topics that have been studied in detail in recent work by many researchers [for example 40,99].

C.II .1 C-V Measurements

The MOS (Metal-Oxide-Semiconductor) capacitor consists of a parallel plate capacitor with one electrode being a metallic plate, called the gate, and the other electrode being

the silicon. The two electrodes are separated by a thin insulating layer of SiO_2 (Fig. C.2). The "metal" electrode may be actually metal (like Aluminum) or deposited high-conductivity polysilicon, as it is in many cases.

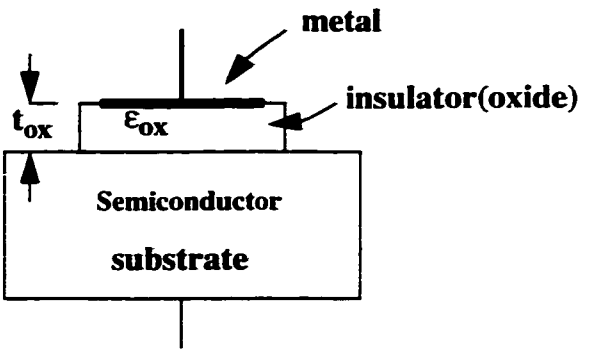

Fig. C.2: The basic structure of MOS.

In C-V measurement as shown in Fig. C.3(a) the capacitance is measured at different bias voltages. Depending on the gate voltage, the substrate immediately before the Si/SiO_2 interface may be in accumulation, depletion or inversion. At each voltage, the value of capacitance is measured. Fig. C.3(b- solid curves) shows typical HFCV and LFCV curves of a N-substrate MOS capacitor. Based on the amount and position of oxide charges the C-V curves can be different from the ones of a MOS capacitor with a charge-free oxide. This difference, which may include the change of horizontal position or/and some distortion (Fig. C.3(b) dashed curves), is used to obtain information about oxide charges and Si/SiO_2 interface states [1].

C.II .2 I-t Measurements

In I-t measurements, as shown in Fig. C.4(a), a constant voltage (high enough to cause the Fowler-Nordheim tunneling phenomenon) is applied to the MOS structure and

the gate current is monitored [1, 40, 41]. For an ideal MOS structure the current should be constant. However, the change of gate oxide charge densities due to the voltage and current flow changes the characteristics of the original MOS structure and as a result the current may change. For example - for the case of applying positive voltage - creation of positive charges in the bulk oxide can increase the gate current, and creation of negative charges can decrease the current. Fig. C.4(b) shows a typical I-t curve; the part between points a and b shows creation of positive charges, the part between points b and c shows creation of negative charges (or annealing of already created positive charges) and part between points c and d shows creation of more negative charges in such a way that the net trapped charge is negative. I-t measurements evaluate the quality of the oxide by examining its resistance to the generation of new defects and charges. I-t analysis is discussed in more detail in following section.

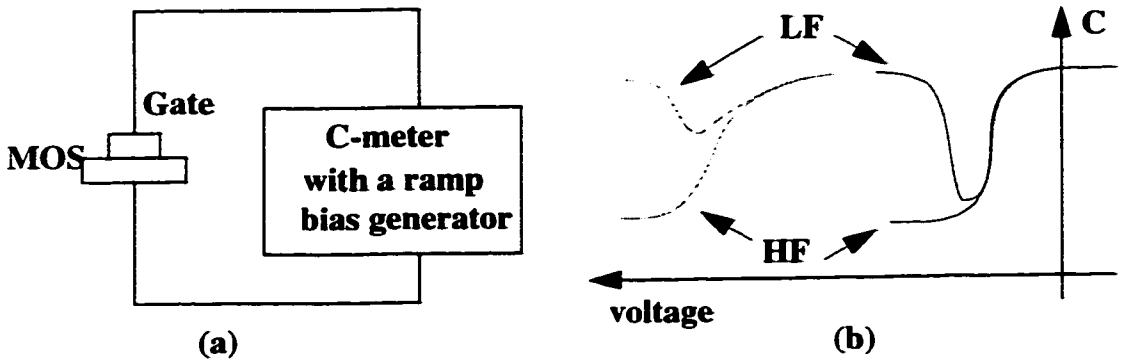

Fig. C.3: C-V measurement technique.

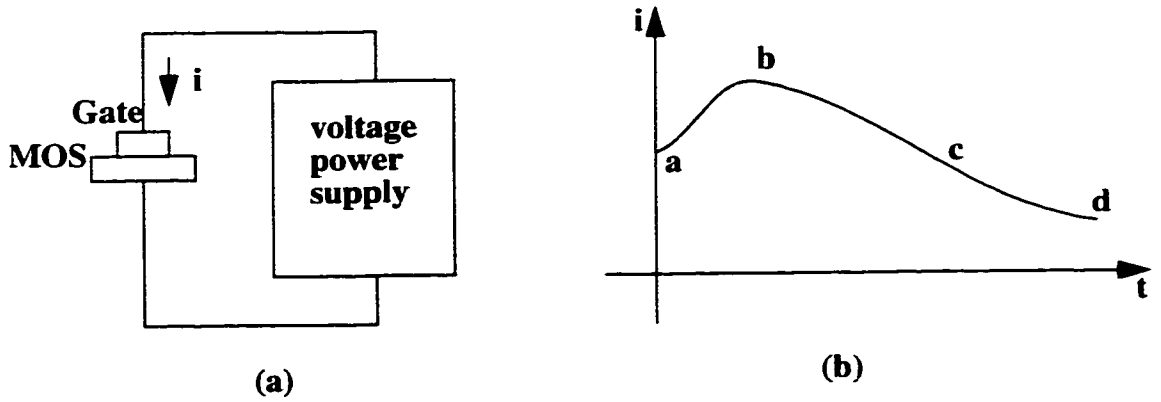

Fig. C.4: I-t measurement technique.

C.III I-t and C-V Measurement Theory

As mentioned above, I-t measurement is used to obtain information about bulk trapped charges (Q_b). This measurement senses the effect of bulk trapped charge build-up on the oxide internal field near the injecting interface. Fig. C.5 shows schematically the internal field in an oxide for both cases: (a) $Q_b \cong 0$, and (b) $Q_b \neq 0$. As the figure shows, because of the existence of bulk trapped charges near the cathode interface, the field near that interface changes. This, in turn, changes the oxide current. By making some assumptions, the relation between Q_b and the oxide current can be obtained.

By assuming that bulk trapped charges are near the cathode interface (but at least a tunneling distance away from that interface), the effect of these charges on the oxide field near the interface is the same as the effect of changing the gate voltage by the value of $Q_b X_b/\epsilon_{ox}$, in which X_b (measured from the gate oxide interface) is the centroid of bulk

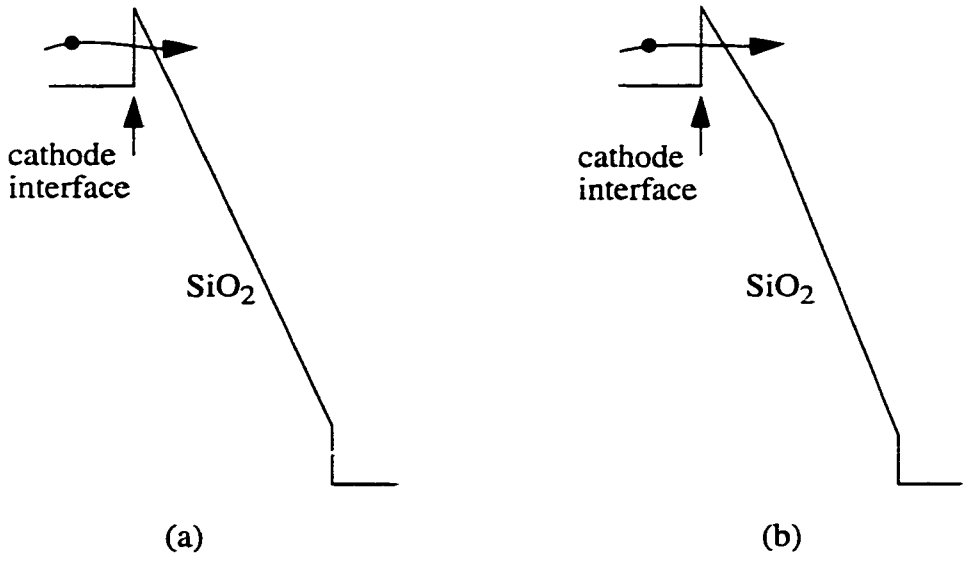

Fig. C.5: Energy band diagrams of SiO_2 during I-t measurement;
a: $Q_b \cong 0$
b:the effect of some negative bulk trapped charges near the cathode interface.

trapped charges and ε_{ox} is oxide low frequency dielectric. Under this condition the field near cathode interface is equal to $E_{ox}(ave)-(Q_bX_b/\varepsilon_{ox}L)$, in which L is oxide thickness and $E_{ox}(ave)$ is equal to V_{ox}(oxide voltage)/L. The relation between Fowler-Nordheim current and the oxide field near cathode interface is as following:

$$J = AF^2 exp\,(-\frac{B}{F}) \tag{1}$$

where:

F: field near cathode interface

A and B : constants

J : oxide current density

At the beginning of the stress, the field near the cathode interface is equal to the average oxide field (because Q_b=0) and we have:

$$J(0) = AE_{ox}(ave)^2 exp\left(-\frac{B}{E_{ox}(ave)}\right) \tag{2}$$

During the stress, and consequent change in Q_b, the field near cathode will change and we will have:

$$J(t) = A\left(E_{ox}(ave) - \frac{Q_bX_b}{\varepsilon_{ox}L}\right)^2 exp\left(-\frac{B}{E_{ox}(ave) - \frac{Q_bX_b}{\varepsilon_{ox}L}}\right) \tag{3}$$

For the case of applying constant voltage during stress, $E_{ox}(ave)$ will be constant. By dividing both sides of Equation (3) by the corresponding sides of Equation (2) the follow-

ing equation can be obtained:

$$ln\left(\frac{J(t)}{J(0)}\right) \equiv \frac{BQ_bX_b}{E_{ox}(ave)^2\varepsilon_{ox}L} \tag{4}$$

As Eq.(4) shows, we have information about the product of Q_b and X_b. In the condition of $(X_b/L) \equiv 1$ (the condition that usually exists for thick oxide) we will have:

$$Q_b = E_{ox}(ave)^2\varepsilon_{ox}B^{-1}ln\left(\frac{J(t)}{J(0)}\right) \tag{5}$$

For the condition of applying constant gate current, comparison of Eqs. (2) and (3) shows that:

If $J(0) = J(t) \Rightarrow$

$$E_{ox}(ave)_{/t=0} = E_{ox}(ave)_{/t>0} - (Q_bX_b/\varepsilon_{ox}L)$$

$$V_{ox}(0)/L = V_{ox}(t)/L - (Q_bX_b/\varepsilon_{ox}L)$$

$$Q_bX_b = \Delta V_{ox}\varepsilon_{ox} \tag{6}$$

by assuming that silicon surface potential changes during stress are negligible , Eq. (6) yields following equation:

$$\Delta v_g = \frac{X_b}{\varepsilon_{ox}}Q_b \tag{7}$$

where Δv_g ($\approx\Delta V_{ox}$) is the change of gate voltage.

Equations (5) and (7) show that the I-t technique does not give any information about interfacial charges. The usual technique to obtain information about total charges in oxide is C-V measurement. C-V measurement determines the product of total oxide

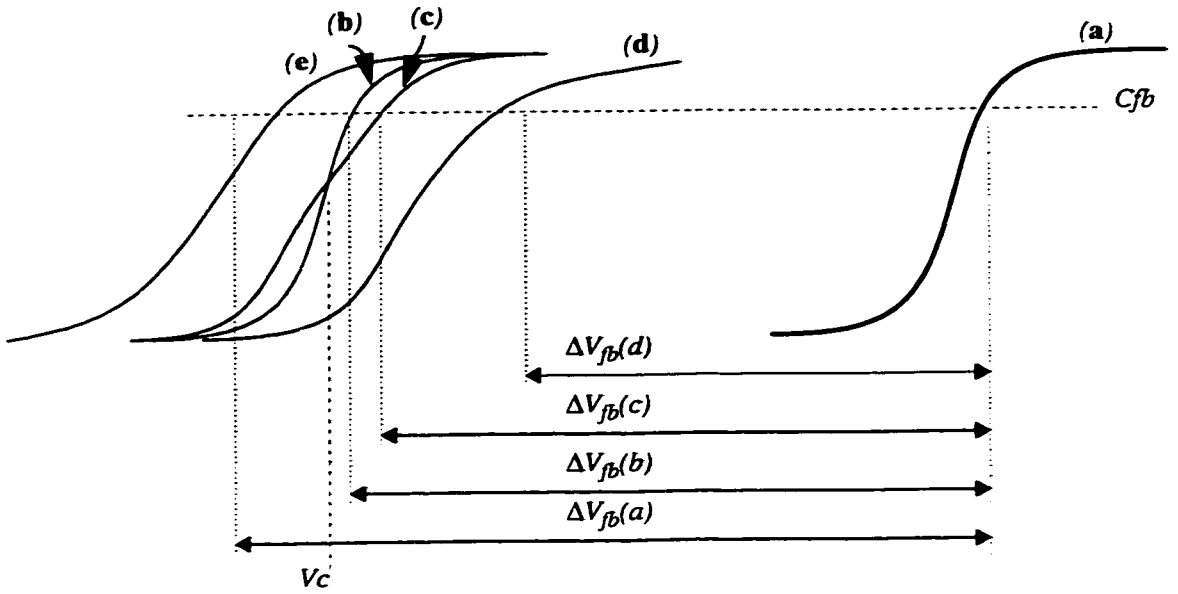

Fig. C.6: Effect of oxide and interface charges on the C-V curve.

charge density (Q_{to}) and the centroid of the charges (X_{to}) :

$$X_{to} \cdot Q_{to} = \Delta V \cdot \varepsilon_{ox} \tag{8}$$

[Q_{to}= Q_b (bulk charge density) + Q_i (interfacial charge density)]

ΔV is the change of voltage in C-V curve. To minimize the effect of interface state charges (ΔQ_{it}) and the silicon substrate charges (ΔQ_s) on measuring Q_{to}; ΔV is measured at flat-band voltage.

$$X_{to} \cdot Q_{to} = \Delta V_{fb} \cdot \varepsilon_{ox} \tag{9}$$

On this situation the measured Q_{to} still includes not only trapped bulk charges and trapped interfacial charges, but also $\Delta Q_{it}(0)$ and $\Delta Q_s(0)$. Fig. C.6 shows how the measured Q_{to} includes $\Delta Q_{it}(0)$.

If curve(**a**) is a high frequency C-V curve for a charge-free oxide , the existence of

oxide charges causes the curve shift horizontally to the left or right. Curve(**b**) shows the effect of a positive charge which causes a shift to the left. Interface state charges not only cause a smearing-out of the curve (curve(**c**)), but they also can shift the curve more to the right or left (curves **d** and **e**).

Curve(**e**) shows the case where all interface states are donor type. For this case, in carrier accumulation, (which corresponds to the right section of the curve), the donor states are filled with electrons and there is no net charge created by these states. Curve(**e**) shows that for accumulation there is no extra shift in comparison to that of Curve(**b**). By decreasing the applied gate voltage, the electrons in donor states are repelled, and as a result there is a net positive charge at interface. Extra shift to the left at the inversion region of curve (**e**), compared to that of curve (**b**), is caused by this positive charge. The usual "U" shape of the density of interface states shows that for the case of curve(**e**) the distribution of interface states is as following:

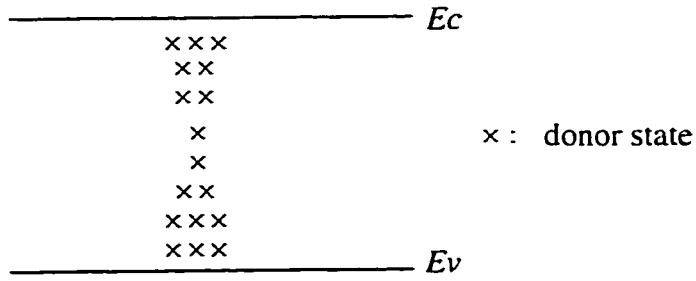

Curve(**d**) shows a case in which all interface states are acceptor type. For this case, during the inversion condition (which corresponds to the left section of the curve), the acceptor states are empty and there is no net charge created by these states. Curve (**d**) shows that in inversion there is no extra shift compare to that of curve(**b**). By increasing the applied gate voltage, the acceptor states are filled with electrons, and as a result there is a net negative charge at interface. Extra shift to the right at the accumulation region of curve(**d**), compared to that of curve(**b**), is caused by this negative charge. The usual "U"

shape of the density of interface states shows that for the case of curve(**d**) the distribution of interface states is as following:

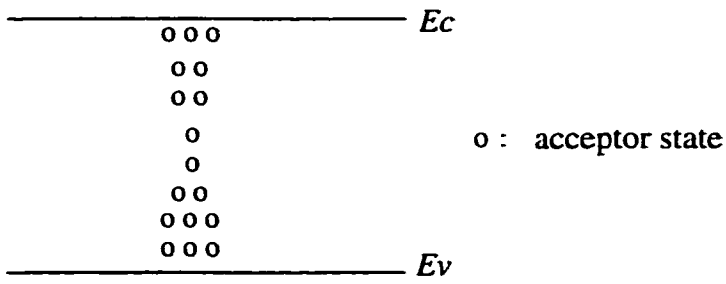

curve(**c**) shows the case that the interface states in the upper part of the energy band of SiO_2 are acceptor type, while in the lower part of the band they are donor type. For this case, for voltages higher than V_c (in figure 2), curve(**c**) shifts to the right side of curve(**b**), which means the net interface charges are negative (caused by acceptor states). and for the voltages lower than V_c, curve(**c**) shifts to the left side of curve(**b**), which means the net interface charges are positive (caused by donor states). At voltage V_c, the net value of interface charges is zero. The usual "U" shape of the density of interface states shows that for the case of curve(**c**) the distribution of interface states is as follows:

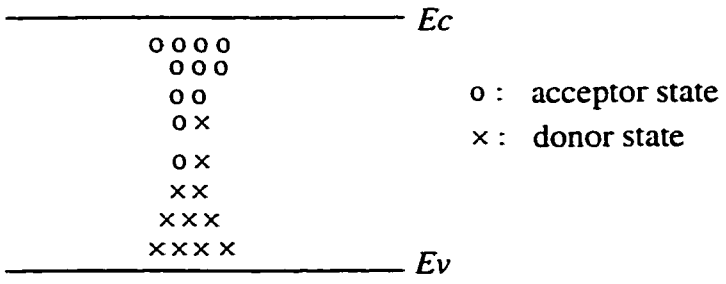

From the four different values of ΔV_{fb} that are shown on Fig. C.6, the only value that gives the real value of Q_{to} (by using equation (8)) is $\Delta V_{fb(b)}$; however, practically by C-V measurement we have one of the three values of $\Delta V_{fb(c)}$, $\Delta V_{fb(d)}$ or $\Delta V_{fb(e)}$, that we refer to that as ΔV_{fb} . The difference between this value and $\Delta V_{fb(b)}$ determines how many interface state charges play a role in the shift of the C-V curve.

$$Q_{it}(0) = \frac{\Delta V_{fb} - \Delta V_{fb\,(b)}}{X_{to}} \varepsilon_{ox} \qquad (10)$$

It is shown that the usual situation for C-V curves is curve (*c*) for which $\Delta V_{fb}(c) \approx \Delta V_{fb}(b)$ and as a result the measured Q_{to} (by using equation (8)) is very close to real value.

To have information about interfacial charges and separate them from bulk charges, and also obtain the values of Q_{to} and X_{to} we can use both photo-I-V and C-V measurement together:

photo-I-V $\Rightarrow Q_b$, X_b

C-V $\Rightarrow Q_{to}\, X_{to}$ [$Q_{to} = Q_b + Q_i$, Q_i includes $Q_{it}(0)$]

We have:

$$Q_{to}\, X_{to} = Q_b X_b + Q_i L$$

Which results:

$$Q_i = \frac{Q_{to} X_{to}}{L} - \frac{Q_b X_b}{L} \qquad (11)$$

By knowing the value of Q_i the value of Q_{to} can be calculated:

$$Q_{to} = Q_b + Q_i \qquad (12)$$

and by knowing Q_{to} the value of X_{to} can be calculated:

$$X_{to} = Q_{to} X_{to} / Q_{to} \qquad (13)$$

To have information about interface state densities we can use HF or/and LF C-V measurement. Also the total number of interface states can be obtained by measuring the different shifts of HF curve points for corresponding points of accumulation region and inversion region:

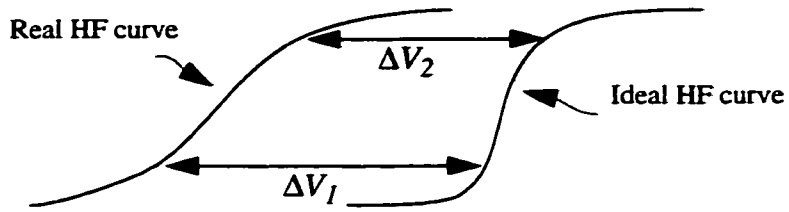

$$\int_{E_v}^{E_c} D_{it}(E)\,dE = \frac{\Delta V_1 - \Delta V_2}{L \cdot e}\varepsilon_{ox} \qquad (14)$$

[e : electron charge]

---

1. In our C-V program that we use to find Q_{to} , the program consider $X_{to} = L$ to calculate Q_{to} from equation (8). This leads to estimation of the density of the charges that are close to Si/SiO_2 interface. For the cases that all charges are just near two interfaces, that estimation is close to real value; for example if there are equal charges of $q_1=q_2=q$ near both interfaces, the real values of X_{to} and Q_{to} are equal to $L/2$ and $2q$ respectively, and the measured value of the product of these two values is equal to $L.q$. If we consider wrongly the value of X_{to} equal to L then the value of Q_{to} will be calculated $L.q/L = q$. This value is half of the real value of Q_{to} ; however it is the correct value of the charges close to Si/SiO_2 interface.

Appendix D

Simulation Program

```
%*****************************************************************************
%          The following program simulates the Thickness profiles of the oxide films
%          grown through the point-to plane positive and negative corona processes. It
%          calculates thicknesses based on the linear-parabolic equation, and using the
%          modifed values of the parameters that are used in the Deal-Grove model
%          of thermal oxide films.
%*****************************************************************************

%********************* Opening a window to show the parameters
%                                  that needed to be entered by user
check=exist('parameters');
if check == 0
    figure(1); clf; axis([0 1 0 1]); axis('off');
    text(-.1,1,'before running the program enter the following parameters');
    text(-.08,.9,'temp=? ( in C)');
    text(-.08,.85,'corona=? (-1 for negative and 1 for positive corona)');
    text(-.08,.8,'OtoNr=? ( the percentage of oxygen; 1 for 100% )');
    text(-.08,.75,'time=? (time of oxidation in minute)');
    text(-.08,.7,'xin=? (initial oxide thickness in Angstrom)');
    text(-.08,.65,'I=? corona current in uA(absolute value)');
   text(-.08,.6,'cxf,ksxf,dxf=? changing factors for concentration, reaction and diffusion');
   text(-.08,.55,'Hlen=? half of the length of wafer in mm');
```

```
    text(-.08,.5,'Hlcp,Hlcn=? half of the length for effect on concentration in positive and neg-
    ative corona');
    text(-.08,.45,'Hldp, Hldn=? half of the length for effect on diffusion in positive and nega-
    tive corona');
    text(-.08,.4,'Hlkp, Hlkn=? half of the length for effect on reaction in positive and negative
    corona');
    text(-.08,.3,'siltype=? (100 0r 111)')
end;
parameters=1;

%********** Calculating the coeffitients which will be used to
%                    modify the B and B/A parameters
cx=cxf*I;
if corona == -1
    ksx=ksxf*I;
    elseif corona == 1
    ksx=ksxf*(I^(0.5));
end
Dx=dxf;

%********** Calculating the original valus of B and B/A
%                    at the oxidation temperature

K=8.62*(10^(-5)); T=273+temp; E1=1.23; C1=772;
if siltype == 100
    C2=(6.23/1.68)*(10^6); E2=2;
```

```
    elseif siltype == 111
    C2=(6.23)*(10^6); E2=2;
end

B=C1*(exp(-1*E1/(K*T)));
BoverA=C2*(exp(-1*E2/(K*T)));
A=B/BoverA;
B=B*OtoNr;

%********************** Giving the initial values of the parameters
%                              that belong to different regions of the film
for x=-1*Hlen : Hlen;
   b(x+Hlen+1)=B;
   a(x+Hlen+1)=A;
   c(x+Hlen+1)=1;
   ks(x+Hlen+1)=1;
   d(x+Hlen+1)=1;
end

%******************** Calculating the modified values of concentration
%                              factors for different regions of the film

%Hlcp: half of the effective lenght base on the concentration factor
%                              for positive corona
if corona == 1
    for x=-1*min(Hlcp,Hlen) : min(Hlcp,Hlen);
```

```
        c(x+Hlen+1)=(1/(cx+1))-(((1/(cx+1))-1)/(Hlcp^2))*(x^2);
    end
    for x=-Hlen : Hlen;
        b(x+Hlen+1)=b(x+Hlen+1)*c(x+Hlen+1);
    end
  else
   %Hlcn: half of the effective length based on the concentration factor
   %                                    for negative corona
    for x=-1*min(Hlcn,Hlen) : min(Hlcn,Hlen);
        c(x+Hlen+1)=(cx+1)-(cx/(Hlcn^2))*(x^2);
    end
    for x=-1*Hlen : Hlen;
        b(x+Hlen+1)=b(x+Hlen+1)*c(x+Hlen+1);
    end,
end
```

%******** Calculating the modified values of diffusion**

%   factors for different regions of the film

```
%Hldp: half of the effective length based on the diffusion factor in positive corona
if corona == 1
    for x=-1*min(Hlen,Hldp) :min(Hlen, Hldp),
        d(x+Hlen+1)=((Dx+1))-(Dx/((Hldp)^2))*(x^2);
    end
    for x=-1*Hlen : Hlen;
        b(x+Hlen+1)=b(x+Hlen+1)*d(x+Hlen+1);
```

```
        a(x+Hlen+1)=a(x+Hlen+1)*d(x+Hlen+1);
    end
    %Hldn: half of the effective length based on the diffusion factor in negative corona
  else
    for x=-1*min(Hlen,Hldn): min(Hlen,Hldn),
        d(x+Hlen+1)=(Dx+1)-(Dx/(Hldn)^2)*(x^2);
    end
    for x=-1*Hlen: Hlen,
        b(x+Hlen+1)=b(x+Hlen+1)*d(x+Hlen+1);
        a(x+Hlen+1)=a(x+Hlen+1)*d(x+Hlen+1);
    end,
end
```

%******** Calculating the modified values of interface reaction**

% factors for different regions of the film

```
%Hlkp: half of the effective length based on the reaction factor in positive corona
if corona == 1
    for x=-1*min(Hlen,Hlkp) : min(Hlen, Hlkp),
        ks(x+Hlen+1)=(ksx+1)-(ksx/(Hlkp^2))*(x^2);
    end
    for x=-1*Hlen : Hlen,
        a(x+Hlen+1)=a(x+Hlen+1)/ks(x+Hlen+1);
    end
    %Hlkn: half of the effective length based on the reaction factor in negative corona
  else
```

```
    for x=-1*min(Hlen,Hlkn) : min(Hlen,Hlkn),
        ks(x+Hlen+1)=(ksx+1)-(ksx/(Hlkn^2))*(x^2);
    end
end
for x=-1*Hlen : Hlen,
    a(x+Hlen+1)=a(x+Hlen+1)/ks(x+Hlen+1);
end

%****************************** Calculating the thicknesses

t=time/60;          % t: oxidation time in hour
Xi=xin/10000;               % Xi: initial thickness in um
for x=-1*Hlen : Hlen,
    ta(x+Hlen+1)=((Xi^2)+(a(x+Hlen+1)*Xi))/b(x+Hlen+1);
end

% The following calculated thicknesses are in um
for x=-1*Hlen : Hlen,
    thickness(x+Hlen+1)=(a(x+Hlen+1)/2)*(sqrt(1+(((t)+ta(x+Hlen+1))/          ...
      ((a(x+Hlen+1)*a(x+Hlen+1))/(4*b(x+Hlen+1)))))-1);
end

%****************************** Plotting the result
for x=-1*Hlen : Hlen,
    xax(x+Hlen+1)=x;
end
```

```
figure(2);plot([]);hold on;

plot(xax(1:(2*Hlen)+1),thickness(1:(2*Hlen)+1)*10000);

xlabel(' Distance from center mm');

ylabel('thickness A')


%*****************Showing the process parameters and some calculated

%                          values

I=I,siltype=siltype,time=time,temp=temp,ksxf=ksxf,cxf=cxf,dxf=dxf

centertox=thickness(Hlen+1)*10000

edgetox=thickness(1)*10000

xin=xin

%******** The modified values of B/A and B at the center and edge regions

boveracenter=(b(Hlen)/a(Hlen))

boveraedge=(b(1)/a(1))

bcenter=b(Hlen)

bedge=b(1)
```